ALUMINA-FORMING NANOLAMINATED CARBIDES AND BORIDES

A Dissertation

by

YEXIAO CHEN

Submitted to the Office of Graduate and Professional Studies of
Texas A&M University
in partial fulfillment of the requirements for the degree of

DOCTOR OF PHILOSOPHY

Chair of Committee,	Miladin Radovic
Co-Chair of Committee,	Ibrahim Karaman
Committee Members,	Homero Castaneda-Lopez
	Sean M. McDeavitt
Head of Department,	Ibrahim Karaman

May 2020

Major Subject: Materials Science and Engineering

ABSTRACT

Alumina-forming materials, such as FeCrAl-based alloys, Ni, Co or Fe based superalloys, have been long studied because of their excellent oxidation resistance and promising applications at high temperatures. Recently, alumina forming ceramics (carbides, nitrides and borides) with nanolayered structures, gained a lot of attention as a good candidate material for high temperature applications because of their excellent oxidation resistance, good mechanical properties, and thermal stability at much higher temperatures than alumina forming metallic alloys. Some of the most interesting alumina forming ceramics belongs to families of nanolayered ternary carbides and nitrides with a generalized formula $M_{n+1}AX_n$ (n=1,2,3) (MAX), and nanolayered ternary borides with a generalized formula $(MB)_{2z}A_x(MB_2)_y$ (z = 1-2, x=1-2 and y=0-2) (MAB), with A element being Al.

In this dissertation work, alumina-forming mechanism of MAX phases, namely Ti_2AlC is studied. The results of this study indicate that Al deficient of approximately 4% in Ti_2AlC leads to the breakaway oxidation, i.e. formation of Al_2O_3+TiO_2 oxide, instead of protective Al_2O_3 oxide layer. The outcomes of this study expected to be contributing towards the research and development of advanced Ti_2AlC MAX phase with good oxidation resistance behavior. A thin layer of Ti_2AlC was successfully diffusion bonded onto Ti alloy Ti6242 at 800 °C by Pulsed Electric Current Sintering (PECS) to evaluate feasibility of using Ti_2AlC as environmental barrier coating (EBC) for high-temperature Ti-alloys.

Cr_2AlC is another MAX phase with the potential of forming protective alumina oxide layer when exposed to high temperature in oxidizing environment. The results in this study show that formation of Cr_7C_3 sub-layer can be avoided in Cr_2AlC samples free of chromium-carbide impurities or in samples with excess Al. In addition, we have shown that small amounts of impurities in starting Cr powders (such as Fe) as well as absence of Cr_7C_3 sub-layer leads to the wrinkling of alumina scale and its premature spallation.

Although MoAlB has been proposed as good candidate material for high temperature applications because it forms stable and protective alumina oxide layer, its mechanical properties at high temperatures have not been studied in the past. In this study a quasi-static and cyclic compression testing at room and high temperatures were conducted on MoAlB. The results show that MoAlB goes through a brittle-to-plastic transition (BPT) at around 800 °C, similar to that observed in MAX phases. While post-testing microstructural observation showed only a few bends and kinks of individual grains, extensive microcracking was observed.

DEDICATION

To my parents, my friends and all people helped me.

ACKNOWLEDGEMENTS

I would like to express the deepest appreciation to my committee chair Dr. Miladin Radovic and co-chair Dr. Ibrahim Karaman, for their continuous guidance and support throughout the study and research. Without their innovative ideas and persistent tutoring, I could not have imagined my Ph.D study would be such a great experience.

I also would like to thank Dr. Homero Castaneda and Dr. Sean McDeavitt for giving me helpful suggestions as my committee members.

I truly appreciate all help from collaborators from Texas A&M University and other research institutes. I want to thank Dr. Anup Bandyopadhyay for his training in sample preparation, SPS, vacuum tube furnace, DSC, TGA and XRD. Thanks go to Dr. Yordanos Bisrat, Dr. Winson Kuo, Dr. Andrew Mott and Dr. Wilson Serem for the training of SEM, EBSD, nano-indentation, TMA, Thermal Conductivity Analyzer, FIB and use of EPMA. I express my appreciation to Dr. Sankalp Kota and Dr. Michel Barsoum from Drexel University for the collaboration and communication in the area of ternary metal borides for high temperature applications. I would like to acknowledge Dr. James L. Smialek from NASA Glenn Research Center and Dr. Thierry Ouisse from Université Grenoble-Alpes for helping me with TGA and supplying single crystal samples.

Thanks also go to my roommate, my friends and colleagues and. I want to thank Yongjin Liu who helped settled down since entering College Station. I also want to thank Dr. Peipei Gao, Dr. Amy Bolon, Dr. Junwei Xing, Dr. Liangfa Hu, Dr. Rogelio

Benitez, Dr. Huili Gao, Matthew Westwick for helping me start my study in the research group. My thanks go to Zeyi Tan, Zhiqiang Zhan, Oscar Huang, Evan Prehn, Marco Martinez, Dong Gi Ha, Dustin Holta, Vrushali Kotasthane, Leping Cai, Xiaofei Zhao, Wenchao Du, Wenhao Lin, Lei Xue, Dr. Yiming Fan, who made my stay and studies more enjoyable. Additionally, I want to thank all the department faculty and staff in Materials Science and Engineering Department for making my time at Texas A&M University a great experience.

I want to extend my appreciation to the Air Force Research Laboratory (Project: FA8650-15-D-5230 0001) and the U.S. National Science Foundation (Award: 1410983 and 1729350), which provided the funding throughout my Ph.D. research.

Last but not least, lots of thanks to my mother, father and Yi Zhou for their company and encouragement, and their solid trust, understanding and patience.

CONTRIBUTORS AND FUNDING SOURCES

Contributors

This work was supervised by a thesis committee consisting of Professors Radovic, Karaman and Castaneda of the Department of Materials Science and Engineering, and Professor McDeavitt of the Department of Nuclear Engineering.

The Electron Microprobe Analysis (EPMA) data depicted in Chapter 2 was collected in part by Dr. Mott of the Materials Characterization Facility. The starting materials in Chapter 3 and 4 were supplied in part by Air Force Research Laboratory and Dr. Ouisse of Université Grenoble-Alpes. The oxidation and mechanical analyses depicted in Chapter 5 were conducted in part by Dr. Kota from Drexel University and were published in 2017 and 2019.

All other work conducted for the thesis was completed by the student independently.

Funding Sources

This work was supported by Air Force Research Laboratory under Grant Number FA8650-15-D-5230 0001, and the U.S. National Science Foundation under Grant Number 1410983 and 1729350.

NOMENCLATURE

ΔW	Weight Gain
A	Area
Al_2O_3	Alumina
bcc	Body Centered Cubic
BPT	Brittle-to-plastic Transition
BPTT	Brittle-to-plastic Transition Temperature
BSE	Backscatter Electron
CG	Coarse Grain
CTE	Coefficient of Thermal Expansion
D	Diffusivity
E	Elastic Modulus
EBC	Environmental Barrier Coating
EBSD	Electron Backscatter Diffraction
EDM	Electrical Discharge Machining
EDS	Energy Dispersive Spectroscopy
EPMA	Electron Microprobe Analysis
FG	Fine Grain
HC	High Carbide
hcp	Hexagonal Close Packed
HP	Hot Press

IKB	Incipient Kink Band
KB	Kink Band
LC	Low Carbide
MAB	$(MB)_{2z}A_x(MB_2)_y$ (z = 1-2, x=1-2 and y=0-2)
MAX	$M_{n+1}AX_n$ (n = 1,2,3)
MTS	Materials Test System
PP	Phase Pure
Q	Activation Energy
RT	Room Temperature
RUS	Resonant Ultrasound Spectroscopy
SEM	Scanning Electron Microscopy
SPS	Spark Plasma Sintering
T	Temperature
T_m	Melting Temperature
TMB	Ternary Metal Boride
TGA	Thermogravimetric Analysis
UCS	Ultimate Compressive Strength
XRD	X-ray Diffraction

TABLE OF CONTENTS

Page

LIST OF FIGURES

Page

LIST OF TABLES

Page

1. INTRODUCTION

1.1 Alumina forming ternary carbides and borides

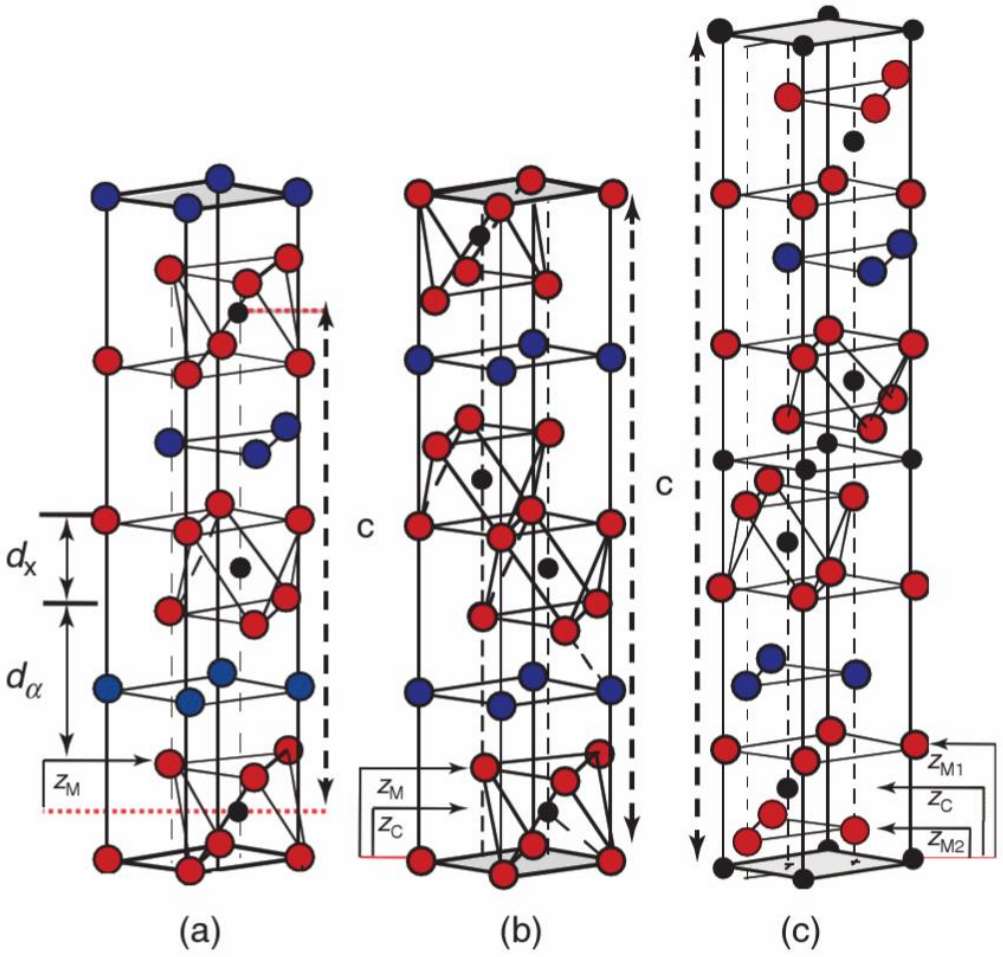

Figure 1.1 Unit cells of (a) 211, (b) 312 and (c) 413 MAX phases, where M, A and X atoms are denoted as red, blue and black respectively [1].

$M_{n+1}AX_n$ phases (or MAX phases) are a group of ternary metal carbides and nitrides where M is early transition metal, A is group 13-16 element and X is C and/or N [2, 3]. The MAX phases have nano-laminated hexagonal structures where near-close-packed M layers are interleaved by layers of A element and with X atoms occupying the

octahedral sites between M atoms. According to the number of multiple M layers separating the A layers, (Figure 1.1) MAX phases can be M_2AX or 211, M_3AX_2 or 312, M_4AX_3 or 413, etc. Because of the various choices in M and A elements in MAX phases, currently, the MAX phases number over 60 [1, 3]. Most of the MAX phases are 211, some are 312 and the rest are 413. Typical M group elements include Ti, V, Cr, Zr, Nb, Mo, Hf and Ta, while A elements include Al, Si, P, S, Ga, Ge, As, Cd, In, Sn, Tl and Pb., **Figure 1.2**.

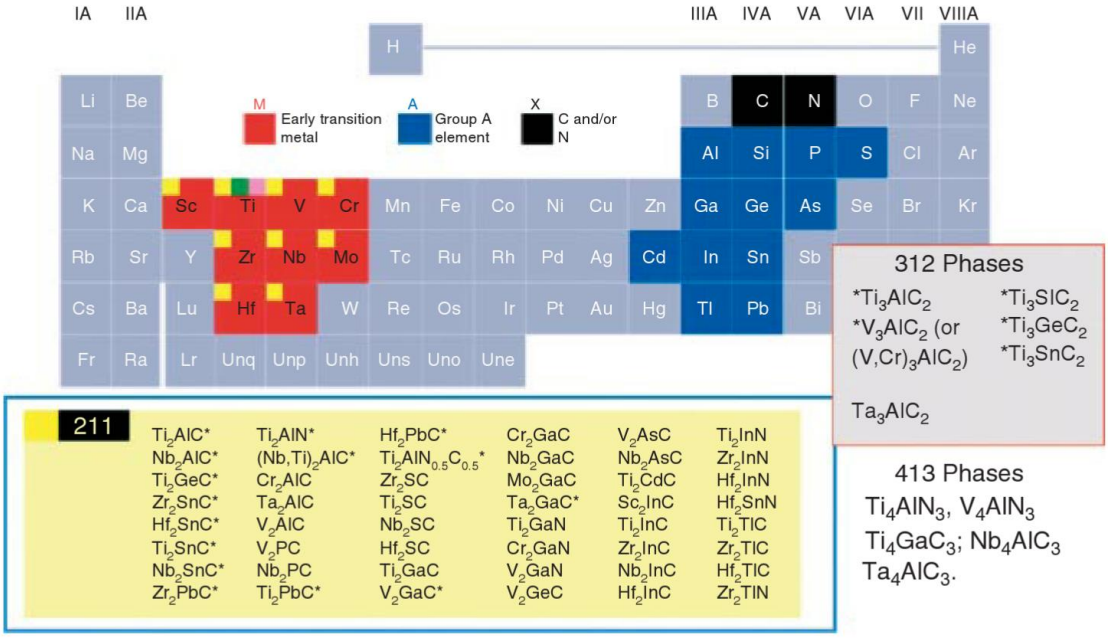

Figure 1.2 List of MAX phases found to date [1].

The MAX phases are fascinating since they have a very unique combination of ceramic and metallic properties such as high stiffness like the binary metal carbides/nitrides and good electrical and thermal conductivity like metals [1, 2, 4-6]. The MAX phases also have excellent thermal shock resistance, good damage tolerance and

high fracture toughness [7]. Moreover, the MAX phases are readily machinable with conventional tooling such as a simple hack-saw. These combination of properties could be traced back to the unusual layered structures in the MAX phases, where the M-X bonds between M and X atoms are exceptionally strong, while the M-A bonds are relatively weak, especially in shear.

Apart from MAX phases, transition metal borides are also appealing class of refractory materials because of their high melting points, high hardness, good corrosion resistance in many environments, and good electrical/thermal conductivities. This fascinating set of properties, among others, make them useful for high-temperature structural applications, wear-resistant coatings, diffusion barriers, high-temperature electrodes, solar absorbers, catalysts, etc. [8-13]. However, their utilization in many of those applications is limited because of their inherent mechanical brittleness, poor oxidation and thermal shock resistance, and relatively high cost [14-18]. MAB phases, with atomically laminated transition metal borides where A-atom plane(s) interleaves M-B sublattices. They have potential to overcome some of the limitations faced by traditional trasniton metal borides in high-temperature oxidizing environments. MAB phases have a general formula $(MB)_{2z}A_x(MB_2)_y$ (z = 1-2, x=1-2 and y=0-2) [19]. Typically, the M-B sublattices in the MAB phases have orthorhombic crystal structure composing of face-sharing trigonal prisms (BM_6) with B atoms in the center the prism. Depending on the M:B ratio and the number of A-atom planes, MAB phases can form MAB (or 222), M_2AB_2 (or 212), M_3AB_4 (or 314), M_4AB_6 (or 416) and M_4AB_4 (or 414) structures, **Figure 1.3**. The first 222 MAB phase, namely MoAlB, was synthesized in

1942 by Halla and Thurry [20] and later confirmed by Jeitschko et al. in 1966 [21] to have an orthorhombic (*Cmcm* space group) structure with a CrB-like, Mo-B sublattice interleaved by Al bilayers. In 1987, another 222-type, namely WAlB was synthesized by Zhang et al. [22], followed by solid solutions of $(Mo_{1-x}W_x)AlB$ and $(Mo_{1-x}Cr_x)AlB$ [23, 24]. For 212-type, Mn_2AlB_2 was first synthesized in 1996 and showed the CrB-like Mn-B sublattice interleaved by Al monolayers [25], and Fe_2AlB_2 was found in the same year [26]. However, Cr_2AlB_2, discovered in 1973, consisted of a Cr_3B_4-like sublattice interleaved by Al monolayers [27]. The sublattice is Cr_2B_3-like in Cr_4AlB_6, Cr_3B_4-like in Cr_3AlB_4 [28] and two stacks of CrB blocks in lately new Cr_4AlB_4 [29].

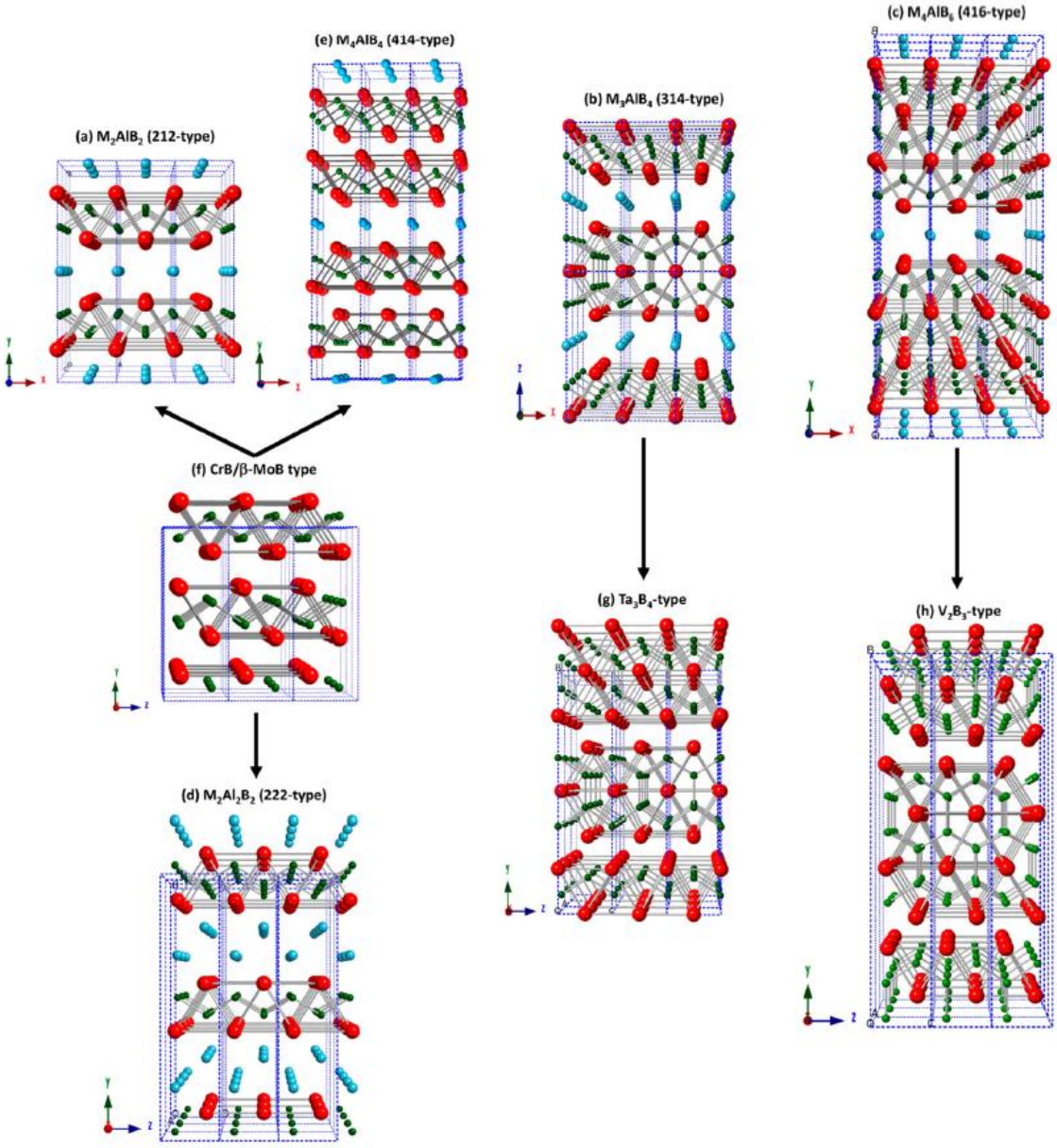

Figure 1.3 Crystal structures of various MAB phases and structurally related binary borides: (a) 212-type [*Cmmm*], (b) 314-type [*Pmmm*], (c) 416-type [*Cmmm*], (d) 222-type [*Cmcm*], (e) 414-type [*Immm*], (f) CrB/β-MoB [*Cmcm*], (g) Cr_3B_4 [Immm], and (h) Cr_4B_6 [Cmcm]. The M, Al, and B atoms are shown in red, light blue, and green, respectively. Dotted blue lines outline individual unit cells. Note that multiple unit cells are shown for clarity [19].

1.2 Oxidation resistance of MAX phases

In general, the oxidation of the MAX phases at high temperatures occurs according to the following reaction:

$$M_{n+1}AX_n + bO_2 = M_{n+1}O_x + AO_y + X_nO_{2b-x-y} \quad (1.1)$$

For example, Ti_3SiC_2 as one of the most studied MAX phases forms TiO_2 and SiO_2 as a result of the overall oxidation reactions according to [30]:

$$Ti_3SiC_2 + 6O_2 = 3TiO_2 + SiO_2 + 2CO_2 \quad (1.2)$$

The oxidation of Ti_3SiC_2 results in formation an outer SiO_2 layer and an inner TiO_2 layer. Carbon from Ti_3SiC_2 is believed to get oxidized in this process and form CO_2 gas.

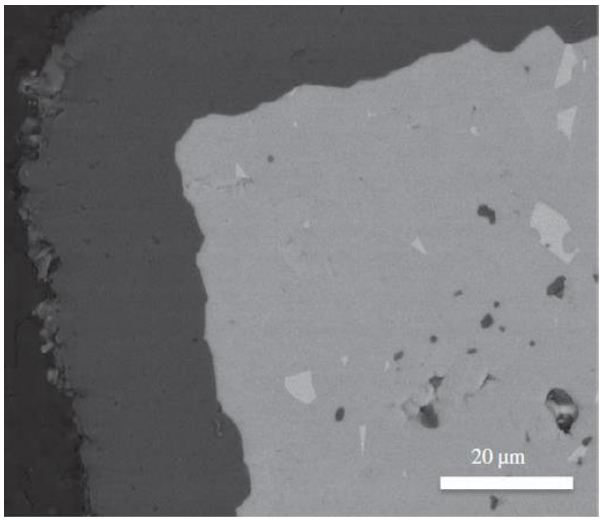

Figure 1.4 SEM, micrograph of Ti2AlC oxidized in air at 1,200◦C for 2,873 h showing a ≈ 21 µ m thick, coherent and fully dense Al_2O_3 layer which conforms to the corners of the sample. [31]

Similarly, Ti_2InC is oxidized to TiO_2 and In_2O_3 [32] while oxidation of Ti_2SnC results in TiO_2 and SnO_2 [33]. In general, the oxidation resistance of all those MAX phases is quite poor because of the formation of duplex oxide scale and oxidation rate

tended to be linear. However, some of MAX phases containing Al show good oxidation resistance [31] because they form protective and adherent alumina layer (**Figure 1.4**). The formed Al_2O_3 layer has long been believed to contribute to the excellent oxidation resistance in Al_2O_3-forming alloys [34-37] due to its high stability and slow growing kinetics [38].

Ti_2AlC is one of Al_2O_3-forming MAX phases and is by far the most attractive for practical applications due to a low density, high concentration of Al and excellent thermal expansion (9-9.6 × 10^{-6} $^oC^{-1}$) match with Al_2O_3 (8.8 × 10^{-6} $^oC^{-1}$ along c-axis direction and 7.9 × 10^{-6} $^oC^{-1}$ normal to c-axis direction) [39]. The residue stresses formed in the Al_2O_3 layer were reported as compressive – of the order of 500 MPa [40]. Such residual stresses are considered low compared to commercially available Fe- and Ni-based Al_2O_3-forming alloys.

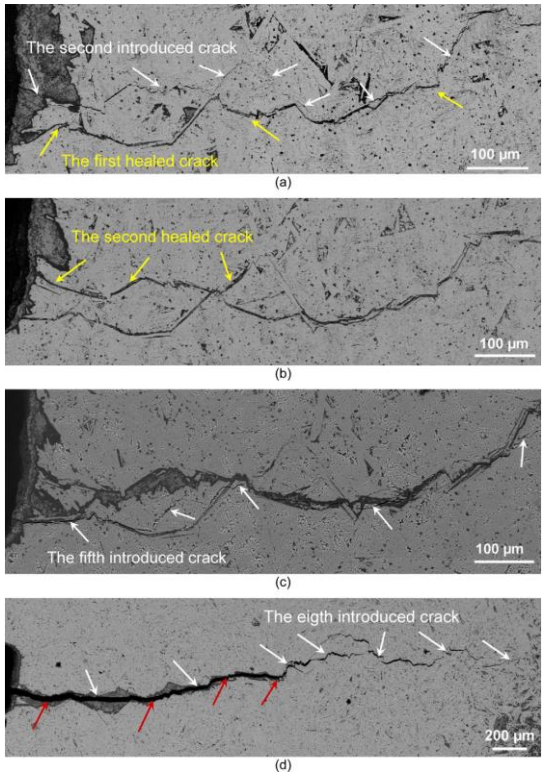

Figure 1.5 Black-scattered scanning electron micrographs of fracture and crack healing of Ti_2AlC samples. (a) Crack path after one cycle of healing and subsequent fracture. (b) After two cycles of healing, the second crack was completely filled again. (c) Crack path after four cycles of healing, and subsequent fracture. (d) Crack path after seven cycles of healing, and subsequent fracture. [41].

Another intriguing thing associated with the oxidation of Ti_2AlC and Ti_3AlC_2 is their crack healing phenomenon [41-43]. For example, **Figure 1.5** shows that the cracks in Ti_2AlC are completely healed during oxidation after 5 repeated d amage events. Although the flexural strength dropped from 211 MPa for undamaged Ti_2AlC to 152 MPa for Ti_2AlC with surface crack, it was recovered to 224 MPa after heating the crack in air for 2 h at 1100 °C. It is also noticeable that the crack was filled with well-adhering Al_2O_3 and some TiO_2. In summary, the excellent formation of protective Al_2O_3 layer on

the surface and crack healing capability, make Al_2O_3 forming MAX phases promising in practical applications

Not like other non-Al containing MAX phases, the oxidation of Ti_2AlC was described as [39]:

$$Ti_2AlC + (\frac{3x}{4} + y)O_2 = (\frac{y}{2})Al_2O_3 + Ti_2Al_{1-x}C_{1-y} + yCO_2 \quad x<0.5 \tag{1.3}$$

In the case of Ti_3AlC_2, the oxidation reaction is:

$$Ti_3AlC_2 + (\frac{3x}{4} + y)O_2 = (\frac{y}{2})Al_2O_3 + Ti_3Al_{1-x}C_{2-y} + yCO_2 \quad x<0.5 \tag{1.4}$$

Initially, reported oxidation kinetics of alumina forming Ti_2AlC phase were not in agreement since it was quantified either as parabolic [44-46] or cubic [39, 40, 47, 48] based on different work. A comprehensive work was done by Tallman et al [31] finally confirmed that the oxide layer thickness (x) for Ti_2AlC increases as a function of time (t) show up to at least 3000 h, following are oxidation kinetics that can be expressed as:

$$x(\mu m) = 1.2(\frac{t}{t_0})^{0.36} \tag{1.5}$$

where t_0 = 1 h, and R^2 for the power law fitting is 0.998. To investigate the oxidation mechanism, an assumption is made based that kinetics of the oxide growth is controlled by grain boundary diffusion of oxygen and grain coarsening, similar to oxidation of Y-doped FeCrAl alloy [49]. First, the oxide grain coarsening during high-temperature can be is described as [50]:

$$d^m = {d_0}^m + Kt \tag{1.6}$$

where K is a constant, m is the grain growth exponent, d_0 is the initial grain size and t is time. Therefore, the thickness of the Al_2O_3 scales (x) can be expressed at a longer time, as:

$$x^2 \approx K'(\frac{t}{t_0})^{(m-1)/m} \quad (1.7)$$

$$n \approx (m-1)/2m \quad (1.8)$$

where K' is a constant. In the case of Ti_2AlC, a value of 3.23 for m was obtained. The m leads to a value of *n* equal to 0.345, which is in an excellent agreement with the value of 0.36 obtained from experiments [31]. This mechanism is recently proved by a modified Wagner treatment [51, 52] and an oxygen diffusion product $\delta D_{gb,O,int}$ is proposed as:

$$12\delta D_{gb,O,int} = k_{p,i} G_i \quad (1.9)$$

$$\delta D_{gb,O,int} = K'' exp(\frac{-Q}{RT}) \quad (1.10)$$

where $k_{p,i}$ is instantaneous parabolic rate constant, G_i is corresponding grain diameter at that time, K'' is a constant, Q is activation energy for grain boundary diffusion of oxygen. In FeCrAl(Zr) heater alloy (Hoskins 875), K'' is found to be 1.8×10^{-10} m^3/s and Q equals 375 kJ/mol. With the same calculation, those values in Al_2O_3-forming MAX phases are found to be in good agreement with FeCrAl alumina forming alloys (**Figure 1.6**) [53]. Thus the Al_2O_3 forming process in Al_2O_3-forming MAX phases and FeCrAl alloys is commonly accepted as Al diffuses outward and O diffuses inward along the Al_2O_3 grain boundary and its kinetics is controlled by an oxygen grain boundary diffusion as long as amount of Al is sufficient in the substrate for preferential oxidation of Al.

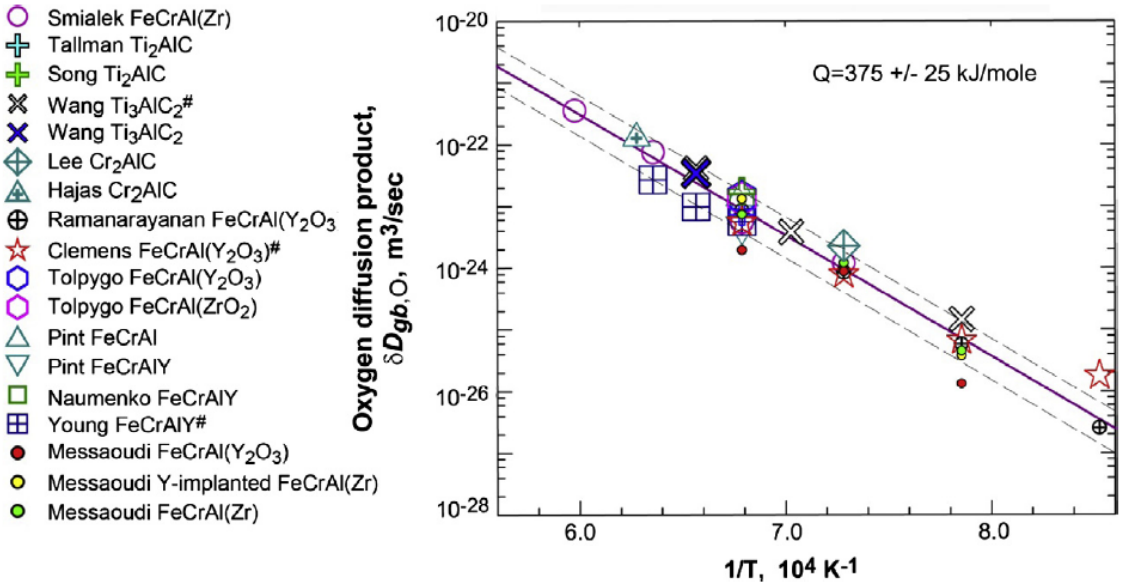

Figure 1.6 Oxygen grain boundary diffusivity from MAX phases compared to other FeCrAl(X) alloy behavior. [53]

However, in some alumina-forming alloys [34-36], once Al in the substrate is depleted or Al concentration is below a critical level, the substrate will be oxidized immediately forming complex non protective oxides because the incapability of forming protective Al_2O_3 scale. Although Ti_2AlC has remarkable oxidation resistance due to the formation of the protective Al_2O_3, other Al-based MAX phases such as Ti_3AlC_2 show catastrophic breakaway oxidation and formation of mixed α-Al_2O_3+TiO_2 scale after long-term oxidation [31, 54]. It is well-established by now that every alumina-forming system must contain a critical Al content below which the selective oxidation of Al to form a predominantly Al_2O_3 scale is not possible anymore [55]. For Ti_3AlC_2, Li et al [54] showed that decrease of Al content below 5.99% causes oxidation breakaway due to formation of TiC binary carbides. Similarly, it has been shown that quick depletion of Al

on the surface of Cr_2AlC results in formation of Cr_7C_3 binary carbides in depilated zone below Al_2O_3 oxide scale [31, 56]. To the best of our knowledge, no breakaway oxidation studies of Ti_2AlC have been reported thus far, although this MAX phase is considered to be one of the best alumina-formers. [40] To find experimentally the conditions at which breakaway oxidation occurs in bulk MAX phases is not a trivial task since it can require more than 3000 h of exposure to air at high-temperature to detect breakaway oxidation, as in the case for Ti_3AlC_2 [54]. An alternative approach for studying oxidation breakaway in MAX phases is to use wedge-shaped samples. The approach was used successfully to study oxidation breakaway in FeCrAl base alloys [57], where a critical Al concentration is found around 1.8wt% for MA956 alloy, 1.1wt% for Kanthal APM and 3.5wt% for PM2000. Later in 2004, the approach was applied to ODS Fe_3Al and found the critical Al content at 10.4% [36]. Hence, the approach would appear to offer considerable potential to find out the critical breakaway oxidation conditions for Ti_2AlC.

1.3 Oxidation of MAB phases

Similar to MAX phases, some of Al containing MAB phases also possess good oxidation resistance. In 2016, SEM and XRD results of hot-pressed MoAlB after heating in ambient air at 1100 and 1300 °C indicated formation of adherent Al_2O_3 scales when (**Figure 1.7**) like in the case of Al_2O_3-forming MAX phases [58]. Differential thermal analysis (DTA) and thermogravimetric analysis (TGA) on the hot-pressed MoAlB samples in a flowing Ar atmosphere showed that Al de-intercalates from the MoAlB layer [59], implying a similar formation mechanism of protective Al_2O_3 layer like Al_2O_3-forming MAX phases scales by the Al diffusion to the surface and formation of

protective Al_2O_3. Similar mechanism was also found in Mn_2AlB_2 at lower temperatures, i.e. before it decomposes into binary MnB and Al at temperatures > 1379K [60]. Xu et al. also reported the formation of Al_2O_3 scales on hot-pressed MoAlB [61] and Shi et al. reported the same observation on MoAlB single crystals [62].

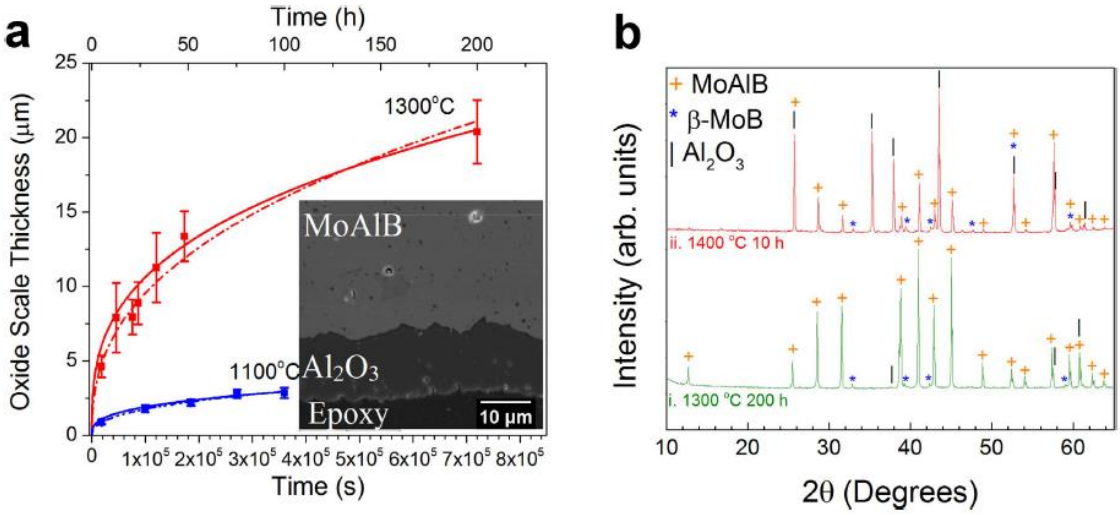

Figure 1.7 (a) Time dependence of the oxide scale thickness from isothermal oxidation testing at 1300 °C (red) and 1100 °C (blue). Inset show MoAlB/oxide scale interface after 200 h at 1300 °C; (b) XRD after oxidation at (i) 1300 °C for 200 h and, (ii) 1400 °C for 10 h [58].

1.4 Mechanical behavior of MAX and MAB phases

Apart from good oxidation resistance and formation of the protective oxide scale, mechanical properties of MAX and MAB phases are critical for their potential applications as a structural materials or protective coatings in oxidizing environments and at elevated temperatures.

The mechanical properties of MAX phases are very atypical of common binary carbides and nitrides since they deform by a formation of kinks and kink bands (KBs)

[63-65]. The mechanism of the formation of KBs is summarized schematically in **Figure 1.8**. Loading along the basal plane creates elastic bending in **Figure 1.8(a)** which in turn results in a shear stress distribution as seen in **Figure 1.8(b)**. Above a critical value, this shear stress will create pairs of dislocations with opposite signs and those dislocations move in the opposite directions in the basal plane to form Mobile Dislocation Wall (MDW) as seen in **Figure 1.8(c)**, followed by accumulation of the MDWs into kink boundaries as seen in **Figure 1.8(d)**. One explanation for the accumulation of MDW in KB is that the first wall is stopped by defect and so MDW starts to accumulate near this defect [66]. The other explanation is that under external load each wall results in the small angles between loading direction and basal plane, thus the shear stress for each wall is increased differently and each walls moves in different speeds, which results in the accumulation of the dislocation walls in KBs [67].

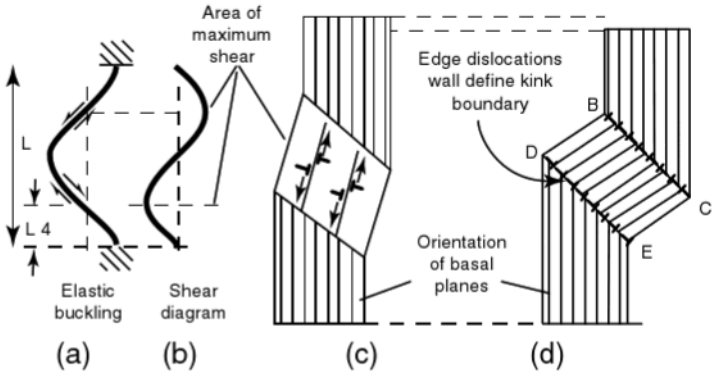

Figure 1.8 Schematic of kink band formation. [66, 67]

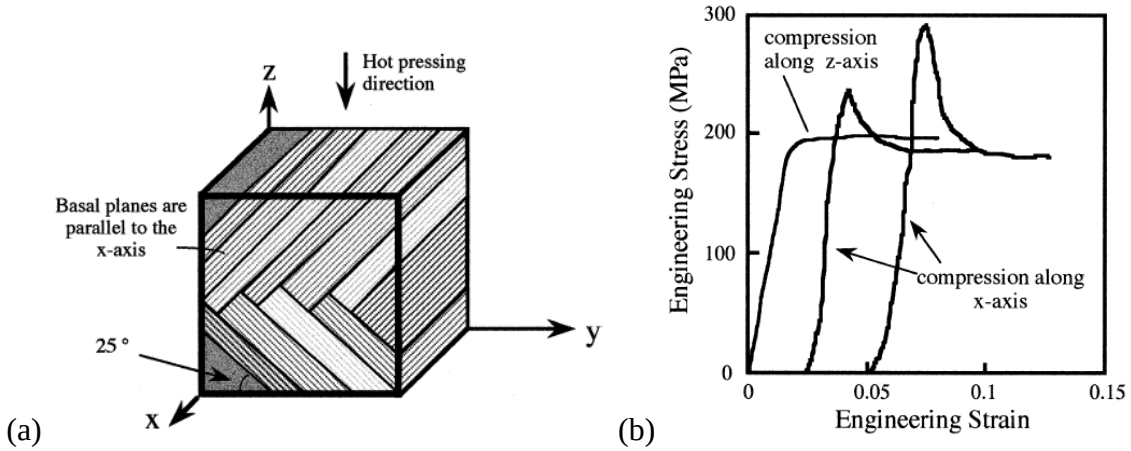

Figure 1.9 (a) Schematic of grain orientation relative to loading directions. Basal planes are for the most part parallel to the x-axis; (b) Stress-strain curves compressed in the z directions and the x direction, i.e., parallel to the basal planes. The curves are shifted by 0.025 strain for clarity's sake. [68]

Because of the easy slip that is limited only to the basal planes and kinking, MAX phases deform anisotropically upon loading and their mechanical response depends on the orientation of the individual grains. **Figure 1.9(a)** shows a schematic of highly textured Ti_3SiC_2 subject to load in the z (approximately 45^o relative to basal planes) and the x (parallel to the basal plane direction) directions. The stress-strain curves in **Figure 1.9(b)** show initial elastic behavior followed with by the plastic flow in z direction, once the critical resolved shear stress for basal plane dislocation glide is reach. However, the stress-strain behavior is quite different in x direction, with the maximum stress at onset of kinking, followed with rapid softening do to kink induced shear bands.

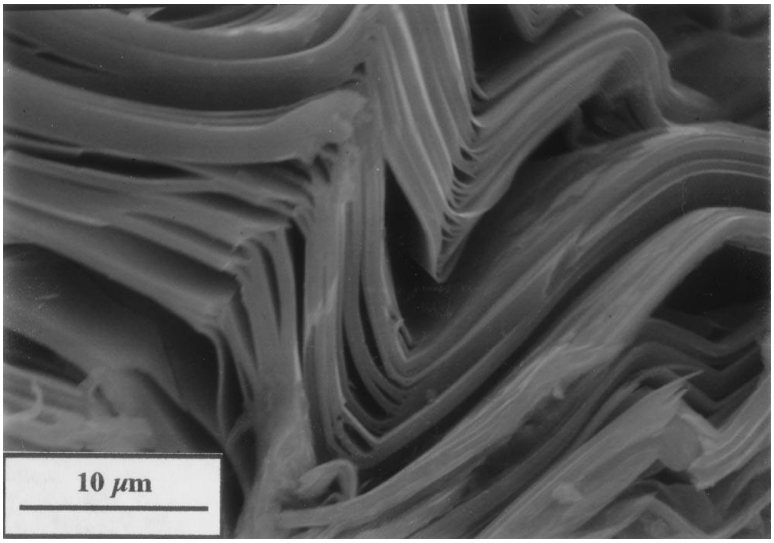

Figure 1.10 SEM micrograph of Ti_3SiC_2 showing multiple, nested kink bands. [65]

In polycrystalline MAX phases show hysteretic nonlinear elastic behavior due to highly anisotropic deformation of individual grains by basal plane slip and kinking (**Figure 1.10**) and most likely inhomogeneous stress distribution. Considerable bending and kinking of individual grains has been widely observed in different polycrystalline MAX phases (e.g. Ti_3SiC_2, Ti_2AlC, Ti_3AlC_2, Cr_2AlC, etc. [69-75]. For example, in Ti_2AlC, stress-strain response is non-linear and the first stress-strain hysteresis loop is open, irreversible and irreproducible [76]. **Figure 1.11(a)** shows a simple stress-strain curve in Ti_3SiC_2 under repeated and cyclical compression at room temperature. Unlike in common ceramic and metallic materials, namely Al_2O_3 and Al alloy, the repeated stress-strain curve of Ti_3SiC_2 forms reversible hysteretic loop and the size of the closed loop was dependent on the grain size [74]. A sample cycled 100 times shows very similar hysteretic stress-strain loops as the sample cycled only 1 time, as seen in **Figure 1.11(b)**. To explain these results, the formation, growth and annihilation of incipient kink bands

(IKBs) is propsoed [74]. However, IKB model is not the only one used to explain the hysteretic behavior in MAX phases. Instead, Poon *et al.* [77] used an alternate model, which explained the nonlinear hysteretic behavior of MAX phases by formation of microcracks and energy dissipation due to friction between crack surfaces during cyclic loading. Recently it was postulated that ripplocations and not dislocations are responsible for the energy dissipation in layered solid in general and the MAX phases in particular [78].

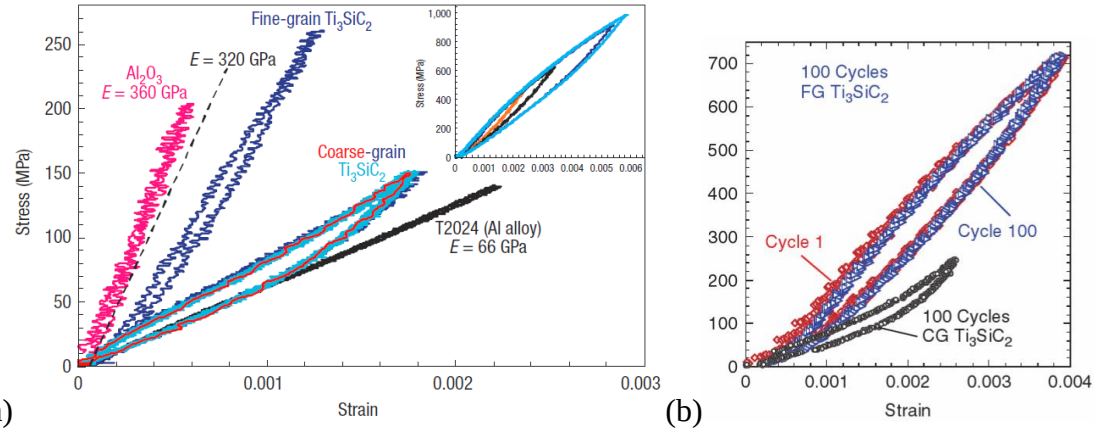

Figure 1.11 (a) Stress-strain curves of fine and coarse-grained Ti_3SiC_2, Al_2O_3 and Al alloy. The dashed line is the linear elastic response expected from Ti_3SiC_2 without having kinking. (b) Stress-strain curves of fine and coarse-grained Ti_3SiC_2 cycled 100 times. [74]

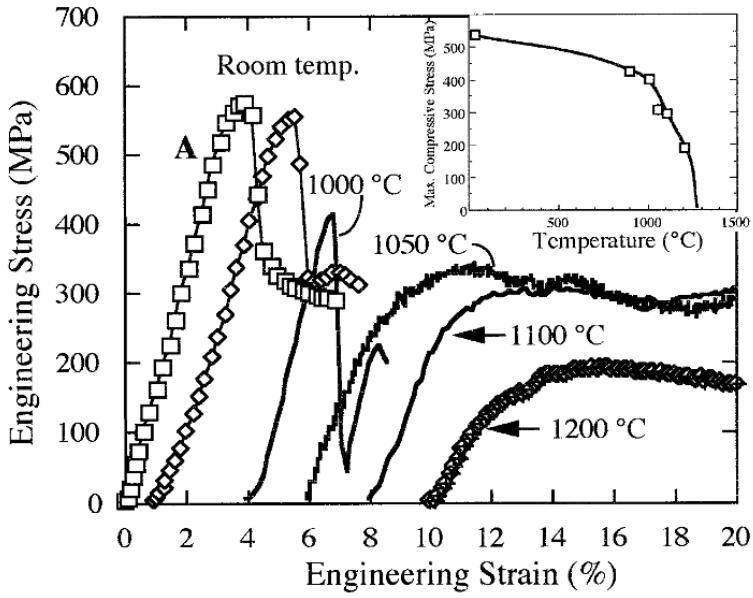

Figure 1.12 Typical compressive engineering stress–strain curves, as a function of temperature. Sample dimensions were; 2 mm × 32 mm in cross section and 2.5 mm high. Initial strain rate was 10^{-4} s^{-1}. Inset shows the ultimate compressive stress versus temperature [79].

At high temperatures, the MAX phases go through a brittle-to-plastic transition (BPT). In quasi-static mechanical tests, the response of MAX phases to tensile stresses are brittle at lower temperatures and high strain rate but can be significant plastic at higher temperatures and lower strain rates due to the creep [80]. For example, **Figure 1.12** shows that a typical stress–strain curves of a Ti_3AlC_2 sample obtained in compression at room temperature, 1000,1050, 1100 and 1200°C [79]. As it can be seen in that figure, that the Ultimate Compressive Strength (UCS) drops and the material becomes more plastic above the BPT temperature (BPTT) at around 1000 °C. This behavior has been observed in other MAX phases too and was attributed to the easier slip and lower stresses required for the transition of IKBs to KBs at higher temperatures

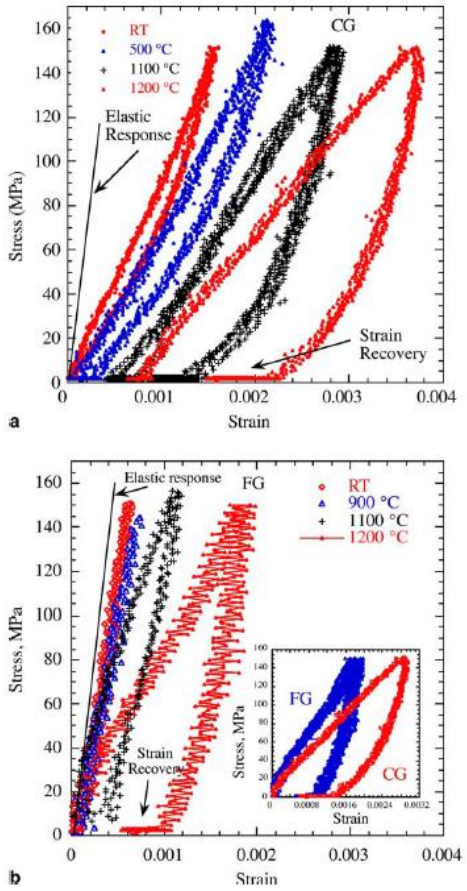

Figure 1.13 Temperature dependence of cyclic stress–strain curves for: (a) CG and (b) FG Ti3SiC2 samples. Inset in b compares the first cycles for both microstructures. [81]

Figure 1.13 shows typical cyclic compression results for CG and FG Ti_3AlC_2 samples, respectively [81]. Unlike to the fully reversible cyclic stress-strain loops at room temperature, the loops become open and no longer fully reversible at above BPTT and the strain continues to recover after complete unloading. The larger loop in the CG samples indicates higher preferential for formation of KBs in CG than in the FG samples. During cycling, the grains breakdown into smaller grains due to accumulation

of KBs, leading to the cycling hardening due to grain refinement, as it is illustrated in.

Figure 1.14.

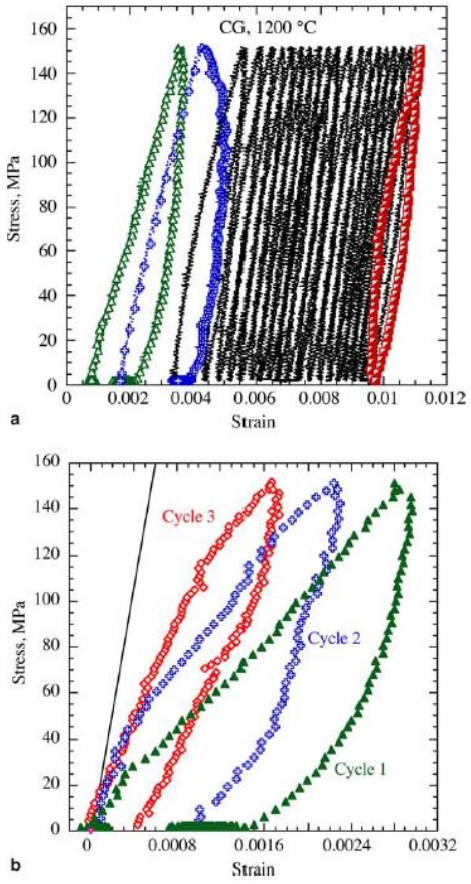

Figure 1.14 Compressive cyclic loading of a CG cylinder at 1200 °C. (a) totality of cycles; (b) comparison of cycles 1, 2 and 21, in (a). In (b) all cycles start at the origin. Solid inclined line represents a Young's modulus of E = 270 GPa, which is the expected linear elastic response at that temperature based on ultrasound measurements. [81]

With nano-laminated structures consisting of strong M-B bonds between M and B atoms and weak M-A bonds similar to MAX phases, some MAB phases are also expected to have similar combination of properties such as high stiffness [59, 60] like other binary ceramics and good electrical and thermal conductivity [82, 83] like metals.

Kota et al. reported the room temperature ultimate compressive strength (UCS) of hot-pressed MoAlB as high as 1940 MPa perpendicular and 1420 MPa parallel to the hot-pressing directions [58], which is confirmed by Xu et al. [61]. In contrast, the UCS of Fe_2AlB_2 is reported to be 2082 MPa perpendicular and 1992 MPa parallel to the hot-pressing directions [84]. Properties like elastic constants [83, 85, 86], thermal conductivity [87] and thermal expansion [88] are also found to be anisotropic in some MAB phases. In Cr_2AlB_2, *ab initio* DFT calculations predict the value of C_{11} is larger than C_{22} and C_{33}, which could be attributed to the structural anisotropy in MAB grains where more B-B units stack along the a-axis direction. In analogous to MAX phases, MoAlB and WAlB prefers basal plane shears and cleavage, originated from basal plane failure due to weakly bonded Al-Al bilayers and M-A layers [89]. In addition, the zigzag boride chains in MAB phases reported by Ade and Hillebrecht may also cause different mechanical responses from MAX phases [28]. To the best of our knowledge, mechanical properties of any of MAB phases at elevated temperature has never been reproted in the open literature, although this class of materials has great potential for structural applications at high temperature in oxidizing environments.

1.5 Research Objectives

The main research objective of this study is to fill in the knowledge gaps that are needed to better understand oxidation resistance of oxidation resistance and mechanical properties of MAX and MAB that is needed to foster their application as a high temperature structural materials or coatings for oxidizing environments. The specific research objectives are summarized as followings:

1. Experimentally study the breakaway oxidation in wedge-shaped Ti_2AlC samples at different temperatures and time. Compositions and phase transformation of Ti_2AlC after Al depletion are analyzed.
2. Evaluated the performance of Ti_2AlC as an environmental barrier coating for Ti alloys. The same wedge shaped Ti_2AlC coating is oxidized to predict the critical thickness for different temperatures.
3. Investigate the effect of impurities in Cr_2AlC contributing to the morphology and spallation of the formed oxide and study the breakaway oxidation of Cr_2AlC using the wedge-shaped samples.
4. Explore the oxidation resistance and Al_2O_3 forming mechanism of MoAlB and study its mechanical responses under quasi-static and cyclic loads at elevated temperatures.

2. BREAKAWAY OXIDATION IN WEDGE-SHAPED TI_2ALC

2.1 Literature Review

Among the alumina-forming MAX phases, Ti_2AlC is one of the most widely studied, and it is, by far, the most attractive for practical applications because it forms protective oxide layer that is resistant to thermal cycling. Wang et al. [39] first demonstrated that Ti_2AlC forms thin α-Al_2O_3+TiO_2 outer scale, and dense protective α-Al_2O_3 inner scale after relatively short (20 hours) exposures to oxidizing environments within the 1000-1300 °C temperature range. They suggested that the chemical activity and diffusivity of Al in Ti_2AlC are large enough to result in preferential oxidation of Al into protective a α-Al_2O_3 passivating layer: as soon as Ti_2AlC is exposed to an oxidizing environment, Al readily comes out of the Ti_2AlC (because of its high chemical activity) and diffuses fast towards the oxygen-facing surface (because of its high atomic mobility). Sundberg et al [44] demonstrated excellent thermal cycling resistance of Al_2O_3 protective oxide scale formed on Ti_2AlC, since it did not spall off even after 8000 thermal cycles to 1350 °C. Good thermal cycling resistance of the Al_2O_3 protective oxide scale can be attributed to its good adhesion to Ti_2AlC and the close matching between thermal expansion of Ti_2AlC (9-9.6 $\times 10^{-6}$ °C^{-1}) and that of α-Al_2O_3 (7.9 $\times 10^{-6}$ - 8.8 $\times 10^{-6}$ °C^{-1}). [39, 40] The latter results in the development of slightly compressive stresses in alumina scale formed on Ti_2AlC, upon its cooling from elevated temperatures [39, 40]. These compressive stresses can be expected to positively contribute to the fracture toughness of the coating.

It is well established by now that the oxidation kinetics of Ti_2AlC follows cubic oxidation law during long-term oxidation in 1000-1300 °C temperature range, both in air and steam. [48] For example, Tallman et al [31] demonstrated cubic oxidation kinetics of Ti_2AlC exposed to 1200 °C for almost 3000 hours. Recently, Smialek [90] showed that after short transient regime with linear oxidation kinetics, in which mixed Al_2O_3+TiO_2 oxide scale forms, only pure α-Al_2O_3 scale continues to grow following cubic oxidation kinetics controlled by inward diffusion of oxygen trough grain boundaries in α-Al_2O_3 scale—the $t^{1/3}$ behavior is typical of any system in which a reaction product layer grows as a result of the competition between grain boundary diffusion and microstructure coarsening [91]. As a result, activation energy for oxidation of Ti_2AlC is almost identical to that found for other alumina forming alloys. [55] Most recently, another important implication of formation of adherent α-Al_2O_3 layer during oxidation of Ti_2AlC at elevated temperature has been demonstrated, since eventual cracks in Ti_2AlC exposed to air can be easily filed in with α-Al_2O_3. [41, 42, 92] The later leads in high-temperature self-healing of small cracks in Ti_2AlC and consequently improvements in the flexural strength of the samples containing small cracks after their oxidation.

While Ti_2AlC has remarkable oxidation resistance, other Al-based MAX phases such as Ti_3AlC_2 show catastrophic breakaway oxidation and formation of mixed α-Al_2O_3+TiO_2 scale after long-term oxidation [31, 54], in a similar fashion to some alumina-forming alloys [34-36]. It is well-established by now that every alumina-forming system must contain a critical Al content below which the selective oxidation of Al to form a predominantly Al_2O_3 scale is not possible anymore [55]. For Ti_3AlC_2, Li et

al [54] showed that decrease of Al content below 5.99% causes oxidation breakaway due to formation of TiC binary carbides. Similarly, it has been shown that quick depletion of Al on the surface of Cr_2AlC results in formation of Cr_7C_3 binary carbides in depilated zone below Al_2O_3 oxide scale [31, 56]. To the best of our knowledge, no breakaway oxidation studies of Ti_2AlC have been reported thus far, although this MAX phase is considered to be one of the best alumina-formers. [40] To find experimentally the conditions at which breakaway oxidation occurs in bulk MAX phases is not a trivial task since it can require more than 3000 h of exposure to air at high-temperature to detect breakaway oxidation, as in the case for Ti_3AlC_2 [54]. An alternative approach for studying oxidation breakaway in MAX phases is to use wedge-shaped samples. The approach was used successfully to study oxidation breakaway in FeCrAl base alloys [57]. Hence, the approach would appear to offer considerable potential to find out the critical breakaway oxidation conditions for Ti_2AlC.

This paper reports on the investigation of breakaway oxidation of Ti_2AlC. For the purpose of a better understanding of breakaway oxidation mechanism, wedge-shaped Ti_2AlC samples were exposed to static air at temperatures ranging from 1000 to 1300 °C for different times. Based on the analysis of the phase composition of the oxidized wedges specimens and the breakaway oxidation mechanism of Ti_2AlC is proposed. The products of the oxidation are further rationalized using a thermodynamic analysis based on Density Functional Theory (DFT)-derived energetic analysis of all phases likely to take part in these oxidation reactions.

2.2 Experimental Methods

Ti_2AlC powders were reaction-synthesized using a procedure described in more detail elsewhere [73, 76]. Briefly, Ti (99.5%, -325 mesh) Al (99.5%, -325 mesh) and TiC (99.5%, 2μm) (all from Alpha Aesar, USA) were mixed in molar ratio of Ti:Al:TiC = 1.00:1.05:0.95 and ball-milled for 24 h at 300 rmp in a glass jar using ZrO_2 balls. The powder mixture was poured into an alumina crucible (AdValue Technology, US), placed into a tube furnace (MTI Corporation, CA), and heated to 1400°C at heating rate of 10 °C/min under flowing ultra-high purity argon (UHP-Ar). After reaction synthesis of the powder mixture at 1400 °C for 4 h, porous Ti_2AlC was drilled milled into a powder form and sieved to particle sizes below 90 μm. Subsequently, the Ti_2AlC powder was poured into a 20 mm diameter graphite die, and densified using Pulsed Electric Current Assisted Sintering (PECAS, model DCS25, Thermal Technology LLC, CA), commonly referred to as Spark Plasma Sintering (SPS), at 1400 °C for 15 min under pressure of 100 MPa in flowing UHP Ar. Final samples were 95vol.% phase pure with 3vol.% $TiAl_x$ and 2vol.% of Al_2O_3 as determined by XRD, SEM and EBSD and describe in more details elsewhere [73, 76]. $TiAl_y$ impurities were found to be mostly clustered around triple grain boundary junctions.

Fully dense Ti_2AlC discs were sliced by wire Electrical Discharge Machining (EDM) into 2 mm thick discs with 19.6 mm diameter. Subsequently the EDM layers were removed, followed by mechanical polishing to 0.1 μm diamond paste finish. Those discs were further bonded to larger aluminum discs using crystalbond (Ted Pella, CA), and polished under the angle to form wedge sample with a 3.5±0.2° taper and the

thickness ranging from ~10-20 μm at the very tip of the wedge, to 500 μm at the opposite end. After removal from the aluminum support disk by washing in acetone, wedge-shaped Ti_2AlC specimens were placed on alumina plate and inserted to the preheated box furnace (Carbolite, UK) for further oxidation. Wedge-shaped samples were oxidized at various temperatures (i.e. 1000, 1100, 1200 and 1300 °C) in ambient air and removed from the furnace after being oxidized for different times (i.e. 5 min, 10 min, 15 min, 30 min, 45 min, 1 h, 2 h and 10 h). Note here that all samples were placed in the preheated furnace and removed from the hot furnace after completed oxidation to avoid additional oxidation during heating and cooling of the furnace. Although this method results in the rapid heating and cooling of the samples, no cracking or spallation of the oxide layer was observed, demonstrating once again excellent thermal shock resistance and passivating coating adherence of oxidized Ti_2AlC.

The wedge-shaped Ti_2AlC samples were mounted in epoxy after oxidation, and their cross section was mechanically polished to 0.1 μm diamond paste finish. Scanning Electron Microscope (SEM, Quanta 600 FEG, FEI, OR, USA), equipped with Energy Dispersive Spectroscopy (EDS, Oxford Instruments, UK) was used to analyze the microstructure and composition of phases along the wedge and the average critical thickness was measured from SEM images (see below). Electron microprobe analysis (EPMA, Cameca SXFive, Cameca, WI) was used for a quantitative phase evaluation in the breakaway oxidation region in Ti_2AlC.

2.3 Results and Discussion

2.3.1 Phase characterization of Ti_2AlC

Analysis of the XRD results for fully-dense Ti_2AlC samples prepared in this study confirmed that all samples were phase pure, and no Ti_3AlC_2 as secondary phase was observed, **Figure 2.1**. However, SEM and EDS results presented in **Figure 2.2** and **Table 2-1**, reveal the presence of the small amount of $TiAl_x$ (dark gray phase containing only Ti and Al) apart from Ti_2AlC phase (light gray phase with Ti:Al:C atomic ratio close to 2:1:1) disc. As amount of $TiAl_x$ phase in Ti_2AlC samples was very low since, it is not surprising this phase was are observed in XRD result.

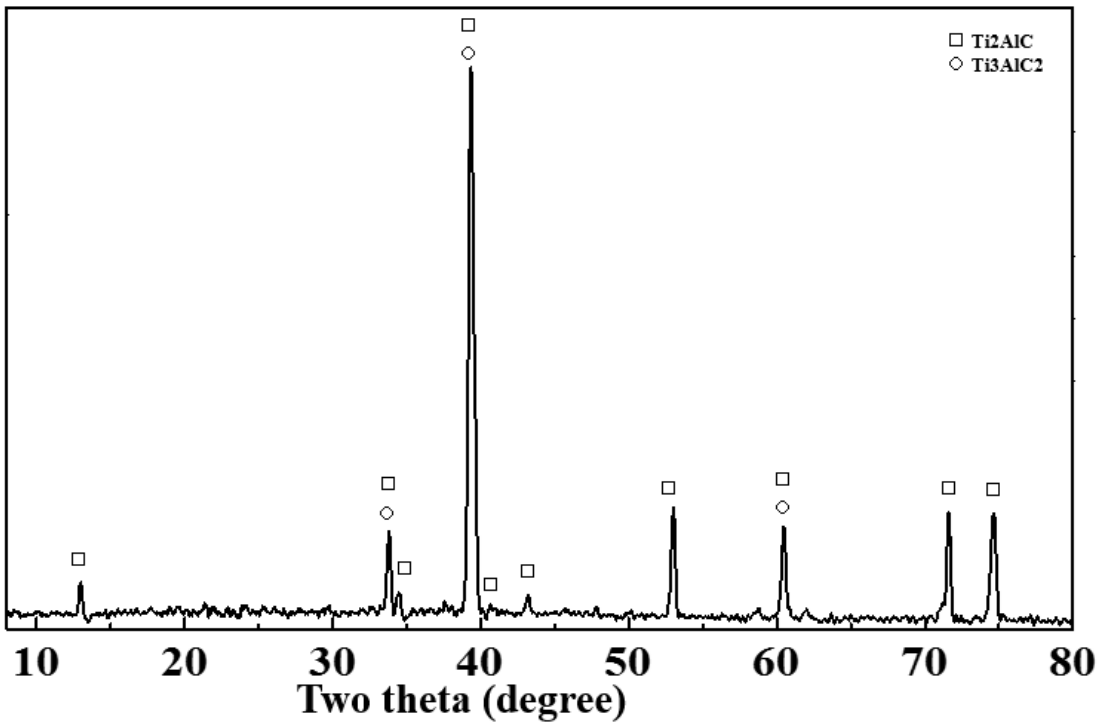

Figure 2.1 XRD result of produced Ti_2AlC disc

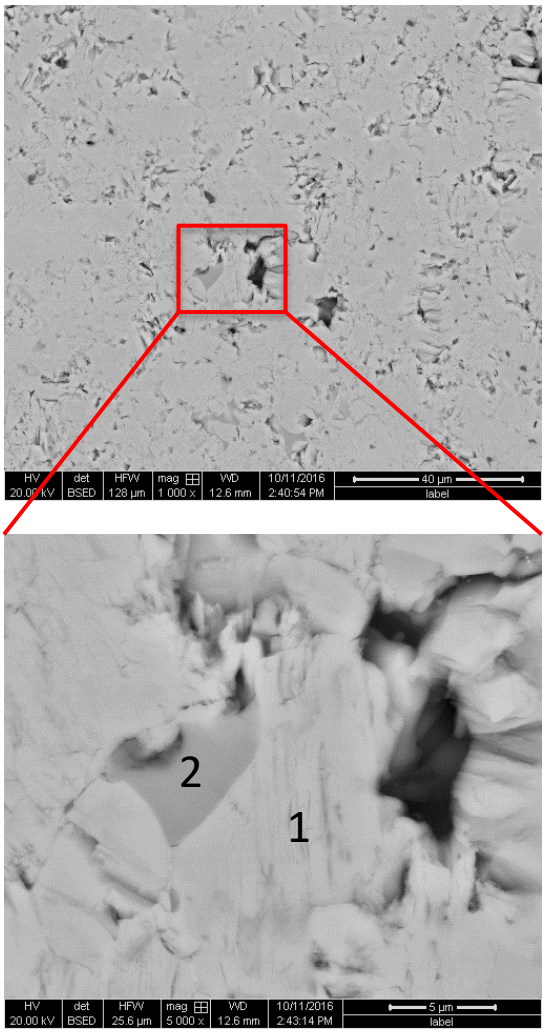

Figure 2.2 Back-scattered electrons SEM images of Ti_2AlC samples sintered in this study.

Table 2-1 EDS results of spots indicated in Figure 2.2

Spot	Ti	Al	C
Bright	46.36	24.40	29.25
Dark	43.62	56.37	

2.3.2 Experimental characterization of oxidized wedge-shaped Ti_2AlC

Figure 2.3 shows SEM backscatter electron (BSE) images of three selected wedge-shaped Ti_2AlC samples oxidized at 1000 °C (**Figure 2.3**a), 1100 °C (**Figure**

2.3b) and 1200 °C (**Figure 2.3**c) for 30 min, respectively. SEM results in **Figure 2.3** together with EDS results (not shown here) suggest that wedge-shaped samples can be divided in the following regions based on its phase composition after oxidation:

Region I with thin protective, predominately alumina oxide layer on Ti_2AlC;

Region II with titania nodules in otherwise continuous, thin predominantly-alumina oxide scale on Ti_2AlC;

Region III with thick alumina and titania oxide layer on decomposed Ti_2AlC;

Region IV with continuous thick alumina and titania oxide layer on the surface of TiO_y oxide with some TiC in the middle;

Region V with containing only alumina and titania oxide mixture.

Note here that boundaries between different regions shift along the wedge-sample towards the ticker end of the sample with increasing temperature or time, as it is illustrated in **Figure 2.3** for samples oxidized for 30 min at 1000, 1100 and 1200 °C.

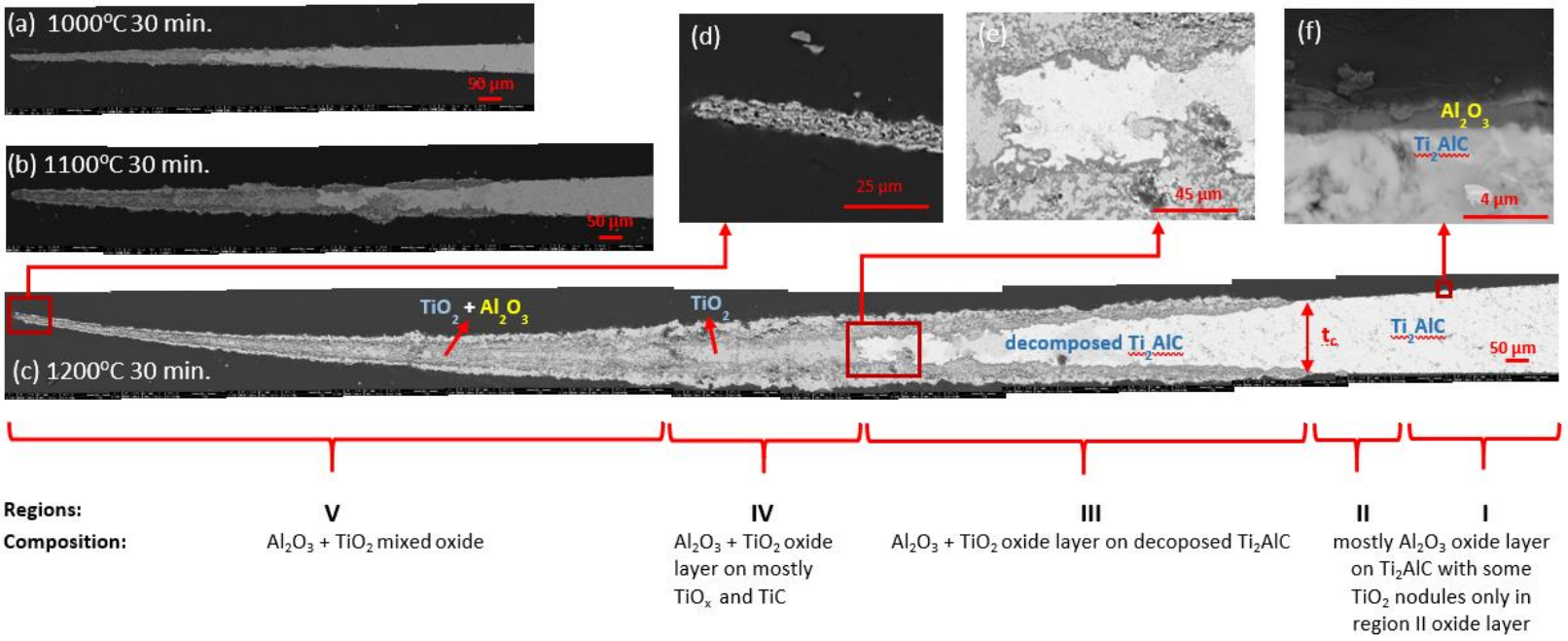

Figure 2.3 Backscattered Electron SEM images of selected wedge-shaped Ti_2AlC oxidized at (a) 1000, (b) 1100 and (c) 1200 °C for 30 min. Insert (d), (e) and (f) shows magnified tip, middle and end, respectively, of the wedge-shaped sample oxidized at 1200 °C for 30 min.

2.3.3 Regions I and II

The fact that thin protective Al_2O_3 oxide scale (only with small amount of Ti detected in EDS) forms in Region I and II is in good agreement with previously published results on oxidation of bulk Ti_2AlC samples in the same temperature range [31, 39, 40, 48, 53, 93]. Note here that eventual Al depletion in Ti_2AlC determined using EDS was below the level that can be accurately determined using this method. This is in good agreement with TEM results reported by Lin et al. [93] showing minimal Al depletion at the oxide/substrate interface.

The thickness of the Al_2O_3 oxide scale was more or less uniform in *Regions I and II,* and is plotted as a function of time for different oxidation temperatures in **Figure 2.4**a, together previous results obtained by oxidation of bulk Ti_2AlC. Since previous results on oxidation of bulk Ti_2AlC showed that oxidation kinetic follows cubic law [31, 39, 40, 48, 90], results obtained in this study are fitted using following equation:

$$x^3 = k_x \cdot t \tag{2.1}$$

where x is thickness of the oxide layer, t is time and k_x is cubic law constant that can be expressed as:

$$k_x = k_{x0} exp\left[-\frac{Q}{RT}\right] \tag{2.2}$$

where Q is activation energy and T is temperature. As shown in **Table 2-2**, least-squares fit of the results using Eq. (2.1) resulted in an $R^2 > 0.926$. More importantly, when k_x values provided in **Table 2-2** are plotted vs. 1/T on the Arrhenius plot (**Figure 2.4**b)

activation energy *Q* of 331 kJ/mol can be determined. This value is quite close to the previously reported activation energies for oxidation of bulk Ti_2AlC [53].

Since the activation energy, *Q*, and thicknesses of the oxide scale determined in this study (**Figure 2.4**) are quite close to those obtained from the oxidation of bulk samples, it is reasonable to conclude that the oxidation of wedge-shaped Ti_2AlC at *Region I* is indeed very similar to that of bulk Ti_2AlC, and not affected by any eventual diffusion of Al along the wedge-shaped specimen to Al depilated regions in the thinner part of the sample (*Regions II-V*). However, while Al_2O_3 forms continuous protective layer in *Region I*, it is interrupted in *Region II* by nodules of mixed oxides (Al_2O_3+TiO_z). It is not completely clear why nodules of the mixed Al_2O_3+TiO_z oxide form in the *Region II*, but it can be speculated at this moment that they form in the regions having larger cluster of $TiAl_y$ inclusions at or near the surface of the sample.

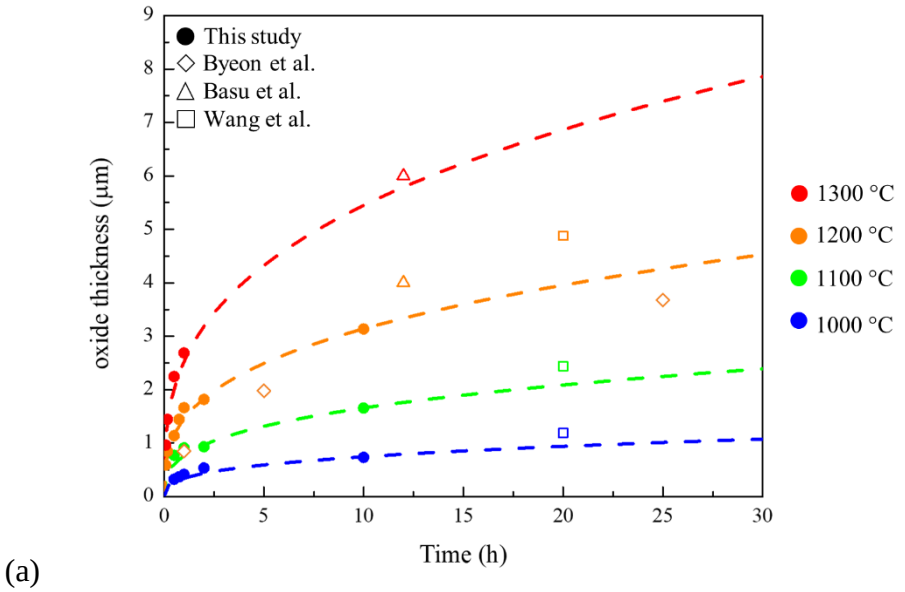

(a)

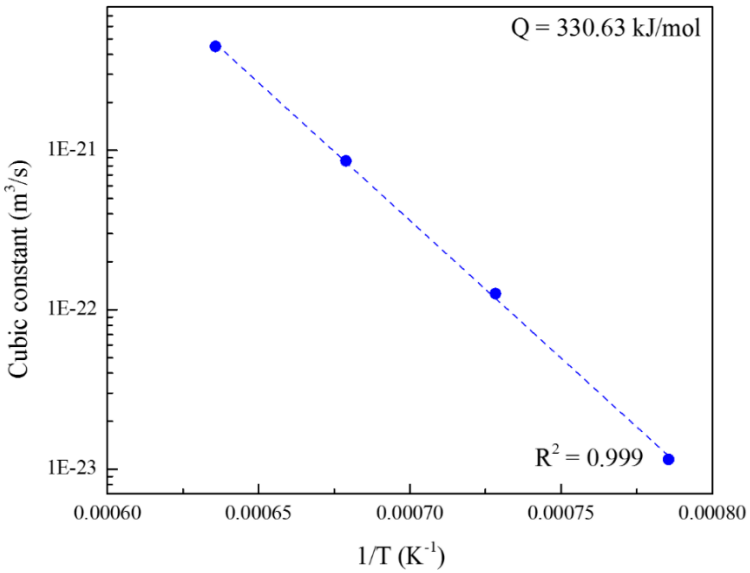

(b)

Figure 2.4 (a) Thickness of Al_2O_3 layer in the *Region I* vs. time for different oxidation temperatures with results of the fitting assuming cubic oxidation kinetics (dashed lines). For comparisons, results reported by Byeon et al. [40], Basu et al. [48] and Wang et al. [39] are also plotted as open symbols. (b) Arrhenius plot for the Al_2O_3 layer obtained from fitting experimental results with the cubic oxidation kinetic.

Table 2-2 Summary of k_x and R^2 for oxidation of Ti_2AlC at different temperatures.

	1000 °C	1100 °C	1200 °C	1300 °C
$k_x(m^3/s)$	$1.15x10^{-23}$	$1.26\ x10^{-22}$	$8.60\ x10^{-22}$	$4.49\ x10^{-21}$
R^2	0.9262	0.9861	0.9961	0.9409

2.3.4 Region III

As shown in **Figure 2.3**, the oxide layer in *Region III* is significantly ticker that that in *Regions I and II,* and consist of predominately Al_2O_3 scale on the surface, and relatively thick mixed Al_2O_3+TiO_z subscale. In addition, same decomposition of Ti_2AlC can be observed, that becomes more obvious close to the thinner end of the sample.

To further identify phase present in *Region III,* EPMA analysis is performed on wedge-shaped Ti_2AlC sample oxidized at 1200 °C for 30 minutes, **Figure 2.5** and **Figure 2.6**. Ti, Al, O and C maps on **Figure 2.6**b-e confirm that oxide scale in this region contains of mixture of aluminum-oxide and titanium-oxide. More importantly, **Figure 2.5** shows decomposition of Ti_2AlC to Ti_3AlC_2 as indicated by regions with Ti/Al ratio ~3 (green in **Figure 2.5**f) and Ti/C ratio ~1.5 (green in **Figure 2.5**g). In addition, further decomposition of Ti_2AlC to TiC can be also seen as overlap of dark blue regions in **Figure 2.5**c with very little Al, green region in **Figure 2.5**e with ~50% C, and dark purple region in **Figure 2.5**g with Ti/C atomic ratio ~1. As it can be seen in **Figure 2.6**, the amount of Ti_3AlC_2 and TiC phases in the substrate, seems to increase significantly in *Region III* as one looks closer at the elemental maps close to boundary with *Region IV*.

Results presented here clearly show that oxidation mechanism in *Region III* breaks away from that of bulk Ti_2AlC since thick mixed oxide layer forms in this region. This mixed oxide layer obviously forms primarily as a result of oxidation of Al deficient phases, such as Ti_3AlC_2 and TiC. Therefore, it is reasonably to conclude that breakaway oxidation occurs at some critical thickness, (t_C in **Figure 2.3**) where Al depleted $Ti_2Al_{1-x}C$ starts to decompose to Ti_3AlC_2 and TiC. Note here, that that critical thickness, or thickness of the wedge-shaped sample at the border between Regions II and III, increases with increasing oxidation temperature and/or time.

For the known critical thickness, t_C, and thickness of the alumina scale layer in *Regions I* and *II*, t_o, critical Al deficiency, x, in $Ti_2Al_{1-x}C$ at which oxidation mechanisms breaks away from that observed in bulk can be determined as:

$$x = \frac{mols\ of\ Al\ in\ Al_2O_3\ layer}{mols\ of\ Al\ in\ Ti_2AlC\ substrate} = \frac{2 \cdot \rho_{Al_2O_3} \cdot t_a / M_{Al_2O_3}}{\rho_{Ti_2AlC} \cdot t_C / M_{Ti_2AlC}} \quad (2.3)$$

Where $\rho_{Al_2O_3}$ and ρ_{Ti_2AlC} are densities of Al_2O_3 and Ti_2AlC, respectively and $M_{Al_2O_3}$ and M_{Ti_2AlC} are molecular masses of Al_2O_3 and Ti_2AlC, respectively. As shown in **Figure 2.7**, using eq. 2.3 and critical thickens and thickness of the oxide layer in *Regions I* and *II* measured for all samples tested in this study, critical Al deficiency that results in breakaway oxidation was found to be approximately 0.05 (or 5%), regardless of the oxidation temperature and time. Note here that standard deviations and scattering are much larger for results obtained at shorter oxidation times mostly due to larger variation in the thickness of the oxide layer in *Regions I* and *II*. With longer time, i.e. 10 hours, the critical Al converge to value between 0.045 and 0.055.

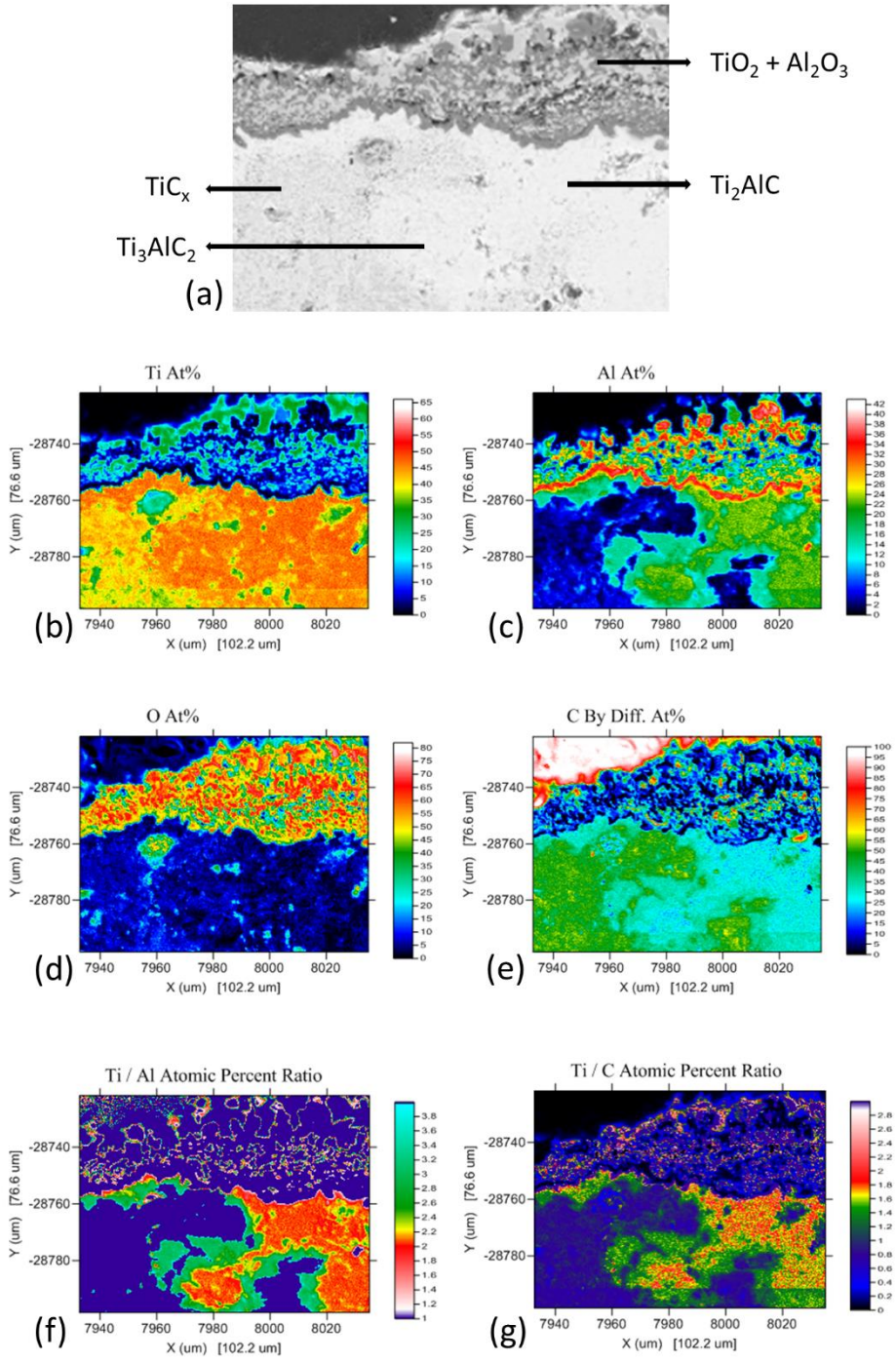

Figure 2.5 (a) Back scattered SEM image in *region III* and EPMA maps for (b) Ti, (c) Al, (d) O, (e) C (f) Ti/Al atomic ratio and (g) Ti/C atomic ratio.

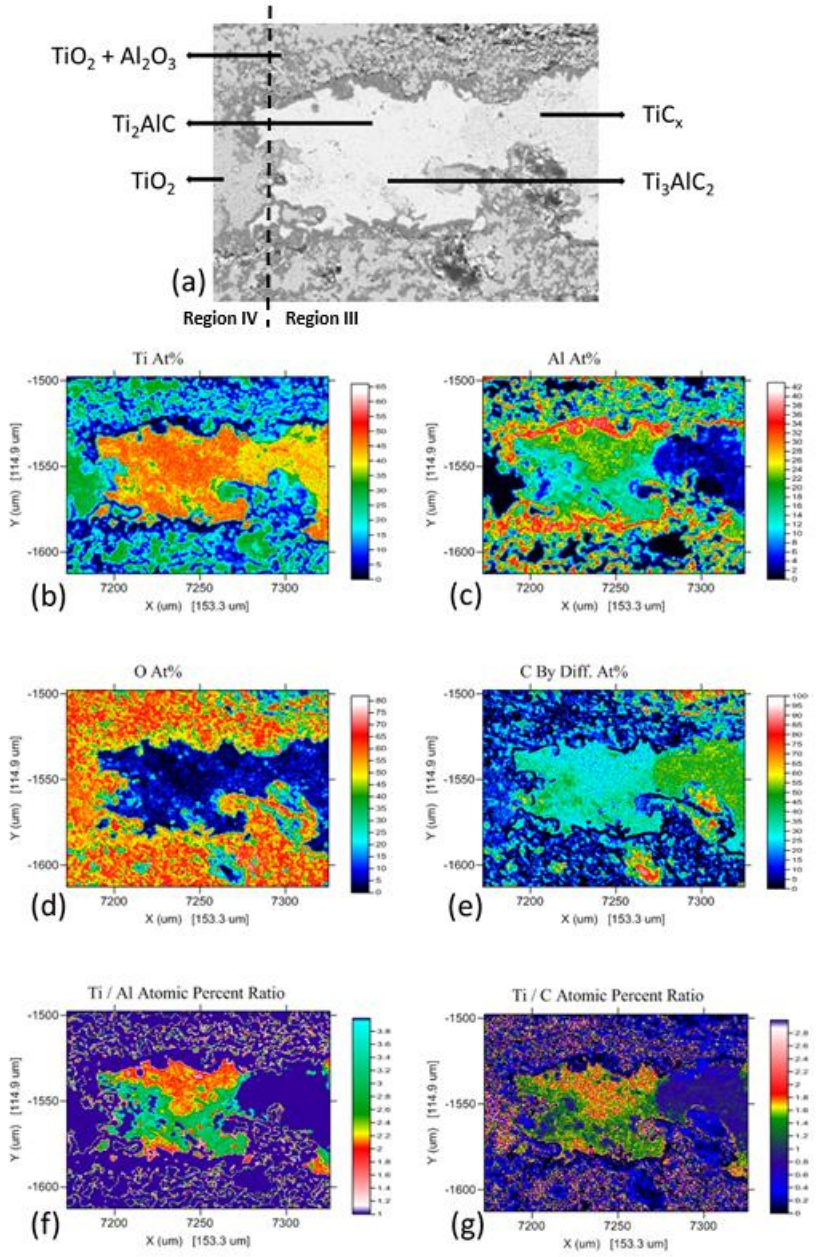

Figure 2.6 (a) Back scattered SEM image of *Regions III* and *IV*, together with EPMA maps for (b) Ti, (c) Al, (d) O, (e) C (f) Ti/Al atomic ratio and (g) Ti/C atomic ratio.

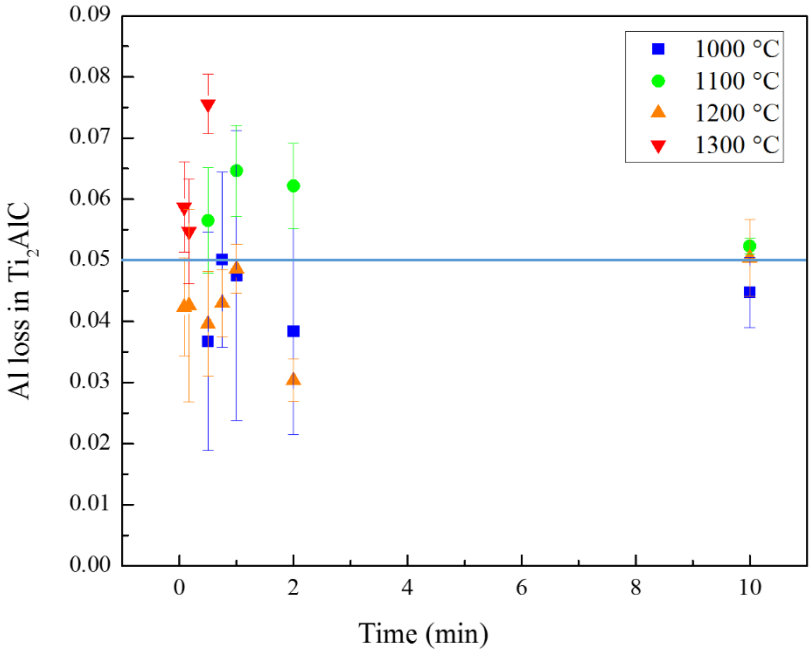

Figure 2.7 Critical Al loss, x, in $Ti_2Al_{1-x}C$ that leads to breakaway oxidation.

2.3.5 Regions IV and V

Region IV consist of a thick mixed oxide on the surface, similar to that observed in *Region III*, **Figure 2.3**. However, unlike in *Region III*, no Ti_2AlC, or any other Al-depleted carbide phase can be identified below the oxide surface layer, as it can be seen from EPMA results in **Figure 2.6**. The only phase present in the middle of the wedge-shaped sample in this region is titanium-oxide, **Figure 2.6**. At the very tip of the wedge-shaped sample (*Region V*) where Al depletion of Ti_2AlC is very fast, only mixed oxide layer can be observed. Interestingly enough, even after oxidation for only 5 min. at 1000 °C (not shown here) the very tip of the wedge-shaped sample was completely oxidized (*Region V*) to mixture of Al_2O_3 and TiO_2.

Results presented in this section clearly indicate that that Al deficiency of approximately 5% in Ti_2AlC leads to the breakaway oxidation, i.e. formation of alumina and titania oxide, instead of protective predominately Al_2O_3 oxide layer. Experimental results also suggest that the breakaway oxidation is caused by gradual decomposition of Al deficient $Ti_2Al_{1-x}C$, to Ti_3AlC_2 and further to TiC and subsequent oxidation of those phases to form mixed oxide.

2.4 Summary

Results of this study reviled existence of five different phase regions on the wedge-shaped Ti_2AlC samples oxidized in 1000-1300 °C temperature range for different times ranging from 5 min. to 10h. In regions *I* and *II* at the thickest end of the wedge-shaped sample, a thin and protective, predominantly Al_2O_3 scale forms on the surface without any visible decomposition of Al deficient Ti_2AlC substrate. Moving toward the tip of the sample, the *Region III* can be observed with the ticker Al_2O_3 and TiO_y mixed oxide scale on the surface of the wedge-shaped sample, and decomposed Al depleted Ti_2AlC substrate to Ti_3AlC_2 and TiC phases. Breakaway oxidation was found to occur between Regions II and III when Al deficiency in Ti_2AlC reaches approximately 5%. Close to the tip of the wedge-shape samples (Regions IV and V), no Ti_2AlC or any other carbide phase can be detected anymore, as sample completely oxide forming ticker Al_2O_3 and TiO_y mixed oxide scale on the surface and TiO_2 in the middle of the sample (*Region IV)*, or only Al_2O_3 and TiO_y mixed oxide throughout the thickness at the very tip of the wedge-shaped sample (*Region V*).

3. EVALUATION OF TI_2ALC AS ENVIRONMENTAL BARRIER COATING FOR TI-6242 ALLOYS

3.1 Literature Review

Titanium alloys are widely used for aerospace and biomedical applications because of their high specific strength and good corrosion resistance when compared, for example to steels and aluminum alloys [94]. At low temperatures, pure titanium has a hexagonal close packed (hcp) structure, referred to as α-Ti phase and it transforms to body centered cubic (bcc) structure, referred to as β-Ti phase above 882 °C [95]. The most common commercial titanium alloys contain predominantly α phase, and have yield strengths from 170 to 480 MPa which is close to that of the annealed 300 series stainless steels, but with 40% lower density. Those commercially available α-Ti alloys also have good formability and weldability and excellent corrosion resistance. The properties of of Ti alloys can be further improved by alloying to stabilize β phase. Therefore, all Ti-alloys can be classified as α, near-α, α/β and β phases based on the amount of β phases present in their microstructure. A Ti64 alloyed with 6%Al and 4%V, is typical example and most commonly used Ti-alloy with α/β microstructure predominantly due to its good mechanical priorities at room temperature. However, its creep resistance even at low temperatures ($T/T_m<0.2$) is quite poor limiting its application at elevated temperatures [96]. In this study, a near-α Ti6242 alloyed with 6%Al, 2%Sn, 4%Zr and 2%Mo, is chosen since it has a good creep resistance up to ~800 °C, and thus it is preferred light-weight alloy for elevated temperature applications such as gas turbines [94]. However, the maximum operation temperature of Ti6242 is still

limited up to ~500°C due to its poor oxidation resistance. Above 500°C temperature, a non-protective TiO_2 layer forms on Ti6242 when it is exposed to oxidizing environments. More importantly, non-protective TiO_2 layer allows easy oxygen diffusion into Ti6242 below oxide layer and causes its embrittlement even at the small amount (of more than 0.14 wt.%) of O dissolved in the α phase [97-101], known as "alpha-case". Protective coatings, such as platinum aluminide [102] and NiCrAlY [103], have been widely studied to reduce the ingress of oxygen into Ti6242 because they lead to the formation of the protective layer of thermally grown oxide (TGO) which, in turn, reduces the oxygen diffusion into Ti6424. However, the shortage of this approach is that the thermal mismatch between the oxide and the metallic substrate triggers the relatively fast spallation of TGO.

$M_{n+1}AX_n$ (MAX) phases are a group of ternary metal ceramics in which M is early transition metal, A is group 13-16 element and X is C and/or N [1-3]. Unlike most of ceramic materials the MAX phases are readily machinable [4, 104]. In addition, they have low density, high strength [4] and excellent thermal shock resistance and damage tolerance [4, 7]. More importantly for their high temperature applications, some of MAX phases containing Al, show good oxidation resistance [31] because they form dense and adherent predominately alumina oxide layer at high temperatures in oxidizing environments. It has been shown recently that oxidation of alumina forming MAX phases follows cubic oxidation kinetics [31, 48] governed by oxygen grain boundary diffusion through alumina scale [53], similar as in the case of FeCrAl and some other alumina-forming alloys [53]. Ti_2AlC is one of the best known alumina-forming MAX

phases and is by far the most attractive for practical applications due to its low density and thermal expansion coefficient of 9-9.6 × 10^{-6} °C^{-1} that is close to that of alumina oxide scale (7.9 × 10^{-6} °C^{-1} - 8.8 × 10^{-6} °C^{-1} [48]. A good matching between thermal expansion coefficients of α-Al_2O_3 and Ti_2AlC results in a good adhesion and exceptional thermal sock resistance of the oxide scale [39, 40]. The oxidation kinetics of Ti_2AlC was also found to be cubic [31, 48], which is crucial for its long-term use at elevated temperatures, and controlled by the rate of oxygen grain-boundary diffusion through alumina scale [53]. The preferential oxidation of Al to form protective, predominately Al_2O_3 oxide scale during oxidation of Ti_2AlC is believed to be governed by high activity and diffusivity of Al in Ti_2AlC [39]. However, it has been shown recently that continuous diffusion of Al form Ti_2AlC to form alumina scale leads eventual to the breakaway oxidation and formation non-protective Al_2O_3+TiO_2 oxide scale, when aluminum content in Ti_2AlC decreases for approximately 5 at.% [105]. Last but not least, Ti_2AlC also have a capability of self-healing and damage repair at elevated temperatures [41] as continuous formation of Al_2O_3 scale fills crack gaps and leads to the recovery of flexural strength of samples containing small surface damages or cracks.

Considering the excellent oxidation resistance of alumina-forming MAX phase, they can be good candidate materials for environmental barrier coatings (EBC) to protect Ti6242 from rapid oxidation at high temperatures. It was shown that Ti6242 coated by Cr_2AlC using industrially sized magnetron sputtering coater exhibited improved oxidation resistance [106] up to 800 °C. However, the Cr_2AlC coatings degraded not only due the diffusion of Al to the oxide scale, but also into Ti6242 substrate. In this

study, we evaluate Ti_2AlC as a EBC for Ti6242 by studding oxidation and interfacial reactions and phase evolution using Ti_2AlC- Ti6242 diffusion joined couples exposed to temperatures of 800 °C and 1000°C and ambient air for different times, ranging from 15 min. to 200 h. Based on the analysis of the phase composition in on the surfaces and across the interfaces, the oxidation mechanism of Ti_2AlC- Ti6242 couples is proposed.

3.2 Experimental Methods

To prepare Ti_2AlC samples, Ti (99.5%, -325 mesh, Alpha Aesar, USA), Al (99.5%, -325 mesh, Alpha Aesar, USA) and TiC (99.5%, 2μm, Alpha Aesar, USA) powders were first mixed in the a 1.05:1.05:0.95 atomic ratio in a glass jar, and ball milled for 24 h by ball milling using zirconia at 300 rmp, following procure described in more details elsewhere [76, 107]. The powder mixtures were poured into an alumina crucible (AdValue Technology, US) and heated at the rate of 10 °C/min to 1400 °C under ultra-high purity Ar (UHP-Ar) in a tube furnace (MTI Corporation, CA), and held at that temperature for 4 h. The reaction sintered Ti_2AlC was removed from alumina crucible, drill milled into the powder, and additionally sieved to obtain powder with particle size below 90 μm. Subsequently the fine Ti_2AlC powders were compacted into a 20 mm dia. graphite die and sintered using Pulsed Electric Current Assisted Sintering (PECAS, model DCS25, Thermal Technology LLC, CA) at 1400 °C in the atmosphere of UHP-Ar for 15 min. using the constant pressure of 100 MPa and heating rate of 50 °C /min.

Full defense Ti_2AlC and Ti6242 (AFRL) samples were cut using wire electrical discharge machining (EDM) into 5 mm thick discs with diameter of 19.6 mm.

Subsequently, both Ti_2AlC and Ti6242 discs where polishing mechanically to 0.1µm diamond paste finish prior to their diffusion joining. Polished Ti6242 and Ti_2AlC discs were then placed inside a graphite die and heated by PECS apparatus to temperatures ranging to 800 or 1000 °C at the heating rate of 50 °C /min under the flowing UHP-Ar, and kept at those temperatures under 5 MPa pressure for 15 min to form Ti_2AlC- Ti6242 diffusion couples. Graphite foil was used to separate Ti6242-Ti_2AlC couples and graphite die in all cases. To investigate the effect of the thickness of Ti_2AlC on oxidation resistance of Ti_2AlC-Ti6242 couples, one Ti6242 disc was sandwiched between two Ti_2AlC discs and diffusion joined using the same procedure. Those sample where further mechanically polished to 0.1µm diamond paste finish, to form Ti_2AlC-Ti6242 couples with tapered (from 0 – 500 µm) Ti_2AlC layers, as it is illustrated in **Figure 3.1**.

Figure 3.1 Ti6242 with wedge-shaped Ti_2AlC layers

Oxidation tests of Ti_2AlC-Ti6242 couples were carried out in a box furnace (Carbolite, UK) at 800 and 1000 °C under the ambient static air for different times (from 15 min. to 200 h). For all oxidation tests, Ti_2AlC-Ti6242 couples were placed in the alumina crucibles heated to targeted temperatures using heating rate of 10 ^oC/min.

The phase composition of the fully densified Ti_2AlC was characterized using X-ray diffraction (XRD, D8 Discover, Bruker, USA) and Scanning Electron Microscopy (SEM, JSM-7500F, JEOL, Tokyo, Japan and FE-SEM, Quanta 600 FEG, FEI, Oregon,

USA) equipped with Energy-Dispersive Spectroscopy (EDS, Oxford Instruments, UK). In addition, SEM with EDS was used to characterize phase composition of Ti6242, and cross-sections of the Ti_2AlC-Ti6242 couples after diffusion bonding and after oxidation tests. All samples for SEM and EDS where prepared by mechanical polishing to 0.1μm diamond paste finish. The acceleration voltage of 20 kV was used for SEM imaging. In addition, Electron Microprobe Analysis (EPMA, Cameca SXFive, Cameca, WI) was used for a quantitative elemental analysis, while Electron-backscatter Diffraction (EBSD, Aztec EDS, Oxford Instruments, UK) was used to study the phase composition across interfaces in Ti_2AlC-Ti6242 couples. Samples for EBSD where additionally polished using 0.05 μm colloidal silica solution. Last but not least, nano-indentation measurements across the Ti_2AlC-Ti6242 interfaces were carried out using Hysitron TI950 Triboindenter (Bruker, USA) using loading force of 2000 μN to changes in elastic modulus and hardness across the interface.

3.3 Results and Discussion

3.3.1 Characterization of starting Ti6242 alloy

Figure 3.2 shows typical microstructure of the Ti6242 alloy used for this study, consisting of lager amount of α phase and smaller amount of β phase. EDS results in **Table 3-1** also show that α phase contains a larger amount of Al which is known to be α stabilizers, while β phases contains lager amount of Mo which is used as β stabilizers in Ti alloys. In addition, EDS results shows that the content of Zr and Sn is almost identical in both phases.

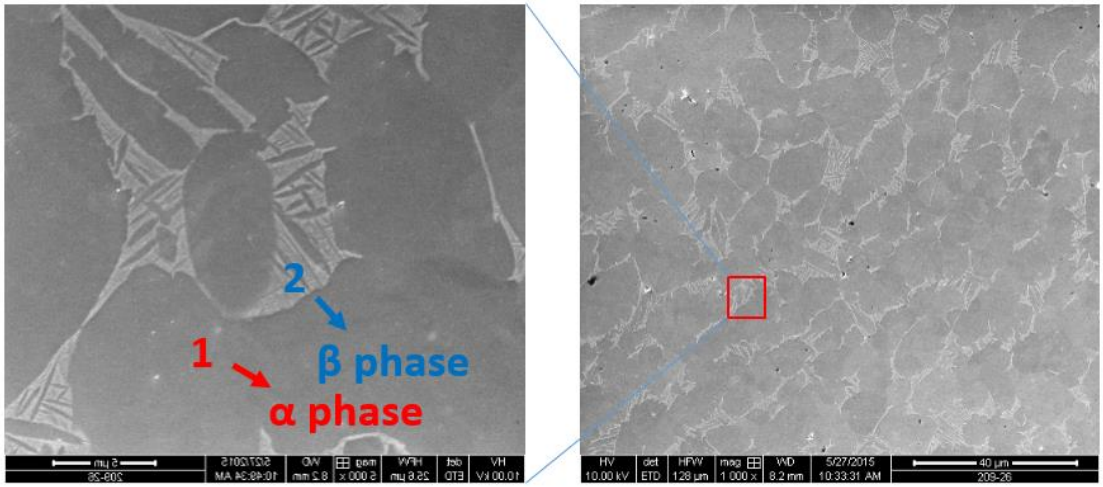

Figure 3.2 Back scattered SEM image of Ti6242 alloy

Table 3-1 Composition analysis of Ti6242 by Electron Microprobe in Figure 3.2

Weight%	Ti	Al	Zr	Mo	Sn
α-Ti phase	87.45	7.06	3.32	0.32	1.85
β-Ti phase	79.92	3.88	3.91	10.09	2.20

3.3.2 Microstructure of the interface in the diffusion bonded Ti6242-Ti_2AlC couples

SEM images in of the of interface in Ti_2AlC-Ti6242 couples in **Figure 3.3** clearly show good diffusion bonding between Ti_2AlC and Ti6242 was achieved at both 800 °C and 1000 °C using PECAS. 1-2 μm thin reaction zone can be observed in the diffusion bonded interface in both samples. EDS results also shows phase compositions typical for β and α phase in Ti6242 (spots 1 and 2 in **Figure 3.3**a) and Ti_2AlC (spots 5 and 6 in **Figure 3.3**a). They also reveal that the reaction interface between Ti_2AlC and Ti6242 (spot 3 in **Figure 3.3**a) contains only Ti and Al, in the atomic ration that is close to 1:1, suggesting that reaction zone should be nearly stoichiometric TiAl. More importantly, EDS results in **Table 3-2** also reveal lower Mo and Zr content and higher

Al content in region between diffusion reaction layer and Ti6242 (spot 3 in **Figure 3.3**a) than in the bulk Ti6242. Note here an absence of any β phase Ti6242 adjacent to the reaction layer. Therefore, results presented in **Figure 3.3** clearly show that the interface between diffusion bonded Ti_2AlC and Ti6242 consists of two sub-layers: (1) reaction layer where new phases form at the interface, and (2) Al-rich sublayer in Ti6242 containing only α phase. Comparison microstructure of the interface between Ti_2AlC and Ti6242 diffusion bonded at 800 and 1000 °C reveals the similar structure in both cases, with slightly thicker reaction layer in the the couple diffusion bonded at 1000 °C. However, the microstructure of Ti6242 after heating to 1000 °C contains significantly less β phase, as expected in Ti6242 samples annealed above temperature of 950 °C [108].

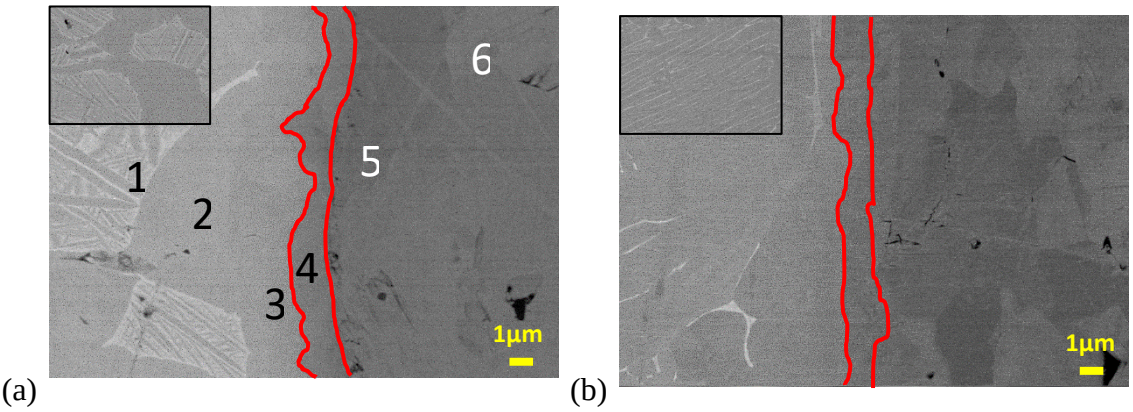

(a) (b)

Figure 3.3 Back-scattered electron SEM image of the interface Ti_2AlC-Ti6242 couples diffusion bonded at (a) 800 °C and (b) 1000 °C for 15 min. Red lines indicate the start and end of the reaction regions in the interface between Ti6242 (on the left side in all images) and Ti_2AlC (on the right side in all images). Inserts in (b) and (d) shows 5000× of Ti6242 substrate after heatment at 800 and 1000 °C.

Table 3-2 EDS results of spots indicated in Figure 3.3(a)

Spot	Composition (at. %)					
	Ti	Al	C	Zr	Mo	Sn
1	82.17	7.48	-	4.74	4.65	0.97
2	84.45	12.34	-	2.45	0.14	0.62
3	74.57	21.81	-	2.56	-	
4	50.08	47.32	-	2.60	-	
5	48.19	23.64	28.17	-	-	
6	45.43	22.29	32.28	-	-	

3.3.3 Electron backscatter diffraction (EBSD) observations and reaction mechanisms

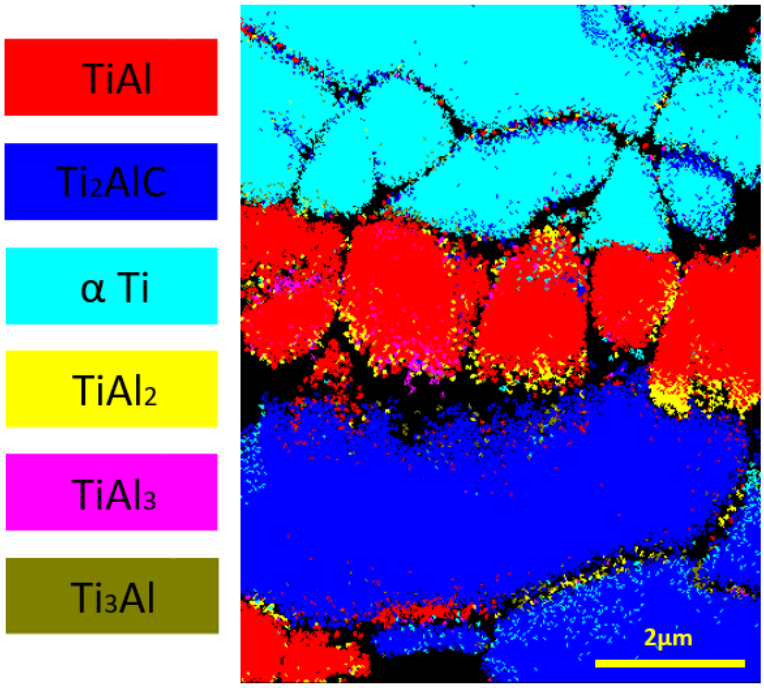

Figure 3.4 EBSD phase map of Ti_2AlC-Ti6242 interface phase map formed during diffusion bonding at 800 °C for 15 min.

To better understand the composition and distribution of phases across the Ti_2AlC-Ti6242 interface, EBSD was used to analyze phases in the reaction layer formed after diffusion bonding Ti6242 to Ti_2AlC at 800 °C for 15 min, **Figure 3.4**. The EBSD results confirm that interfacial reaction layer consists of predominately intermetallic

TiAl, which is in good agreement with EDS results in **Table 3-2**. A small amount of other intermetallic phases, such as $TiAl_2$, $TiAl_3$ and Ti_3Al can be also observed in the reaction layer, especially in the areas closer to Ti_2AlC. In addition, only α-Ti phase can be found in Ti6242 adjacent to the predominantly TiAl reaction layer. Note that the size of that α-Ti phase is much smaller than the gran size of untransformed Ti6242. Hoverer, in some areas such as grain boundaries, regions between Ti_2AlC and Ti6242, and the transformed β-Ti, Kikuchi patterns could not be indexed most likely because of the presence of highly nonstoichiometric phases.

Results presented in in this section suggests that Al diffuses from Ti_2AlC into Ti6242 during diffusion bonding of those two materials, resulting into formation of predominately TiAl rich reaction layer between them. The formation of TiAl and $TiAl_3$ was confirmed previously in the interface during diffusion bonding of pure Ti and Al at 640 °C and 90 min [109]. In addition, Al diffuses even further from the reaction zone into the Ti6242 resulting in the higher Al content in Ti6242 adjacent to the reaction layer (see composition of spot 3 in **Figure 3.3**). The later leads to the transformation of β phase into the α phase, since Al is α stabilizer. The results shown here are in good agreement with previously published results on interfusion between MAX phases and other metallic alloys, which suggests that interfacial reaction always starts with diffusion of weakly bonded A-element from MAX phase into the interface and alloy. For example, de-intercalation of Si in Ti_3SiC_2 and its diffusion in metallic alloys has been observed before in diffusion bonding Ti_3SiC_2 to NiTi of and explained by the fact that the "A" element is the most weakly bonded element in MAX phase [110-112]. Similarly,

diffusion bonding of Cr_2AlC and Ti_2AlC to superalloys reveled formation of complex based intermetallics in the reaction zone at the interface due to Al diffusion form MAX phase to superalloy, and of Al depletion in the MAX phase adjacent to that zone [113].

Area	Hardness value (GPa)	Modulus (GPa)
β	5.59	137.57
α	5.25	137.86
β→ α transformation sublayer	5.62	144.32
TiAl reaction sublayer	6.06	167.88
Ti_2AlC	12.73	206.92

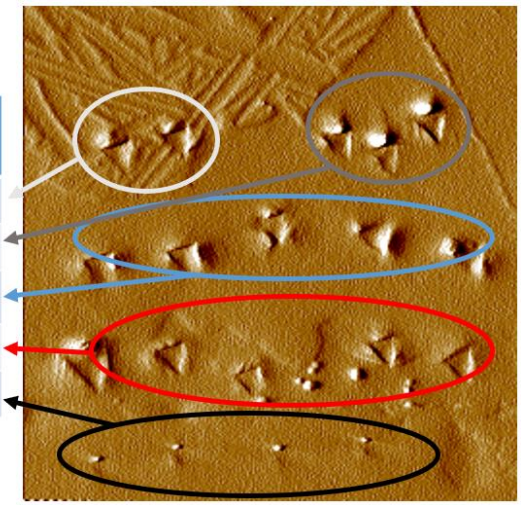

Figure 3.5 Hardness and elastic modulus change across the Ti_2AlC-Ti6242 interface after their diffusion bonding condition at 800 °C, 15 min.

Figure 3.5 summarizes hardness and elastic modulus changes across the Ti_2AlC-Ti6242 interface after diffusion bonding at 800°C for 15 min. obtained using nano-indentation testing. The hardness of Ti_2AlC is more than twice than hardness of other phases in the interface and Ti6242 substrate. However, the change in elastic modulus is not so abrupt across the interface and it decreases gradually from 206.92 GPa for Ti_2AlC, through 167.88 GPa for TiAl in reaction zone and 144.32 GPa for α-Ti phase in transformation zone, to 137.86 GPa for α-Ti and 137.57 GPa for β-Ti constituents in Ti6242. This gradual change in elastic modulus from Ti_2AlC to Ti6242 will most likely prevent easy deboning under applied mechanical loads due to the strain mismatch across the interface.

To further investigate microstructure evolution in the interface during their extended exposure to high temperatures, Ti6242-Ti_2AlC couples diffusion bonded at 800 °C for 15 min. where further exposed to the same temperature for 10 h, 25 h, 50 h, 100 h and 200 h in ambient air. SEM images of those interfaces in **Figure 3.6** clearly show growth of both $TiAl_x$ reaction sublayer and Al rich transformation sublayer at the interface. However, when comparing SEM images in **Figure 3.3** and **Figure 3.6**, the formation to another reaction sublayer (dark gray in **Figure 3.6**) after prolonged exposure of the diffusion couples to the high temperatures is obvious. EDS results (not shown here) confirmed that Ti:Al atomic ratio in this newly formed sublayer is close to 1:2, suggesting that $TiAl_2$ forms as a result of Al diffusion from Ti_2AlC into TiAl reaction sublayer during prolonged exposure of diffusion couples to the high temperatures. Note here that small amount of $TiAl_2$ (and even $TiAl_3$) phase between continuous TiAl reaction layer and Ti_2AlC were identified using EBSD (**Figure 3.4**) even after diffusion bonding of Ti_2AlC to Ti6242, but this phase still did not form continuous layer thick enough to be clearly observed in SEM images shown in **Figure 3.3**. The change in thickness of the all three sublayers, namely TiAl and $TiAl_2$ reaction layers and $\beta \rightarrow \alpha$ transformation zone in Al rich Ti6242 adjacent to the reaction layer is plotted in **Figure 3.7**, and clearly show the continuous growth of all three sublayers with increasing exposure time as Al continues to diffuse from Ti_2AlC into Ti6242.

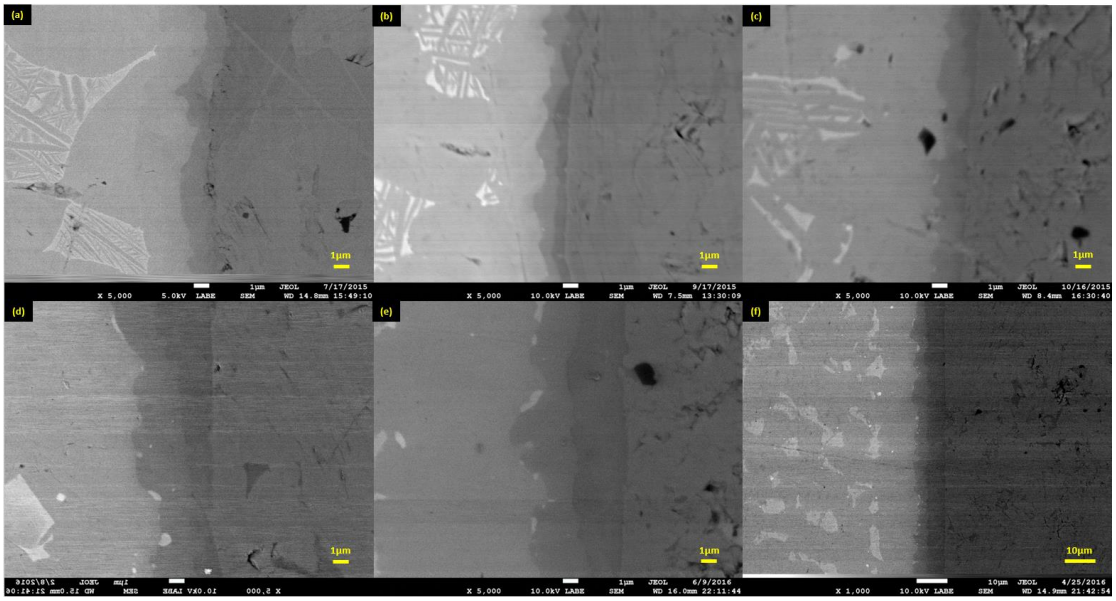

Figure 3.6 Microstructural evolution of the Ti6242-Ti_2AlC interface at 800 °C and for (a) 15 min (b) 10h (c) 25h (d) 50h (e) 100h (f) 200h.

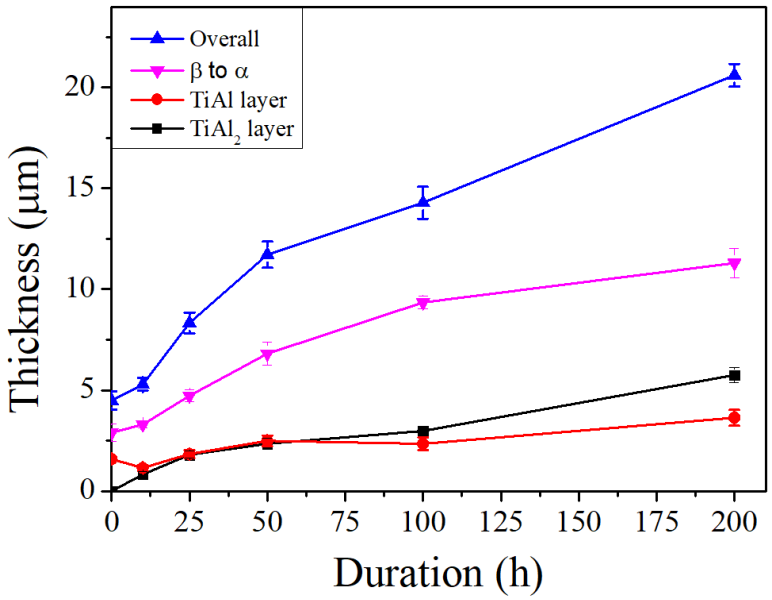

Figure 3.7 Change in thickness of the interfacial reaction transformation layers for the Ti6242-Ti_2AlC interface with different time.

Based on the results shown here, the following reaction mechanism is proposed to take place during:

$$Ti_2AlC \rightarrow xAl + Ti_2Al_{1-x}C \quad (3.1)$$

$$Al + Ti \rightarrow TiAl \quad (3.2)$$

$$Al + TiAl \rightarrow TiAl_2 \quad (3.3)$$

$$TiAl + 2Ti \rightarrow Ti_3Al \quad (3.4)$$

Note here that no significant Al depletion (x in Eq. 3.1) in Ti_2AlC adjacent to the reaction zone can be detected by EDS even after exposure of the couples to 800 °C for 200 h. This once again confirms that Al diffuses very fast in Ti_2AlC to compensate for the Al loss in the zone adjacent to the diffusion interface. More importantly, even after explore of diffusion couple to 800 °C for 200 h, Al depletion from Ti_2AlC is not large enough for its decomposition to Ti_3AlC_2 or TiC, as it was observed to occur due to Al depletion during oxidation of Ti_2AlC [105].

3.3.4 Oxidation of the diffusion bonded Ti_2AlC-Ti6242 couples

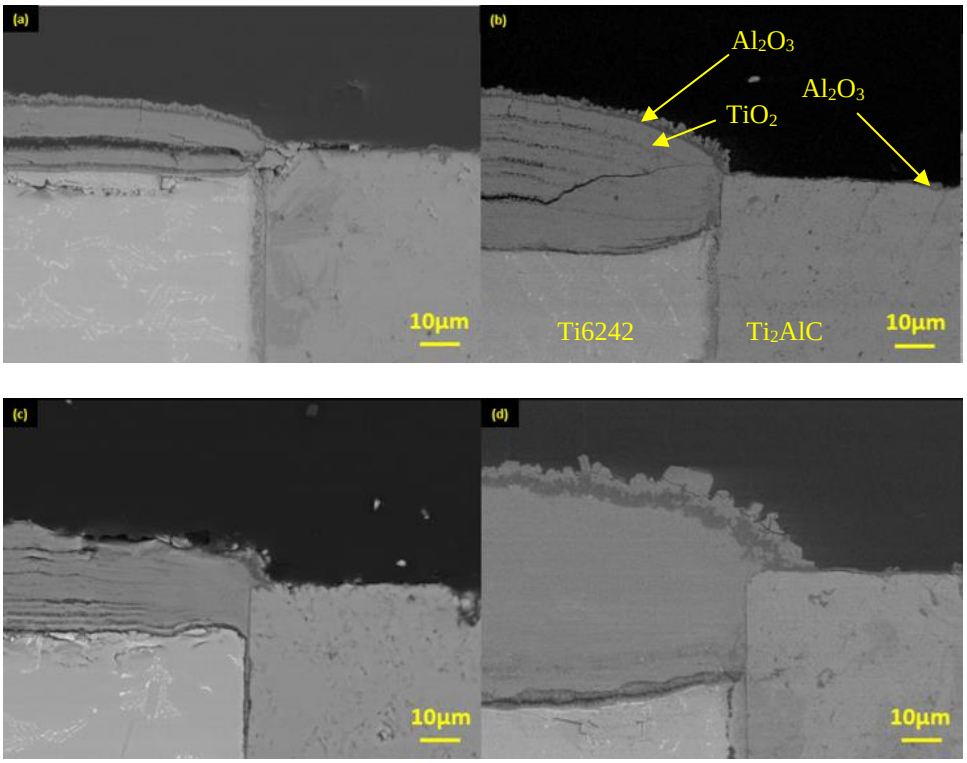

Figure 3.8 Back scattered SEM images of the surfaces of Ti_2AlC-Ti6242 diffuion bonded coupls after heat-treatment in static air at 800 °C for (a) 25 h, (b) 50 h, (c) 100 h and (d) 200 h.

SEM images of the surfaces of Ti6242-Ti_2AlC diffusion bonded couples exposed to the static air at 800 °C for different times are shown in **Figure 3.8**. The medium gray region in the oxide scale formed on Ti6242 was identified as TiO_2 using EDS (results not shown here), while the dark gray region was found to be Al_2O_3. As it can be clearly seen in **Figure 3.8** and **Figure 3.9**, the thickness of the oxide scales on Ti6242 side increases significantly with the exposure time, while Ti_2AlC side is free of any continues oxide scale, with expiation of a few regions where small patches of Al_2O_3. Therefore, formation of the mixed TiO_2+Al_2O_3 on Ti6242 and only predominantly pure Al_2O_3 on

Ti_2AlC is in good agreement with previous oxidation studies reported for both Ti6242 and Ti_2AlC [31, 101, 105]. Note here that even after exposure to 800 °C for only 25 h, oxide scale Ti6242 on contains a lot of cracks, **Figure 3.8**a, that eventually leads to complete spallation of the oxide scale on Ti6242 after prolonged exposure to the ambient air at 800 °C. As a result of oxide scale spallation on Ti6242, the thickness of the oxide scales after 50 h and 75 h of oxidation seems to be the same, as it can be clearly seen in **Figure 3.9**.

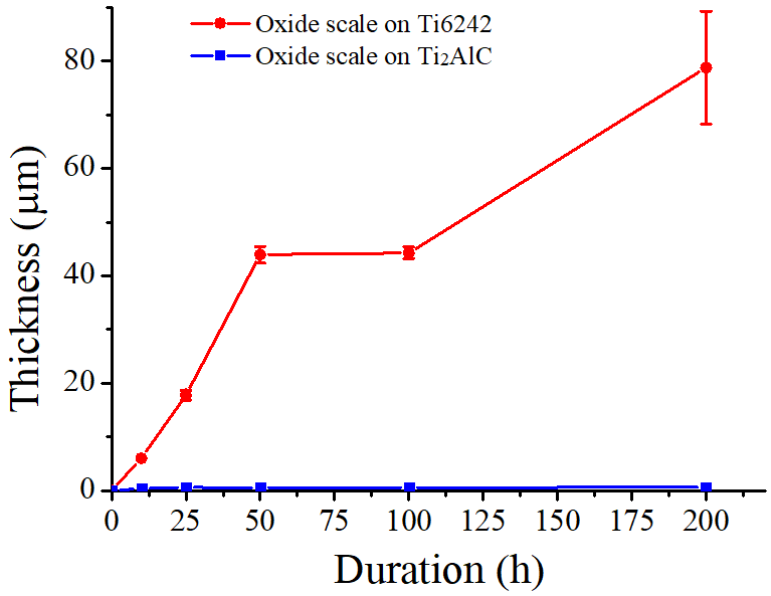

Figure 3.9 Oxide scale thickness of the Ti6242-Ti_2AlC interface exposed to static air at 800 °C for different time.

Results in **Figure 3.8** and **Figure 3.9** clearly demonstrate superb oxidation resistance of Ti_2AlC when compared to Ti6242. Therefore, taking into account a good bonding of Ti_2AlC to Ti6242 (see previous section for mere details), Ti_2AlC can be considered as a good candidate for environmental barrier coating (EBC) for Ti6242, thus

allowing extension of its potential application temperatures to above 500 °C. However, since Al diffuses to both oxide layer on Ti_2AlC to form protective Al_2O_3 oxide scale and into Ti6242 substrate to form reaction sublayers in the interface at the elevated temperature, it is expected that after some time depletion of Al in Ti_2AlC would lead to its decomposition and breakaways oxidation when oxide scale formed on the Ti_2AlC is not anymore pure, protective Al_2O_3, but rather a non-protective mixture of TiO_2 and Al_2O_3. Our previous results showed that when Al depletion in Ti_2AlC exceeds 5at.%, it decomposes to Ti_3AlC_2 and TiC that further oxidize to form non-protective TiO_2+ Al_2O_3 oxide scale [105]. To better understand the effect of Al diffusion to both oxide scale and Ti6242 substrate on the breakaway oxidation, tapered Ti_2AlC was diffusion bonded to the Ti6242 and exposed to 800, 704 and 650 °C for 100 h to determine critical thickness of Ti_2AlC layer below which Al depletion is sufficient to cause formation of non-protective TiO_2+ Al_2O_3 oxide scale.

Figure 3.10 shows Backscatter electron SEM images of cross-section of Ti6242 with tapered Ti_2AlC layer after exposure to ambient air at 800 °C for 100 h, where the thickness of Ti_2AlC layer increases from top right image to the bottom left image. The bright gray layer on the bottom of all images is Ti6242, the medium dark layer above it is Ti_2AlC, and the dark gray layer on the top of Ti_2AlC is an oxide scale. Several different regions with different phase compositions can be observed along oxidized Ti6242 sample with tapered Ti_2AlC in **Figure 3.10**. In region A, with a very thin Ti_2AlC layer, SEM images and EDS result shows that Ti_2AlC completely oxidized into primarily TiO_x. No Ti_2AlC can be observed between TiO_x and Ti6242 in this region.

With a slightly larger thickness of Ti_2AlC layer in region B, this phase could be detected between primarily TiO_x based oxide scale and Ti6242 substrate in **Figure 3.10**. Note here that when Ti_2AlC layer on Ti6242 is very thin, such as in regions A and B, predominantly TiO_x oxide forms, unlike in the case of oxidation of wage shaped Ti_2AlC where mixed Al_2O_3-TiO_x forms even at the very thin end of the sample. This suggest that not only Al diffuses form Ti_2AlC into both oxide scale and Ti6242 substrate , but also Ti from Ti6242 diffuses towards oxide scale to form primarily TiO_x scale. With the further increase in the initial thickness of the Ti_2AlC layer in region C, formation of predominantly Al_2O_3 oxide scale layer (EDS results for spot 2 in **Figure 3.10**) is observed above the mostly pure TiO_x layer (EDS results for spot 2 in **Figure 3.10**). The morphology of this Al_2O_3 and TiO_x mixed oxide layer is in the good agreement with previous observation on oxidation of Al depleted Ti_2AlC, [39, 105]. Partial spallation of oxide scale can be observed in **Figure 3.10**, especially in regions A, B and C. This spallation of the oxide scale occurred during cooling of the sample and it indicates a limited strength of the interface between mixed oxide and Ti_2AlC. With the further increase of the Ti_2AlC layer in region D, only isolated islands of mixed TiO_x-Al_2O_3 oxide scale can be observed within otherwise very predominantly Al_2O_3 thin oxide scale. Those isolated island of the mixed TiO_x-Al_2O_3 oxide are believed to form in the regions with higher amount of the $TiAl_x$ secondary phase [105]. When the Ti_2AlC layer is thick enough, even the small island of mixed TiO_x-Al_2O_3 disappear as seen in region E in **Figure 3.10**, and only a thin and protective Al_2O_3 layer forms on the surface of the sample.

Table 3-3 Critical thickens of the tapered Ti_2AlC layer in diffusion bonded Ti_2AlC-Ti6242 couples that leads to breakaway oxidation of Ti_2AlC after oxidation at different temperatures for 100h.

Temperature, ^oC)	800	704	650
Critical thickness, µm	250	70	35

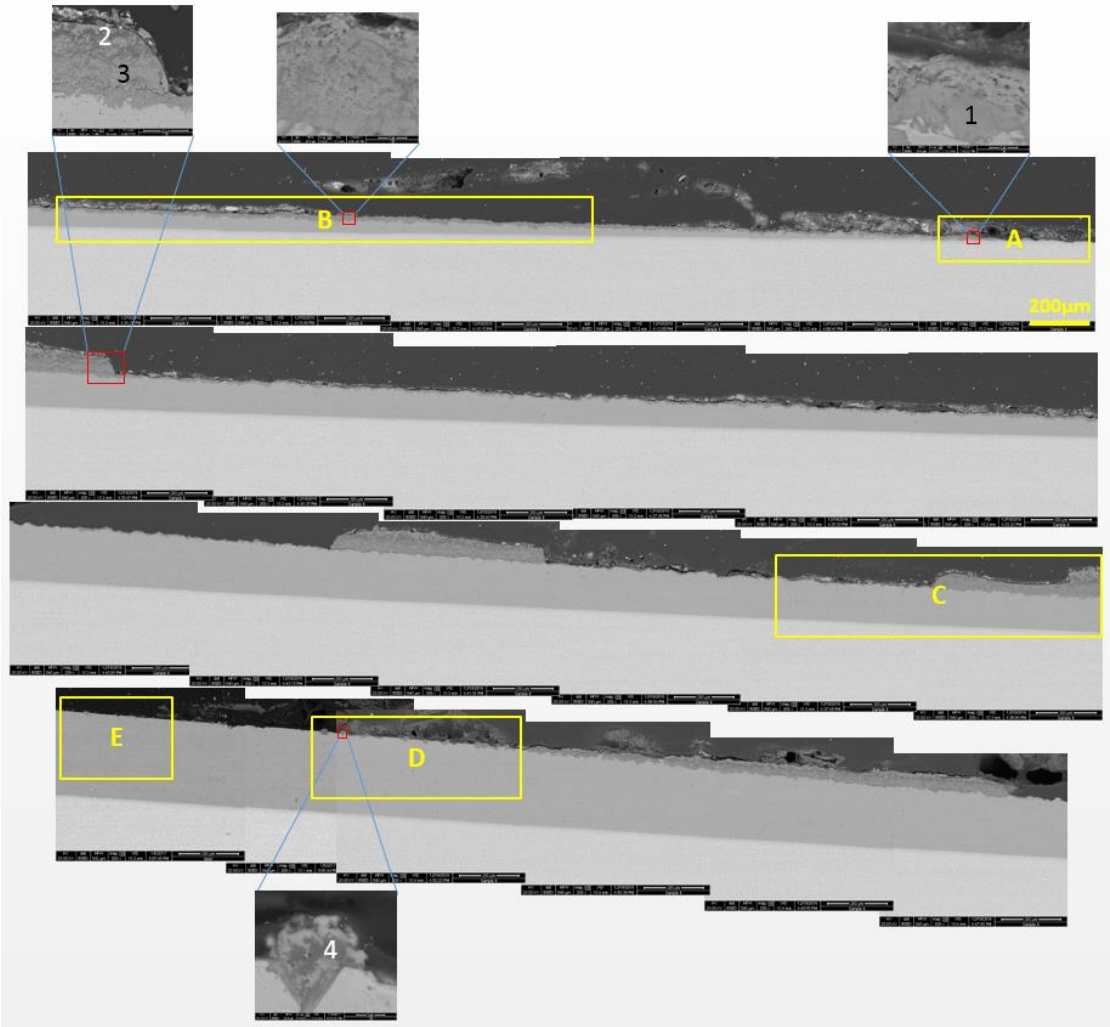

Figure 3.10 Back-scattered electron SEM images of corss-section of Ti6242 with tappered Ti_2AlC layer after exposure to ambient air at 800 °C for 100 h. Inserts show higher maginification images in areas A, B, C, D and E.

Table 3-4 EDS results of spots provided in inserts of Figure 3.10

Spot	Composition (atomic %)		
	Ti	Al	O
1	25.29	2.07	72.64
2	2.84	37.44	59.72
3	31.96	0.93	67.11
4	2.34	31.29	66.37

Based on the results presented in **Figure 3.10**, it is clear that breakaway oxidation of tapered Ti_2AlC and formation of the non-protective mixed TiO_x-Al_2O_3 oxide scales instead of the protective predominantly Al_2O_3 one occurs when the thickness of the tapered Ti_2AlC layer is below some critical value, i.e. at the border between regions C and D. That critical thickens of tapered Ti_2AlC was measured to be of around 250 μm after oxidation at 800 °C for 100 h. As it is shown in **Table 3-3**, the critical thickness of breakaway oxidation of the tapered Ti_2AlC layer diffusion bonded to Ti6242 was found to decrease significantly with decreasing oxidation temperature by analyzing SEM results (not shown here) after oxidation at 800, 704 and 650 °C.

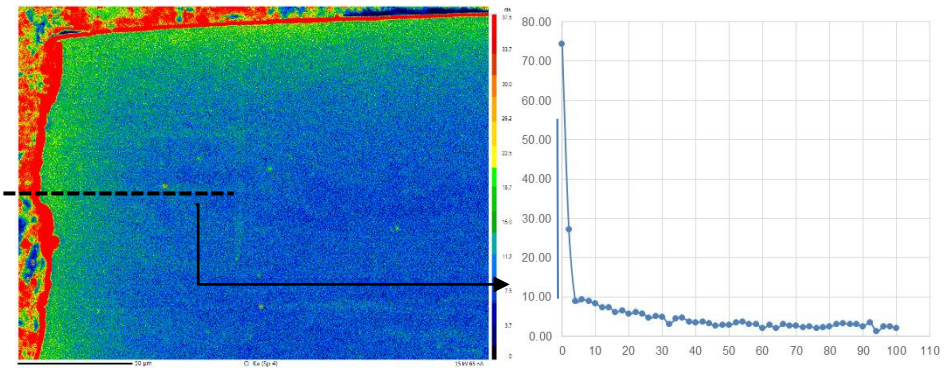

Figure 3.11 EPMA mapping of oxygen Ti6242 after oxidation at 800 °C for 100 h (left) with oxygen concentration profile along dashed line (right).

Last but not least, EMPA quantitative analysis was carried out to detect eventual presence of oxygen in the oxidized Ti6242 diffusion bonded to tapered Ti_2AlC, since small amount of oxygen in Ti6242 causes its significant embrittlement. **Figure 3.11** clearly shows that oxygen can be detected not only in the ~5 µm thick TiO_2 that forms on the surface of bare Ti6242 when it is exposed to the oxidation at 800 °C, but also ~100 µm beyond the oxide scale into the Ti6242. However, **Figure 3.12** shows no presence of oxygen in the Ti6242 sample diffusion bonded to tapered Ti_2AlC, after its oxidation at 800 °C for 100 h, even in the region where non-protective mixed $TiO_x+Al_2O_3$ oxide scale forms (region C in **Figure 3.10**). Not also in **Figure 3.12,** that Ti:Al atomic ratio remains very close to 2:1 in Ti_2AlC even after its long term oxidation and Al diffusion from Ti_2AlC to both Ti6242 substrate and mixed $TiO_x+Al_2O_3$ oxide. Further EMPA analysis of the composition of tapered Ti_2AlC diffusion boded to Ti6242 and oxidized at 800 °C for 100 h, in different regions showed no presence of any oxygen in the Ti_2AlC layer, **Table 3-5**. Therefore, EMPA results clearly show that Ti_2AlC can be successfully used not only to protect Ti6242 from the rapid oxidation, but also to prevent oxygen diffusion in the surface of Ti6242, and consequently its surface embrittlement.

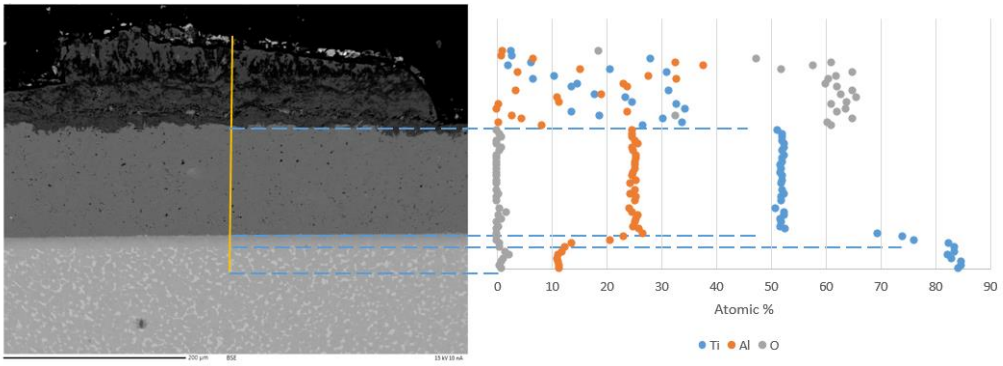

Figure 3.12 Back-scattered eelctron SEM images and EMPA results of Ti6242 diffsuion bonded to tapered Ti_2AlC layer after oxidation on air at 800 °C for 100 h.

Table 3-5 Elemental composition of Ti_2AlC determined using EMPA in regions B, C and E in Figure 3.10. Carbon content was not reported because it cannot be quantified accurately using EMPA, and is assumed to be reminder to 100 at.%.

Region in Figure 3.10	B	C	E
Ti, at.%	52.49±0.93	52.18±0.11	52.07±0.32
Al, at.%	24.87±1.09	24.87±0.37	25.19±0.27
O, at.%	1.12±0.90	0.00±0.00	0.21±0.10

3.4 Summary

Ti6242 and Ti_2AlC were successfully diffusion bonded by PECS at 800°C and 1000 using PECS under the processing condition of 800 °C, 5 MPa, C for 15 min. However, since diffusion bonding at 1000 °C results in transformation of β phase into the α phase in Ti6242 substrate, only Ti6242-Ti_2AlC couples diffusion bonded at 800 °C where further selected to study the oxidation resistance and phase evolution in the Ti_2AlC-Ti6242 interface after extended exposure to temperatures up to 800 °C in ambient air.

Results of this study clearly show that after extended exposure of Ti_2AlC-Ti6242 to the ambient air, Al diffuses from Ti_2AlC into both Ti6242 substrate and oxide layer

that forms on Ti_2AlC. Diffusion of the Al from Ti_2AlC into Ti6242 results in formation of two reaction sublayers at Ti_2AlC into Ti_2AlC-Ti6242 interface, the first one adjacent to Ti_2AlC costing mostly of $TiAl_2$ while the second one closer to Ti6242 consisting mostly of TiAl. In addition, further diffusion of Al from Ti_2AlC to Ti6242 substrate results in the formation of transformation zone, in which β phase Ti6242 completely transforms into the α phase. Thicknesses of both $TiAl_2$ and TiAl reaction sublayers and β→α transformation zone in Ti6242 increase with increasing exposure time to high temperatures, but they thicknesses do not exceeded ~5 μm, ~3 μm and ~12 μm, respectively, after exposure of Ti_2AlC-Ti6242 couple to 800 °C for 100 h.

In addition, fast diffusion of Al from Ti_2AlC layer in Ti_2AlC-Ti6242, and its preferential oxidation, results in the formation of the protective Al_2O_3 oxide scale if thickness of Ti_2AlC is above some critical value. Oxidation studies using Ti6242 samples diffusion boded to tapered Ti_2AlC clearly show that as Al diffuses form Ti_2AlC into both Ti6242 and oxide scale, Al depleted Ti_2AlC layer with thickens below the critical value does not oxidize any more to form protective Al_2O_3 scale, but rather a non-protective oxide scale costing of TiO_2+Al_2O_2 mixture. This critical thickens of the Ti_2AlC layer at which oxidation breakaway occurs was found to be a strong function of oxidation temperature. More importantly, no oxygen was detected in Ti642 substrate after long term exposure of Ti_2AlC-Ti6242 couples to elevated temperatures and ambient air. The latter is particularly important, since oxygen diffusion into Ti6242 beyond TiO_2 that forms on its surface during oxidation, results in it significant embrittlement.

Results obtained in this study clearly suggest that Ti_2AlC can be used successfully as an environmental barrier coating on Ti6242 to protect it if from the rapid oxidation and oxygen embrittlement at elevated temperatures, thus extending its potential application up to ~800 °C. However, the thickness of the protective Ti_2AlC has to be carefully designed for different temperatures and exposure times to avoid significant Al depletion in Ti_2AlC, and consequently its breakaway oxidation, due to continuous diffusion of Al from Ti_2AlC into both protective Al_2O_3 scale and Ti6242 substrate.

4. EEEECT OF IMPURITIES ON THE MORPHOLOGY AND SPALLATION OF THE OXIDE FORMED BY OXIDATION OF CR_2ALC

4.1 Literature Review

Mn+1AXn (MAX) phases are a group of ternary transition metal carbides where M is early transition metal element, A is group 13-16 element and X is C and/or N [2, 3]. They have been investigated extensively because of their unique mechanical properties, especially at high temperatures, such as high strength, nonlinear elastic behavior, excellent thermal shock resistance, damage tolerance, and good creep resistance [4, 7, 104]. Moreover, some of them having Al as and A element, show good oxidation resistance since they can form a dense and protective oxide scale when exposed to oxidizing environments at elevated temperatures [31]. Ti_2AlC is one of the Al containing MAX phases that exhibit excellent oxidation resistance. Its low density, good machinability and excellent thermal expansion match with alumina scale makes it attractive for high-temperature applications [48]. Although initial short-term studies reported by Wang and Zhou in 2003 [39] suggested that oxidation kinetics of Ti_2AlC flows parabolic low, later studies by Sundberg [44]. Again in 2007 and Byeon et al. [40] reported cubic oxidation kinetics for Ti_2AlC in oxidation tests in 1000 - 1400 °C temperature range. Later long –term oxidation studies also cubic oxidation kinetics in both air [46, 92] and steam [48].

Cr_2AlC is another Al containing MAX phases that exhibit good oxidation resistance. Cr_2AlC is particular attractive as a potential bond coat between superalloys and zirconia based thermal barrier coatings [113, 114]. However, unlike Ti_2AlC that

forms almost pure Al_2O_3 oxide scale after short transit regime in which mixed TiO_2+ Al_2O_3 oxide scale form, oxidation of Cr_2AlC results not only in formation of Al_2O_3 protective scale, but also a Cr_7C_3 sub-layer in Al depleted zone between the Al_2O_3 layer and the Cr_2AlC substrate [56]. Nevertheless, similar as in the case of Ti_2AlC, oxidation kinetics of Cr_2AlC was initially reported to be parabolic [115], while later studies long-term studies confirmed cubic oxidation kinetics [116, 117].

Like in the case of Ti_2AlC, the cyclic oxidation resistance of Cr_2AlC is excellent at 1000 and 1100 °C, but unlike in the case of Ti_2AlC, it becomes much worse at 1200 and 1300 °C because the oxide scale spallation [118], most likely due to the large difference in coefficient of thermal expansion of Cr_2AlC and Al_2O_3. However, most recently, Smialek [119] reported that spallation of oxide scale formed on Cr_2AlC is quite different for samples with different amount of Cr_7C_3 impurities in the staring material, and proposed that formation of larger amount of Cr_2O_3 in otherwise primarily Al_2O_3 oxide scales in samples with higher Cr_7C_3 is detrimental for spallation resistance of oxide scale.

The purpose of this work is to investigate the effect of impurities on the morphology and spallation of oxide scale formed on Cr_2AlC, following initial studies reported Smialek [119]. Bulk Cr_2AlC polycrystalline samples were prepared using different starting materials with different amount of trace impurities such as Fe and S, and with different amount of Cr_7C_3 secondary phase, and their oxidation was studied at 1200 °C. In addition, oxidation of high-purity Cr_2AlC single crystalline and wedge-shaped polycrystalline Cr_2AlC samples were carried out at 1200 °C to better understand

underlying oxidation mechanism and spallation resistance of the oxide sale formed on Cr_2AlC.

4.2 Experimental Methods

Table 4-1 Composition of starting Cr and Al of powder according to the vendor's certificates analysis

Powder	Element	Fe	S	P
I	Cr	1210	164	<10
	Al	1000	N/A	N/A
II	Cr	300	N/A	N/A
	Al	65	<2	<2

Polycrystalline Cr_2AlC samples with different amount of impurities were prepared using Cr_3C_2 powders (Sigma Aldrich, < 44 μm) and two different types of Al powders (Alfa Aesar, Powder I: 99.5%Al, <44 μm; II: 99.97%Al, < 44 μm) and two types of Cr powders (Alfa Aesar, Powder I: 99%Al, <44 μm; Powder I: 99.95%Al, < 74 μm). As it can be seen in **Table 4-1**, both Al and Cr powders labeled as Powder I contain larger amount of Fe and S trace elements. The Cr, Al and Cr_3C_2 powders were mixed in different molar ratios as listed in **Table 4-2**, and ball milled with using zirconia balls for 24 h. The powder mixtures poured in the 20mm diameter graphite die and reaction sintered at 1275 °C and 20 MPa for 30 min in ultra0high purity Ar by Pulsed Electric Current Sintering (PECS, Thermal Technologies, CA), commonly referred as Spark Plasma Sintering (SPS).

Table 4-2 Mixing ratios of the starting powders for different Cr_2AlC samples with amount of Cr_7C_3 determined from SEM images

Samples	Mixing ratio of elemental powders, mol%	Cr_7C_3 impurity, %
I-PP	Cr(powder I):Al(powder I):Cr_3C_2=1:2.5:1	0%
I-LC	Cr(powder I):Al(powder I):Cr_3C_2=1:2.3:1	1.85%
I-HC	Cr(powder I):Al(powder I): Cr_3C_2=1:2:1	8.8%
II-PP	Cr(powder II):Al(powder II): Cr_3C_2=1:2.5:1	0%
II-HC	Cr(powder II):Al(powder II): Cr_3C_2=1:2:1	12.4%

Cr_2AlC single crystals were grown from a liquid solution with composition of Cr = 0.36, Al = 0.57 and C = 0.07 [120]. After holding at T_{max} = 1650°C for two hours to ensure carbon dissolution, crystal growth was achieved by slowly cooling down the solution from T_{max} to T = 1200°C for 5 to 7 days with an Ar pressure p_{Ar} = 1.5bar. Slow cooling aims at limiting unwanted spontaneous nucleation by putting to good use Ostwald ripening. Even though, the solidified flux usually contains more than 10 large size crystals as well as many smaller ones. A large size crystal is defined as the one whose dimensions are mainly limited by the crucible size and solution volume. The areas of the platelets used here were varying from around 8–12 cm^2, with a thickness limited to 1–2 mm. The c-axis is systematically perpendicular to the platelet surface.

Both polycrystalline and single crystal specimens were cut in smaller samples with approximate dimension of 4 mm x 4 mm x 4 mm for isothermal oxidation and all sample surfaces were mechanical polishing to 3 μm diamond paste. In addition, fully dense Cr_2AlC bulk samples made from II powder (I-PP and I-HC samples) were sliced

by wire Electrical Discharge Machining (EDM) into 2 mm thick discs to make wedge-shaped Cr_2AlC samples. The Cr_2AlC discs were then thermally bonded to larger aluminum discs using crystalbond (Ted Pella, CA) on a hot plate (Thermo Scientific), and polished under the angle to form wedge sample with a 3.5±0.2° taper and the thickness ranging from ~10-20 μm at the very tip of the wedge, to 500 μm at the opposite end. The wedge-shaped Cr_2AlC samples were removed from aluminum discs by washing in acetone (Macron Fine Chemicals).

For isothermal oxidation tests, a box furnace (Carbolite, UK) was preheated to a target temperature of 1200 °C and specimens were placed on alumina plates and inserted into the hot furnace to oxidize for different amount of time, from 1 h to 100 h. For cyclic oxidation tests, sample were place on the alumina plates and inserted in box furnace preheated to 1200 °C to oxidize for 5 h before removing from the furnace and to cooling down to ambient temperature in each oxidation cycle. The weight of the sample was measured after each oxidation cycle.

As sintered samples and oxidized samples were characterized using characterized using Quanta 600 FEG (FEI, Oregon, USA) Scanning Electron Microscope (SEM) with energy dispersive X-ray spectroscopy (EDS, Oxford Instruments) and Fera-3 Model GMH Focused Ion Beam Microscope equipped with Electron Back Scatter Diffraction (EBSD, Oxford Instruments) detector.

4.3 Results and Discussion

4.3.1 Chromium-carbide secondary phases in Cr_2AlC

Sintering of the sample using different mixtures of starting powders listed in **Table 4-2,** led to significant different differences in the composition, as seen from SEM images in **Figure 4.1**. The samples prepared with the stoichiometric elemental ratio of Cr:Al:C=2:1:1, namely samples I-HC and II-HC in **Table 4-2**, had a large amount of chromium-carbide (light gray in **Figure 4.1**a and d) as impurities, apart from Cr_2AlC (medium gray in **Figure 4.1**) and smaller amount of Al_2O_3 impurities (dark gray in **Figure 4.1**). Large amount of chromium-carbide into those due to the loss of low melting point Al during sintering due to its volatilization before reacting with other powders to form Cr_2AlC. To compensate the deficiency of Al, 25% of extra Al is added in powder mixture and phase pure Cr_2AlC, namely samples I-PP and II-PP, as shown in **Figure 4.1**c In addition, **Figure 4.1**b shows SEM images of a samples prepared with addition of only 15% of extra Al Powder I, that still contain small amount of chromium-carbide. Note here that all phases in Figure 1 where identified from EDS results (not shown here).

Since EDS cannot provide exact C content, it is impossible to determine the type of chromium carbide that formed during reaction sintering from those results. Therefore, XRD and EBSD of all samples was carried out. XRD results (not show here) indicate that all samples sample contained Cr_2AlC as a major phase and a small amount of Al_2O_3, while samples I-HC, I-LC and II-HC also contained Cr_7C_3 as a secondary phase too. Results of Releveled analysis in **Table 2** show that amount of Cr_7C_3 secondary phases

ranged from 1.85% in I-LC to 12.4% in II-HC samples. EBSD results also confirmed that reaction sintered samples consist of Cr_2AlC as a major phase, Cr_7C_3 as a secondary phase and small amount of Al_2O_3 impurities, as it is illustrated in **Figure 4.2**a for II-HC sample. **Figure 4.2**b also illustrates find-grain structure of the reaction sintered samples, with all grains smaller than ~10 μm.

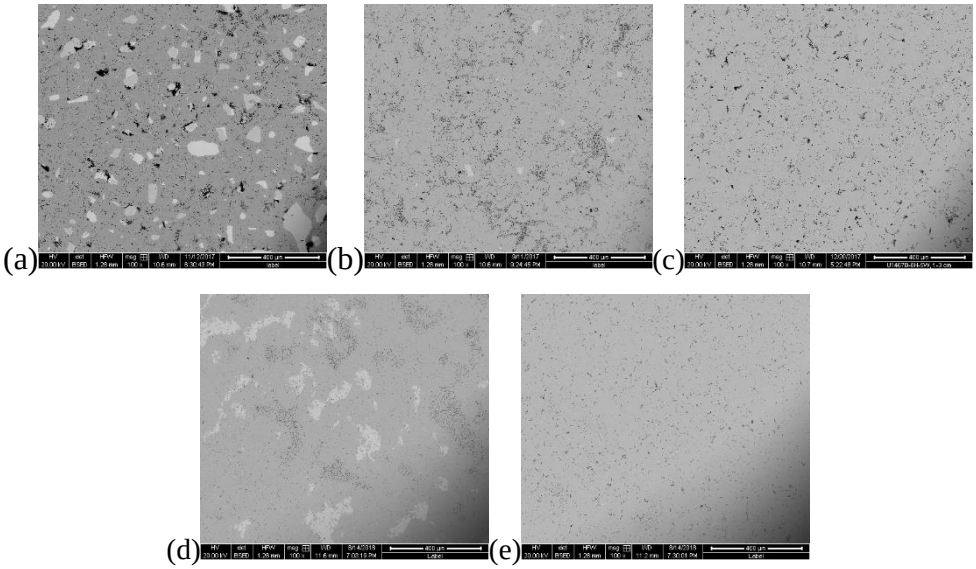

Figure 4.1 BSE images (a) I-HC, (b) I-LC, and (c) I-PP prepared using Al Powder I and Cr Powder I, and (d) II-HC and (e) II- PP prepared using high purity Al Powder II and Cr Powder II.

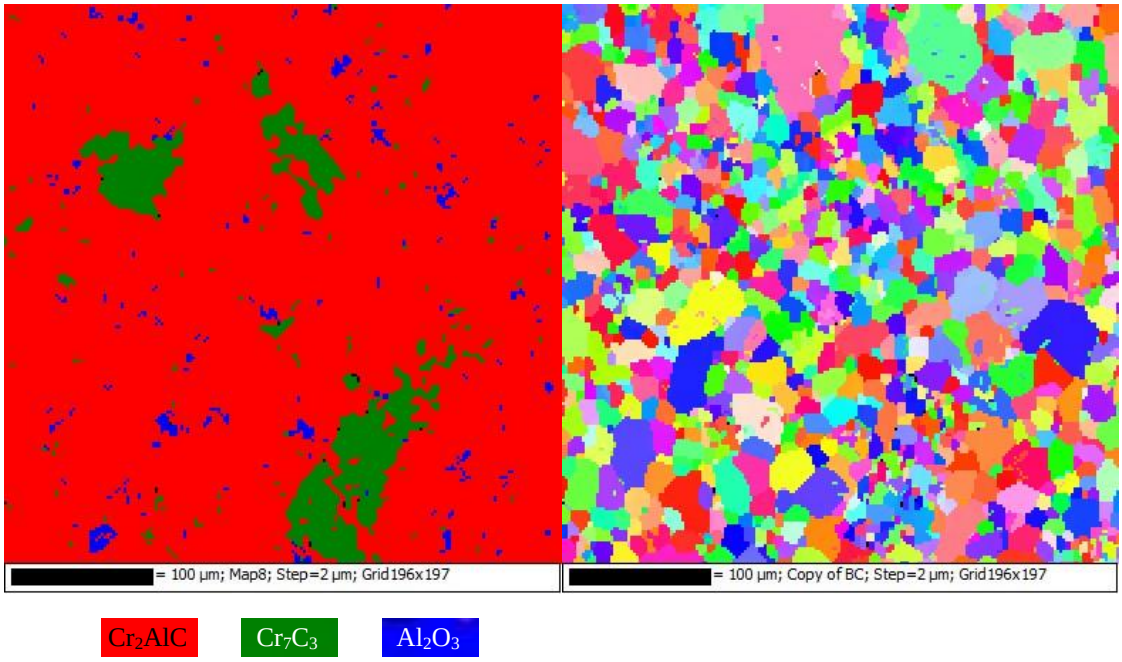

Figure 4.2 EBSD of II-HC samples: (a) phase composition map and (b) Inverse pole figure (IPF) map.

4.3.2 Al_2O_3 morphology of single crystal Cr_2AlC

Figure 4.3 shows SEM images of surfaces and cross sections of single crystal Cr_2AlC after oxidation at 1200 °C for 15, 30 and 60 min. The surfaces parallel and perpendicular to (0001) plane in single crystal Cr_2AlC are shown in **Figure 4.3**a and **Figure 4.3**b, respectively. EDS results showed that surface parallel to (0001) plane contained both Al_2O_3 (dark gray in **Figure 4.3**a) and Cr_2O_3 (light gray in **Figure 4.3**a), while on the surface perpendicular (0001) plane contained only only Al_2O_3. Most importantly, SEM images of the cross sections through the oxide scale grown on the surface perpendicular to the (0001) plane, show that even after oxidation of only 15 minutes, a sublayer of Cr_7C_3 forms in Al-depleted zone beneath the Al_2O_3. The later

suggests that, contrary to the common believe, diffusion of Al along A-layer is not fast enough to compensate for Al deficiency in Cr_2AlC beneath Al_2O_3 scale. EBSD results in **Figure 4.4** shows that single phase, compact and polycrystalline layer of Cr_7C_3 forms in Al-depleted zone beneath Al_2O_3 oxide scale. Therefore, farther growth of the Al_2O_3 oxide scale on surfaces perpendicular to (0001) with the oxidation time (d) is possible most likely due to outwards diffusion of Al through grain boundaries Cr_7C_3 layer. SEM images of the cross sections through oxide scale formed at surfaces parallel to (0001) plane in **Figure 4.3**c, a layer of Cr_7C_3 can be also observed beneath oxide scale that consist of Al_2O_3 and Cr_2O_3. However, in this case Cr_7C_3 in not phase pure but also contains Al_2O_3 and Cr_2O_3 suggesting that internal oxidation takes place on those surfaces, most likely die to faster inward diffusion of oxygen through the mixed oxide scale.

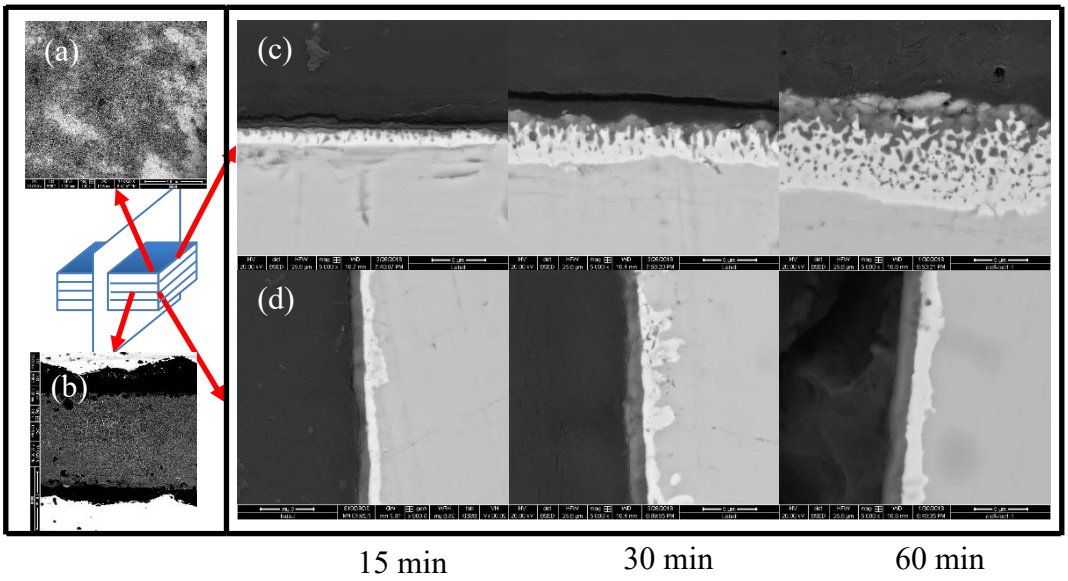

Figure 4.3 SEM of single crystal Cr_2AlC oxidized at 1200 °C: (a) surface parallel to (0001) plane, (b) surface perpendicular to (0001) plane surface; (c) cross section through the oxide scale formed on the surface parallel to (0001) plane after oxidation for 15, 30, and 60 minutes; (d) cross section through the oxide scale formed on the surface perpendicular to (0001) plane after oxidation for 15, 30, and 60 minutes.

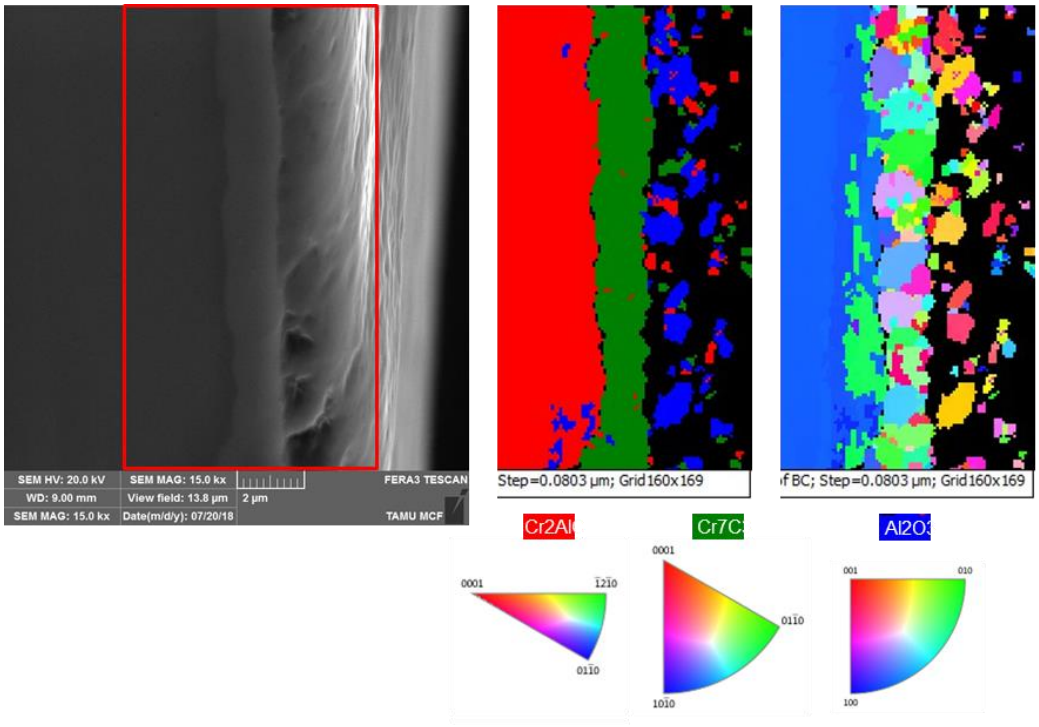

Figure 4.4 EBSD results for single crystal Cr_2AlC oxidized at 1200 °C for 15 minutes with phase composition maps and IPF maps.

4.3.3 Al_2O_3 morphology from polycrystalline Cr_2AlC

The SEM images of cross sections through the oxide scales formed after oxidation of polycrystalline Cr_2AlC prepared with different elemental powder rations, using low purity (Powders I) and high purity (Powders II) powders are shown in **Figure 4.5** and **Figure 4.6**, respectively. **Figure 4.5** and **Figure 4.6** shows significant differences in the morphology of the oxides scale, oxide scale adhesion and composition of the depleted zone beneath oxides scales for sample prepared using different powder ratios and powders with different ammonites of trace elements (Fe and S) impurities.

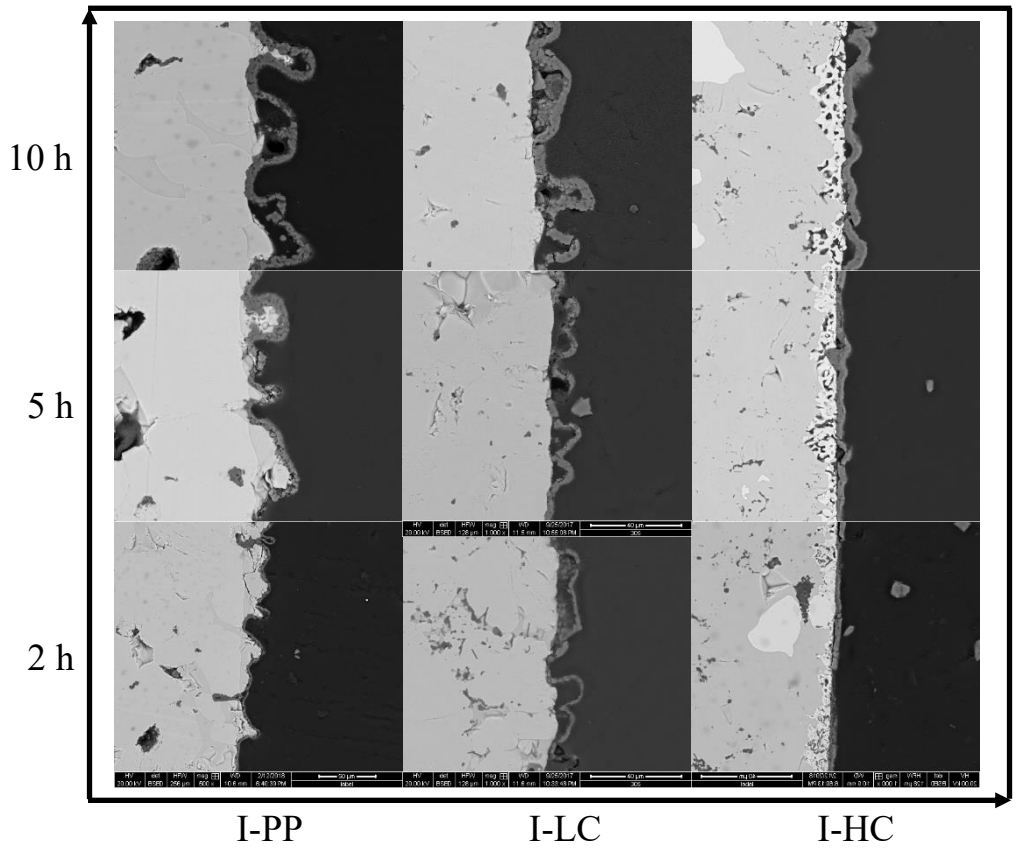

Figure 4.5 Cross-sectional SEM images of Cr2AlC prepared using low purity powder (Powder I) after oxidation at 1200 °C for different time.

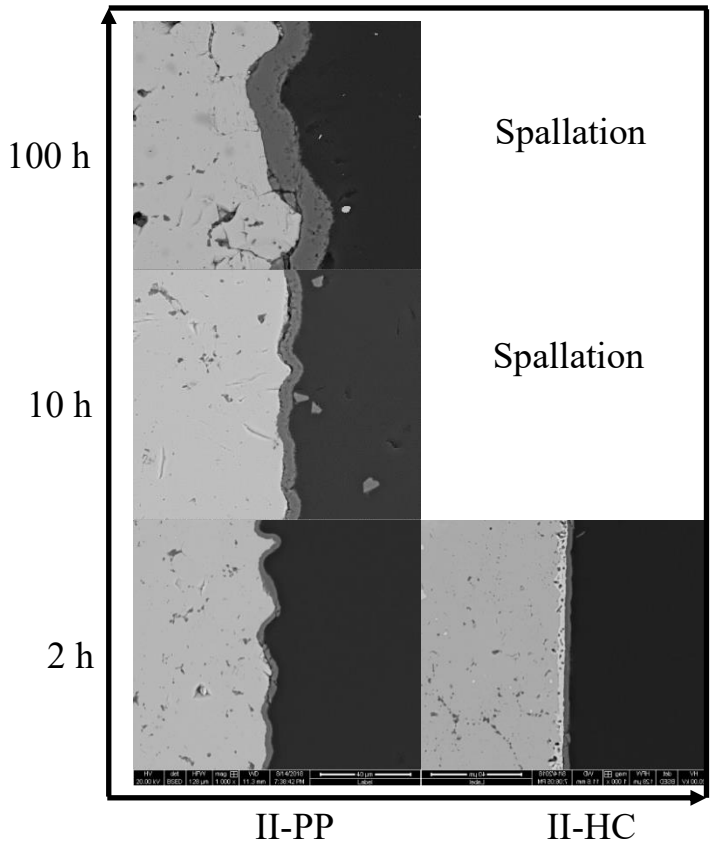

Figure 4.6 Cross-sectional SEM images of Cr2AlC prepared using high purity powders (Powder II) after oxidation at 1200 °C.

First, it is clear from **Figure 4.5** and **Figure 4.6** that Cr_7C_3 (light gray layer in **Figure 4.5** and **Figure 4.6**) forms in the Al-depleted zone beneath Al_2O_3 scale only in the sample with higher content of Cr_7C_3 secondary phase (i.e. samples I-HC and II-HC), as expected according to the all previously published results on oxidation of Cr_2AlC [56, 115-118, 121, 122]. However, phase pure Cr_2AlC samples in this study (i.e. samples I-PP and II-PP) show formation of only Al_2O_3 oxide scale even after isothermal oxidation for 100 h at 1200 °C. Those results are not only in contradiction with previously published results on oxidation of polycrystalline Cr_2AlC, but also with our results on

oxidation of single crystals **Figure 4.3** and **Figure 4.4** that clearly show transformation of Cr_2AlC into the Cr_7C_3 in the Al-depleted zone bellow Al_2O_3 scale after very short oxidation even on surface perpendicular to the (0001) plane.

I order to explain this observation, we hypothesis that phase pure Cr_2AlC must contain a small amount of excess Al, most likely in the form Al reach Cr-Al solid solution or intermetallic that are undetectable by XRD, SEM and EBSD. To test this hypothesis, quantitative point and area EDS analysis of as-sintered samples was carried out, and selected but typical results are summarized in **Figure 4.7** for I-HC and I-PP samples. As it can be seen in **Figure 4.7**, Cr:Al elemental ratios determined from both point and areal analysis are very similar in samples whit higher content of Cr_7C_3 (sample I-HC), and show slightly lower Al content than that expected for pure Cr_2AlC due to the presence of Cr reach secondary phase. However, for phase pure samples (sample I-PP) Cr:Al ratio from point analysis in individual Cr_2AlC grains is close to 2:1 as expected for Cr_2AlC, while areal results show around 4% higher Al content. The later indicate presence of small amount of Al or Al-rich phases in the grain boundaries, from which Al can diffuse outwards through grain boundaries to form protective Al_2O_3 oxide scale.

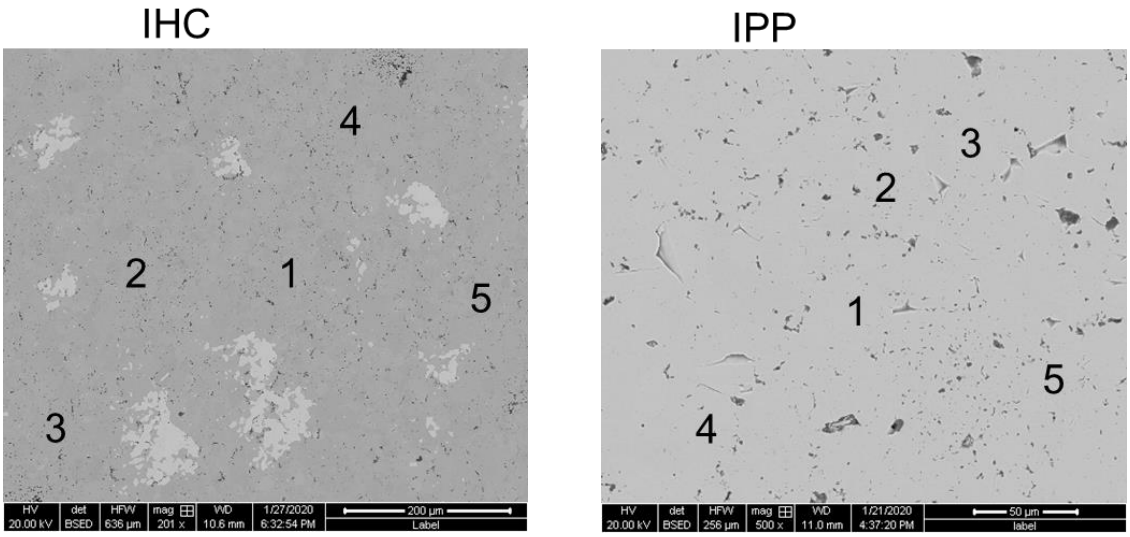

#	Cr	Al	Cr:Al	
1	39.12	18.37	2.130	2:0.94
2	39.13	17.85	2.192	2:092
3	41.13	18.75	2.194	2:0.92
4	39.36	17.79	2.212	2:0.90
5	41.79	19.44	2.150	2:0.93

Point EDS

#	Cr	Al	Cr:Al	
1	41.11	20.48	2.007	2:0.99
2	41.88	20.86	2.008	2:0.99
3	42.19	20.97	2.012	2:0.99
4	41.19	20.62	1.998	2:1.001
5	40.57	20.19	2.009	2:0.99

#	Cr	Al	Cr:Al	
A	42.35	20.20	2.097	2:0.95
B	42.73	20.31	2.104	2:0.95
C	43.29	20.54	2.108	2:0.94

Area EDS

#	Cr	Al	Cr:Al	
A	40.67	21.15	1.923	2:1.04
B	40.53	21.01	1.929	2:1.04
C	41.30	22.06	1.872	2:1.07

Figure 4.7 Point and areal quantitative EDS analysis of I-HC and I-PP samples.

If the outward diffusion of access Al through grain boundaries is the reason for formation of protective Al_2O_3 scale without transformation of Cr_2AlC in Al depleted zone in Cr_7C_3 in I-PP and II-PP samples, it is reasonable to expect that once all Al from grain boundary is depleted, further oxidation will results in the formation of Cr_7C_3 in the Al-depleted zone beneath Al_2O_3 scale. To test this hypothesis, we prepared wage-shaped from II-PP using procedure described in more details in Chapter 2 and of this thesis in [123], and exposed to oxidation at 1200 °C for 1 h. Cross-sectional SEM images of that

wedge-shape samples in **Figure 4.8**, clearly show that at the very tip of wedge-shaped sample, all Cr_2AlC is completely depleted in Al beneath predominately Al_2O_3 oxides scale and transformed to Cr_7C_3. More importantly, at the thickest end of the wedge-shaped samples, only alumina scale forms on the oxidized surface because the sample is thick enough in that location to supply enough Al through outward grain boundary diffusion to form almost pure Al_2O_3 oxide scale. However, moving from the thicker end of the wedge-shaped sample towards the tip, it can be observed that at certain point (i.e. at the certain thickness of the sample), Al depleted Cr_2AlC beneath Al_2O_3 scale starts to transforms to Cr_7C_3. The later happens when all access Al from grain boundaries is depleted completely and further growth of the oxide layer is possible only by outward diffusion of Al from Cr_2AlC grains beneath oxide scale.

Figure 4.5 and **Figure 4.6** also show that the morphologies of oxide scale formed on different samples are quite different since oxides scale can be planar, convoluted or wrinkled, as it is described in **Figure 4.9**. While I-PP and I-LC have wrinkled morphology at all times and I-HC is planar but becomes also wrinkled after oxidation for more than 2 hours, II-PP forms convoluted oxide scale and II-HC forms planar oxide scale at 2 h that completely spalls off after longer oxidation. Note here that although II-PP does not show significant spallation immediately after oxidation for 100 h, some area of the Al_2O_3 layer is found chipped on the other day after cooling down.

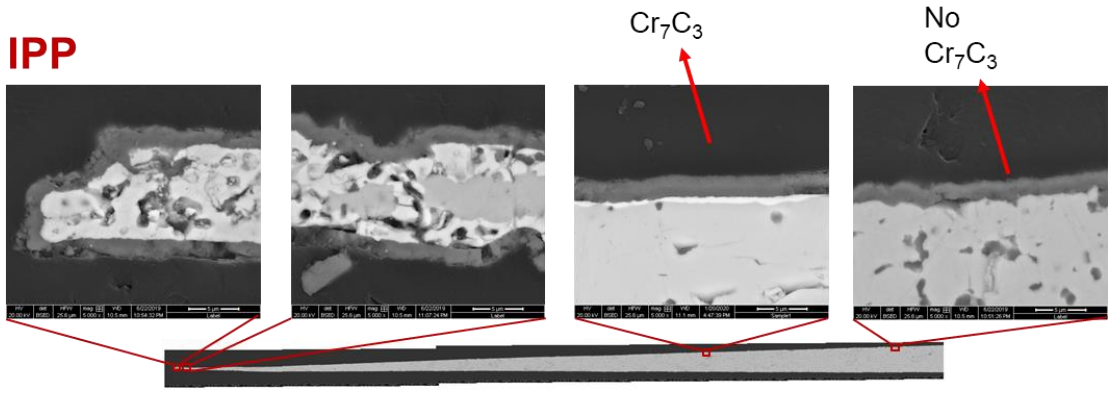

Figure 4.8 Wedge-shaped II-PP Cr_2AlC oxidized at 1200 °C for 60 min.

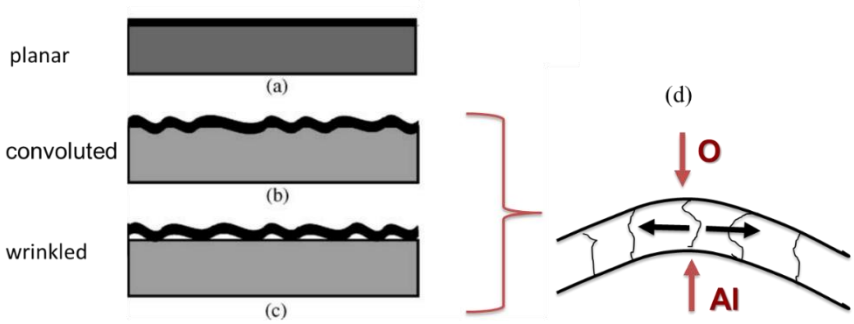

Figure 4.9 Schematics showing (a) planar, (b) convoluted and (c) wrinkled oxide scale morphologies [124]. (d) Schematic illustrating lateral growth of oxide scale in grain boundaries by inward diffusion of O and outward diffusion of Al [125].

4.4 Discussion

First, formation of wrinkled and convoluted oxide scale at the extent observed in this study cannot be explained solely by the larger contraction of the Cr_2AlC with coefficient of thermal expansion of around $13x10^{-6}$ 1/°C [126] during cooling, when compared to the contraction of the alumina oxide scale with coefficient of thermal expansion of around $7\text{-}9x10^{-6}$ 1/°C [127]. Therefore, results of this study suggest that wrinkling and convolution of the oxide scale observed primarily in phase pure (I-PP and

II-PP) samples, and only in I-HC after extended oxidation, is most likely results of the difference in mechanism of the oxide scale growth, stress distribution in the oxide scale, and interfacial strength between oxide scale and substrate.

Wrinkling and convolution of oxide scale has been observed in other alumina forming alloys, such as In FeCrAl alloy [128-134]. In this study, the Al_2O_3 layer formed from Cr_2AlC synthesized with Powder I containing larger amount of Fe and S as impurities exhibits more wrinkling and convolution than (**Figure 4.5** and **Figure 4.6**) than those prepared using high purity Powder II. As it is observed for some other alumina formers, the presence of impurities, such as Fe seems to play a role in promoting lateral growth of Al_2O_3 scale in grain boundaries as it is illustrated in **Figure 4.9**d, leading to the convolution and wrinkling of the oxide scale [125]. The increase of Al_2O_3 creep rates in the presence of Fe impurity [135-137] indicates that Al transport at grain boundaries is faster with the presence of Fe in the scale [138], leading to the fast lateral growth of Al_2O_3 scale. Therefore, more intensive wrinkling and convolution of samples prepared with Powder I can be partially explained by more intensive lateral growth of alumna scale in those samples. With a formed layer of Cr_7C_3 in I-HC Cr_2AlC, only planar Al_2O_3 layer is formed in 2 h, mostly likely due to a low diffusivity of Fe in Cr_7C_3. With longer time, the planar Al_2O_3 layer of I-HC turns to wrinkled because as more Fe diffuses to the surface and segregates on grain boundaries.

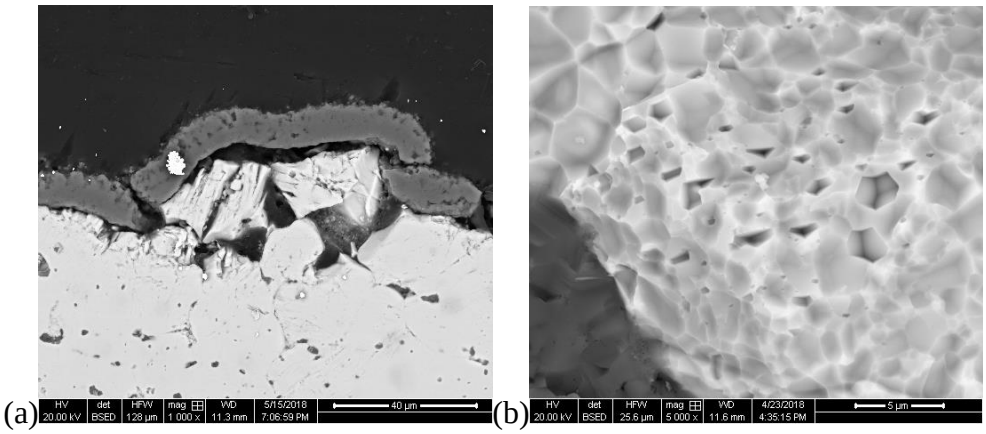

Figure 4.10 SEM images of II-PP oxidized for 100 h on the selected chipped area (a) cross section, (b) surface.

In addition, samples prepared with Powder I show stronger tendency for formation of convoluted oxide scale than samples prepared using high purity Powder II most likely due to the weaker adhesion of the oxide scale to the substrate. This been shown before for some other alumina formers, such as NiAl-based alloys, that small amount of S impurities, as in the case of Powder I leads to the weak adhesion of oxides scale to the substrate and subsequent wrinkling of the initially convoluted oxide scale and eventually its partial spallation [139, 140]. In the case of samples prepared with high purity Powders II, the interface between oxides scale and substrate is extremely storing, as it can be seen in **Figure 4.10**, and leads to the cracking and grain pull in the Cr_2AlC substrate beneath convoluted oxides scale. The cross section and surface images of the chipped Al_2O_3 in **Figure 4.10** indicate a strong adhesion between Al_2O_3 and Cr_2AlC since the compressive growth stress is reported to be as high as about 1 GPa in the convoluted alumna scales [141, 142], and yet it does not lead to a scale delamination but instead pulls off a whole Cr_2AlC grain in the substrate beneath the oxide scale.

Last but not least, presence or lack of the porous Cr_7C_3 beneath the oxide scale also mast important role on the morphology and spallation resistance of the oxide scale. Note here that oxidation of Cr_2AlC samples without Al (I-HC and II-HC) results in formation of porous Cr_7C_3 in Al depleted zone beneath the oxide scale, and in general tends to form more planar oxide scale, **Figure 4.5** and **Figure 4.6**. The later is most likely due to the stronger adhesion of the oxide scale to the substrate in the cases when Cr_7C_3 is present, and the certain extend slower lateral growth in Al_2O_2 layer. The later leads to the massive spallation in the case of II-HC samples, when oxide scale strongly adheres to the substrate, and stresses that build up in the oxide scale due to the lateral growth cannot be relaxed by convolution and wrinkling, and possible creep of the oxide scale.

4.5 Summary

Results of this study shows that pure Cr_2AlC can forms a pure and dense Al_2O_3 layer, like other alumina forming MAX phases during oxidation at high temperatures, only when access Al is present in grain boundaries, most likely in the form of aluminum rich Cr-Al solid solutions or intermetallic. With the presence of Cr_7C_3 secondary phase, the Cr_2AlC is deficient of excess Al and it form Cr_7C_3 sublayer in Al deficient Cr_2AlC beneath the Al_2O_3 layer.

It has been also shown that the he morphology and spallation resistance of the Al_2O_3 layer is significantly influenced by impurities such as Fe and S, and most likely luck of excess Al. Oxide layers on the samples with different amount of impurities results in the formation of planar, convoluted or wrinkled oxide scale. The morphology

of the oxide scale is determined by the rate of the lateral growth of the oxide scale that can be fostered by presence of impurities such as Fe, and adhesion of the oxide scale to the substrate. The latter in turn depends on the tendency for segregation of impurities (such as S) in the interface between oxide scale and substrate, and presence or lack off Cr_7C_3 subscale that forms in Al-depilated zone beneath the oxide scale. Results in this study show that the addition of excess Al and use of starting powders with no impurities such as Fe and S, can foster formation of protective and more spallation resistant Al_2O_3 oxide scale during oxidation of Cr_2AlC. However, both factors contribute to formation of convoluted and wrinkled oxide scale, rather than planar one.

5. OXIDATION RESISTANCE AND COMPRESSIVE DEFORMATION OF MOALB UP TO 1200 °C*

5.1 Literature Review

First characterized in the 1950s by Jeitschko [21], MoAlB crystallizes in the orthorhombic space group Cmcm with a structure that consists of a Mo-B sublattice interleaved with double layers of pure Al. In this regard, MoAlB has an atomically laminated structure quite analogous to that of the ternary transition metal carbides and nitrides, commonly referred to as MAX phases [1]. Recently, MoAlB was synthesized as a dense, predominantly single-phase ceramic and found to be quite oxidation resistant due to the formation of a well-adhered and protective Al_2O_3 scales up to 1350 °C in air [58, 59, 143], which shows that MoAlB has the potential to overcome some of the limitations faced by TMBs in high-temperature oxidizing environments.

Using resonant ultrasound spectroscopy (RUS), the room temperature (RT) Young's and shear moduli were measured to be 373 and 151 GPa, respectively. The corresponding values at 1200 °C were 320 GPa and 130 GPa, respectively, which are ~86% of RT values [59]. At 10.6 GPa, the Vickers hardness of MoAlB was considerably lower than those of MoB, MoB2, and most other binary TMBs [144, 145], but significantly higher than the typical MAX phase. However, as in MAX phases, the indentation marks in MoAlB lack the large, dominant cracks emanating from the corners that are commonly observed in brittle ceramics. The latter suggests that this material could have decent damage tolerance. In our previous work, we also reported ultimate compressive stresses, UCSs, between 1.4 and 1.9 GPa depending on the orientation of

*Reprinted with permission from "Compressive deformation of MoAlB up to 1100 °C" by Yexiao Chen et al., 2019. Journal of Alloys and Compounds, 774, 1216-1222. Copyright 2019 Elsevier.

the loading axis relative to the hot pressing direction [58]. In MoAlB ceramics fabricated by hot-pressing pre-reacted MoAlB powders, Xu et al. found similar compressive strengths (1.3-1.6 GPa) and hardness values (~9.3 GPa under a 30 N load). In addition, fracture toughness values of 4.3 MPa m1/2 and flexural strengths of 456 MPa at RT. [6, 61]

While these properties bode well for the potential use of MoAlB at high temperatures in ambient air, deeper understanding of its mechanical properties and of the operative deformation and failure mechanisms at both room and elevated temperatures is needed. The nanolaminated topology and large b/a and b/c ratios (i.e. ratio of lattice constant parallel to perpendicular to the stacking axis), are features that MoAlB shares with their damage tolerant MAX cousins, that can deform via intra-grain bending, kinking and delamination [4, 6, 7]. Most recently, deformation of MAX phases by ripplocation formation was also proposed in the literature [78, 146]. Based on the structural similarities, we postulated that the same micro-mechanisms could also play a major role in the deformation of MoAlB. For example, the nonlinear elastic behavior, first reported in Ti_3SiC_2 [74] and later in many other MAX phases [69-73, 76, 147-149], was anticipated at both room and higher temperatures.

To test this hypothesis and gain a general understanding of the mechanical properties of MoAlB over a wide temperature range, we quasi-statically and cyclically compressed polycrystalline samples up to 1100 °C in ambient air. The microstructural evolution, as a function of loading, was investigated using a scanning electron microscopy, SEM, to elucidate the dominant deformation and failure mechanisms.

5.2 Experimental Methods

A stoichiometric MoB (MoB with Mo:B atomic ratio 1:1, Alfa Aesar, 99%, < 38 μm) and Al powders were mixed in a 1.0:1.25 molar ratio in a polyethylene jar, and ball milled with ZrO_2 balls for 24 h. The powder mixtures were poured into a boron nitride-coated graphite die and pre-compacted at 30 MPa. The die was placed in a hot press (HP) and heated under mechanical vacuum (< 15 Pa) at a rate of 500 °C/h to 1200 °C and loaded to 25 MPa. The temperature and pressure were held for 5 h before cooling the HP naturally to room temperature. The bonded graphite from the as-sintered sample was ground off for sample characterization. Porosity of the samples was determined to be 0.36±0.10% by Archimedes method that is described in more details elsewhere [76, 148, 149]. A drop of a 2:1:2 part solution, by volume, of hydrofluoric acid (48-51 wt.%, Acros Organics), nitric acid (68%, Alfa Aesar, Ward Hill, MA) and water was placed on the sample for 5 s to etch the surface for grain size analysis. A grain size of 6 ±1 μm was calculated from representative etched SEM micrographs. However larger grains with lengths up to 30 μm were occasionally found.

Two kinds of cylindrical samples – smaller ones with 4 mm diameter and 8 mm length and larger ones with 8 mm diameter and 17 mm length were machined by wire electro-discharge machining (Wire-EDM). Dimensions of the small cylinders were selected not to exceed the load limits of the SiC pushrods used for high-temperature testing at the ultimate compressive strength of the specimens, while the large cylinders are designed to allow attachment of the high-accuracy, high-temperature extensometer. The smaller samples were quasi-statically compressed to failure using a servo-hydraulic

testing machine (MTS-810, MTS, USA) with SiC pushrods at a constant crosshead displacement rate corresponding to a strain rate of 10^{-4} s^{-1}. Cyclic compression testing was carried out on the larger samples at a frequency of 0.5 Hz, at two amplitude stresses, namely 250 MPa and 650 MPa, using the same testing machine. However, in the latter case an axial extensometer (632.59, MTS, USA) attached directly to the samples was used to measure the strains. A preload stress of 55 MPa was applied before each test to ensure good sample alignment and firm contact between sample and pushrods, and samples were loaded to the amplitude stress and then unloaded back to the preload stress, for 10 cycles, while monitoring force and strain.

After compression testing, selected samples were cut down the middle along the compression loading direction. The so exposed cross-sections were mechanically polished using sand paper and 3 to 0.1 μm diamond suspensions. For the final polishing step, a 0.05 μm colloidal silica solution was used. After polishing the samples were imaged using SEM Quanta 600 FEG (FEI, Oregon, USA) Scanning Electron Microscope.

5.3 Results and Discussion

5.3.1 Oxidation resistance of MoAlB

The mass gains per unit area, $\Delta W/A$, as a function of time, t, when bulk MoAlB samples were oxidized in ambient air at 1200, 1300, and 1350 °C are shown in **Figure 5.1**a [143]. The mass gain (typically <0.003 kg/m^2 at all T) that occurred during heating to the desired temperature was accounted for by subtracting the mass gained from samples heated at the same rate to the desired temperatures with no subsequent

isothermal holding time. At 1200 °C, the mass increased steadily, without strong signs of asymptotic behavior. On the other hand, the mass increased rapidly within the first 5 h at 1300 and 1350 °C, after which the oxidation rates slow down significantly. The crossed, open green triangles in **Figure 5.1**a show ΔW/A as a function of time up to 125 one-hour long cycles, assuming the total oxidation time is equal to only the time spent at 1200 °C. Gradual mass gain is observed over the course of the 125 cycles, resulting in a small final mass gain of 2.15×10^{-2} kg/m^2. This mass gain is slightly higher than the 1.7×10^{-2} kg/m^2 measured after isothermal testing for 100 h. This is not surprising given the samples that are cycled spend more time at elevated temperatures (~40 minutes more per cycle at T > 1000 °C) than those during the static oxidation tests at 1200 °C.

To gain further insight into the rate controlling mechanism, we applied the approach of Smialek et al. to analyze our results for temperatures above 1200 °C, at which continuous, protective oxide scales form [53]. The Arrhenian plot of $\delta D_{gb,O,int}$ in **Figure 5.1**b and agree well with those predicted in for FeCrAl-based alloy Hoskins 875 and Al_2O_3-forming MAX phases. Thus, it is likely that oxygen grain boundary diffusivity is also the rate controlling mechanism for the formation of Al_2O_3 scales on MoAlB.

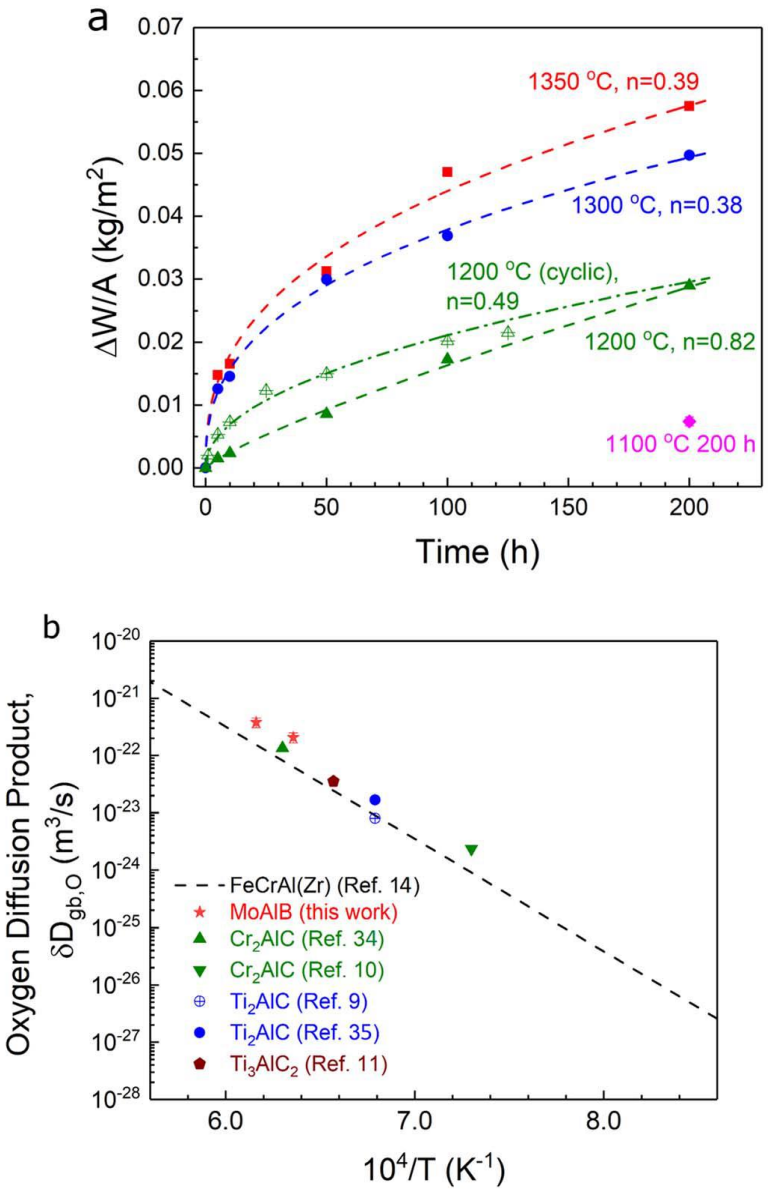

Figure 5.1 (a) Mass gain per unit surface area as a function of isothermal oxidation time for bulk MoAlB samples; (b) Oxygen grain boundary diffusivity of MoAlB compared to Hoskins 875 FeCrAl(Zr) alloy and select MAX phases [143].

5.3.2 Temperature dependence of ultimate compressive strength (UCS)

Figure 5.2a shows selected, but typical engineering stress vs. relative crosshead displacement curves and calculated UCS of MoAlB at different temperatures. Note that engineering stress was determined as load divided by initial cross-section area of the sample, while relative crosshead displacement was calculated as crosshead displacement divided by initial height of the sample. At RT, and below 800 °C, the mechanical response is linear elastic until brittle failure. Between 800 and 900 °C, the material starts to show some plastic deformation but still fails in a predominantly brittle manner, i.e. it shatters in a large number of small pieces. Above 1000 °C, extensive plastic deformation is observed. These results suggest the presence of a brittle to plastic, BPT, transition. The reason it is referred to as a BPT and not the more common brittle-to-ductile transition is to emphasize that the transition is not a result of the activation of additional slip systems. Here (see below), like in the MAX phases, the transition is typically accompanied by distributed damage in the form of cracks and delaminations [150]. Just below the BPT temperature, between 600-800 °C, the UCS slightly increases with increasing temperature. The significant drop in UCS above 800 °C (**Figure 5.2**b) together with the increases in strain to failure, is evidence that MoAlB goes through a brittle-to-plastic transition (BPT) similar to that observed for the MAX phases. [4, 75, 151]

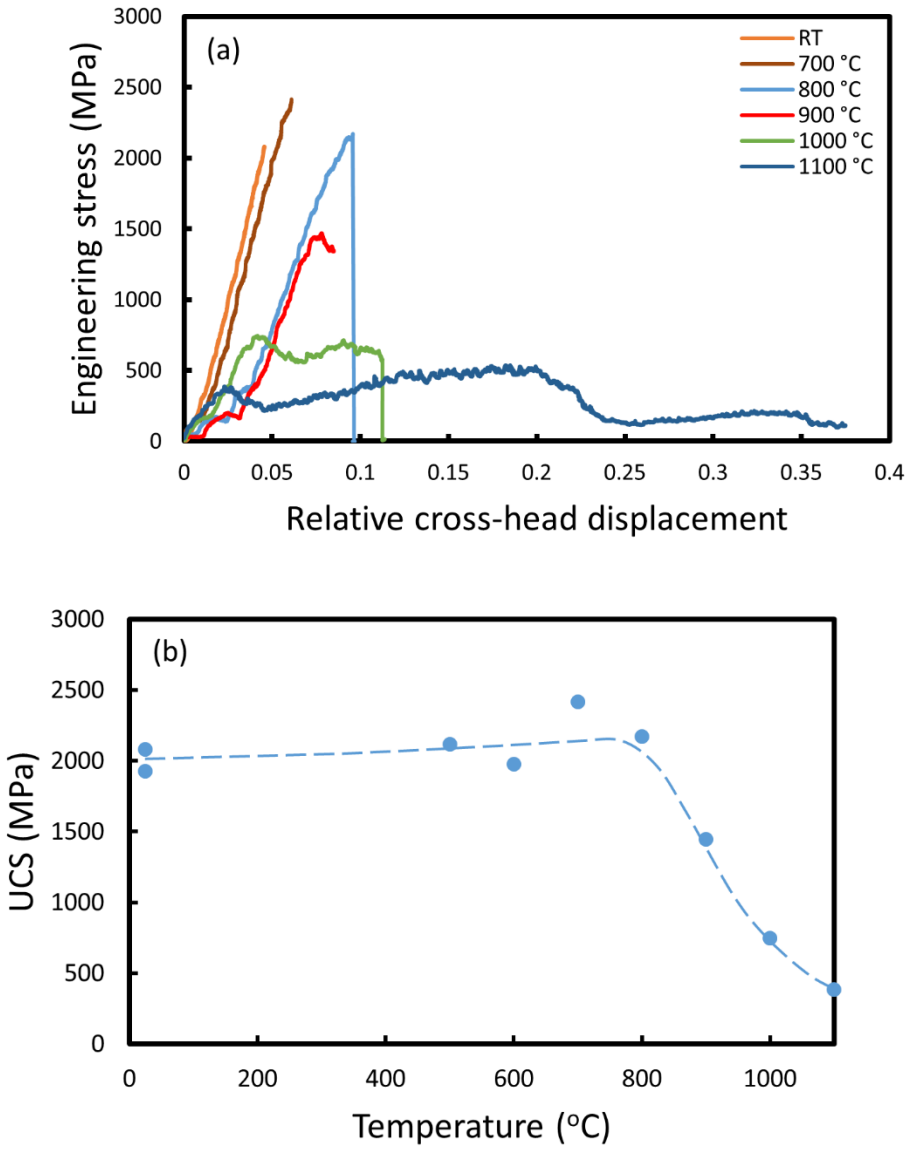

Figure 5.2 (a) Selected engineering stress vs. relative cross-head displacement curves at RT, around BPT and above BPT temperature; (b) Effect of temperature on UCS of MoAlB. Relative displacement was determined as a cross-head displacement divided by the initial length of the sample.

5.3.3 Quasi-static compression

Selected but typical engineering stress-strain curves obtained using the larger samples (8 mm dia. and 17 mm long) are shown in **Figure 5.3**, for samples tested at RT and 1100 °C. Note here that maximum applied engineering stress in this case was limited to 1.5 GPa which is the load bearing capacity of our SiC pushrods. In other words, the sample tested at RT (**Figure 5.3**) did not fail at 1.5 GPa, although its stress-strain curve was linear-elastic up to that stress.

At 1100 °C, the response was more complicated. The typical stress-strain curve shows the material initially goes through a linear-elastic regime, after which a transient "hardening" region can be observed (lower curve in **Figure 5.3**). Subsequently, a distinct softening regime is reached, followed by another hardening region where the test is interrupted at 9% strain the limit of our extensometer. In sharp contrast to most MAX phases, no hysteresis was observed, at RT. However, above the BPT temperature the overall stress-strain behavior is quite similar to that observed in MAX phases in which strains to failure exceed 15 % in compression at 1100 °C [80, 152] and 20 % in tension at 1200 °C [151].

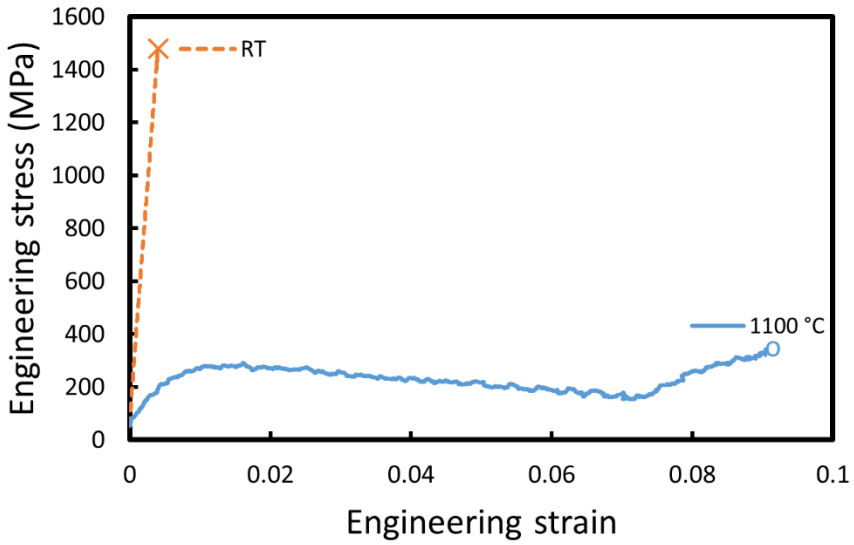

Figure 5.3 Typical engineering stress-strain curves obtained in quasi-static compression at RT and 1100 °C. The RT temperature sample did not fail; the test was interrupted to protect the SiC platens.

5.3.4 Cyclic compression

The response of MoAlB at RT, 700, 800, 900 and 1000 °C to cyclic loading up to stresses of 250 MPa and 650 MPa using a frequency of 0.5 Hz is shown in **Figure 5.4**. The following points are salient for samples cyclically loaded to 650 MPa: (i) the slope of the initial linear part is consistent with E values determined by resonant ultrasound spectroscopy (RUS) indicated by dashed red lines in **Figure 5.4** [59]; (ii) at RT and 700 °C, no hysteresis was detectable; (iii) Nonlinear stress-strain behavior and irrecoverable deformation can be observed starting at 800 °C. All hysteretic stress-strain loops above 800 °C, are not fully reversible, as indicated by colored loop of successive cycles at 1000 °C and 650 MPa where 1st, 5th and 10th cycles are highlighted in blue, orange and red color, respectively. Said otherwise, some irrecoverable strain is recorded after each

loading cycle. The same is true for the samples cycled at 250 MPa (bottom panels in **Figure 5.4**); and, (iv) the amount of irrecoverable strain after unloading decreases with increasing number of loading cycles to 650 MPa, as well as the area of hysteresis loop (**Figure 5.5**). The latter indicates that mechanical energy dissipated in each loading-unloading cycle decreases with increasing number of cycles. The stress-strain curves obtained by loading up to 250 MPa (bottom row of panels in **Figure 5.4**) are qualitatively the same as those obtained at 650 MPa, but with smaller irrecoverable strains and smaller area of hysteresis loops, at and above 800 °C.

The observed stress-strain response of MoAlB below 800 °C is quite different than that of MAX phases since the latter show reproducible closed hysteresis loops even below their brittle to plastic transition temperature [4, 7]. However, the latter's mechanical responses in cyclic compressive loadings above BPT temperatures are qualitatively similar, with MoAlB having much higher strength at equivalent temperatures. The large irrecoverable strain after first loading-unloading cycle, that further decreases with each subsequent loading, can be observed in both materials, as well as the decreasing size of the hysteresis loop (i.e. energy dissipated per each loading cycle) with number of loading cycles, as is summarized in **Figure 5.5**.

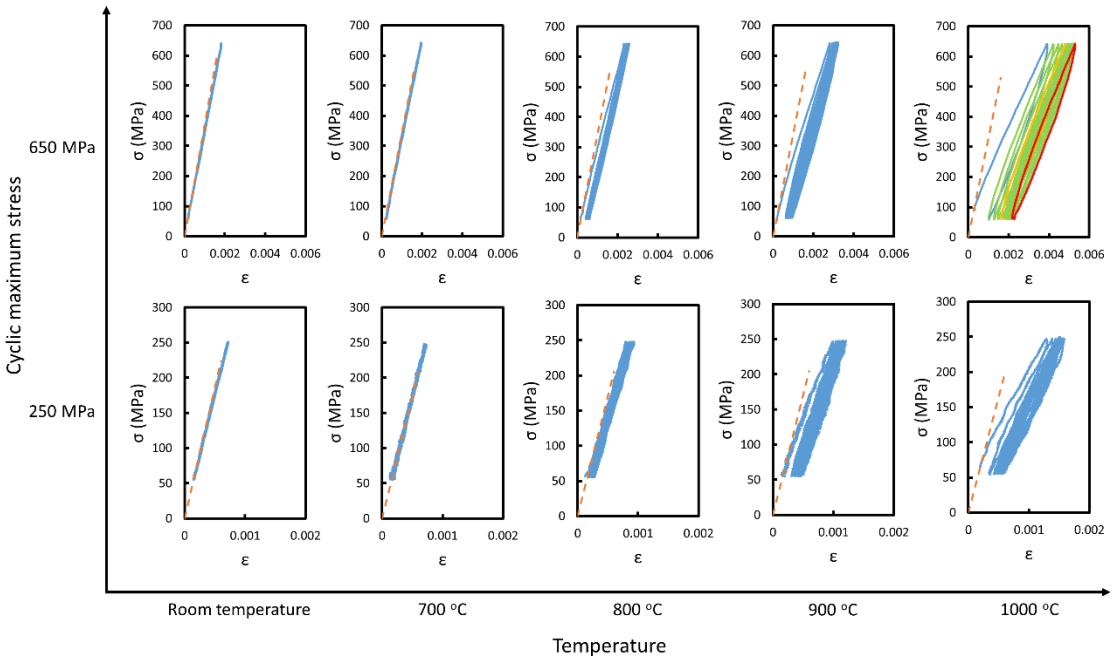

Figure 5.4 Engineering stress-strain behavior of MoAlB cyclically loaded/unloaded for 10 cycles with a frequency of 0.5 Hz up to amplitude stresses of 650 MPa (top row) or 250 MPa (bottom row) at temperatures indicated. The dashed lines are the linear elastic response expected from RUS [59].

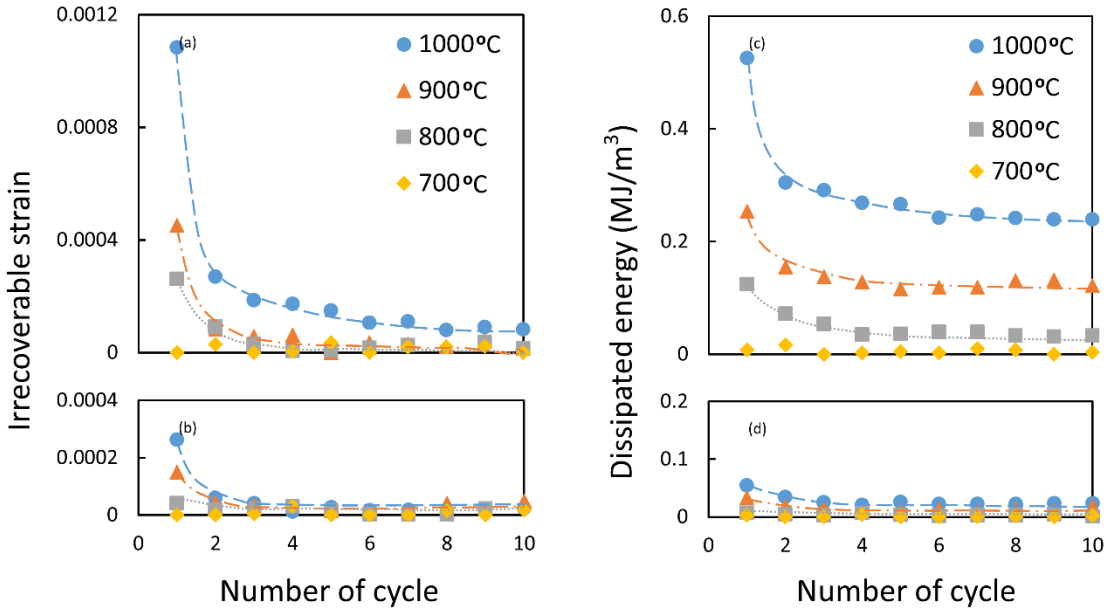

Figure 5.5 Irrecoverable strain under (a) 650 MPa and (b) 250 MPa, and dissipated energy under (c) 650 MPa and (d) 250 MPa, as a function of number of cycles determined from the stress-strain curves shown in Figure 5.4.

5.3.5 Microstructural characterization of compressed samples

Figure 6 shows select, but typical, cross-sectional SEM micrographs of as-sintered MoAlB sample before cyclic compression, (**Figure 5.6**a), after 10 cycles cyclic compression loading to 650 MPa at 700 °C (**Figure 5.6**b) and 900 °C (**Figure 5.6**c), and quasi-static loading to 9% strain at 1100 °C (**Figure 5.6**d-f). In general, the as-sintered sample (**Figure 5.6**a) and those cyclically compressed at temperatures below BPT, such as that loaded at 700 °C in **Figure 5.6**b, are comparable in that they both show the same micro-laminated structure, with visible trans-granular delamination along basal planes. After cyclic compression to 650 MPa at 900 °C, bending of individual grains can be observed, as well as transgranular microcracks perpendicular to the basal planes (**Figure**

5.6c). Eventually, the microcracks coalesce into larger cracks at higher temperatures, as illustrated in the case of quasi-statically loaded sample at 1100 °C in **Figure 5.6**d and e. **Figure 5.6**f, at a higher magnification, reveals that some delaminations cracks do not extend along the entire grain, suggesting that delamination is concomitant with bending or kinking of individual grains.

No visible damage accumulation except the above mentioned transgranular delaminations in samples loaded in compression, was observed below the BPT temperature. However, as illustrated in **Figure 5.7** for the sample quasi-statically compressed at 1100 °C, intergranular cracking and voids accumulate in the microstructure, most notably within a shear band (denoted by blue lines in **Figure 5.7**) that is oriented approximately 45^{o} relative to the direction of the applied stress. This shear region also contains bent and kinked grains as those shown in **Figure 5.6**d and e. Finally, it is also important to note that macroscopic cracks are only observed in the crack-rich region (shear band).

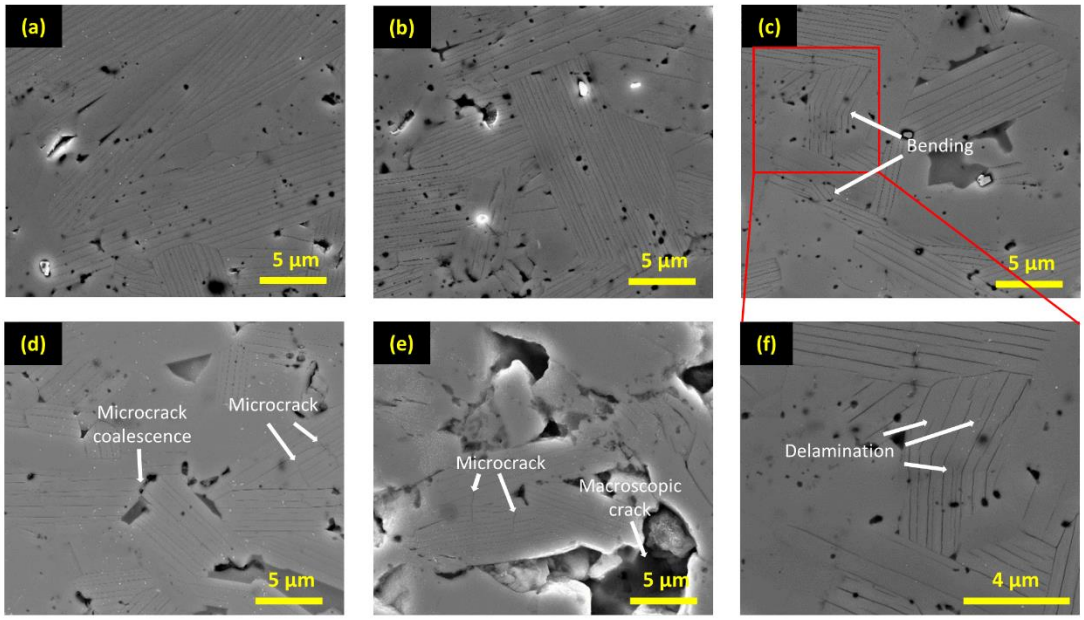

Figure 5.6 SEM images of selected MoAlB samples: (a) as-produced; after cyclic compression to 650 MPa, (b) at 700 °C and, (c, f) at 900 °C; after quasi-static compression to a strain of 9 % at 1100 °C from, (d) the crack-free region and, (e) crack-rich region (shear band) that are marked in Figure 6. In all figures, the compressive load was applied in the vertical direction.

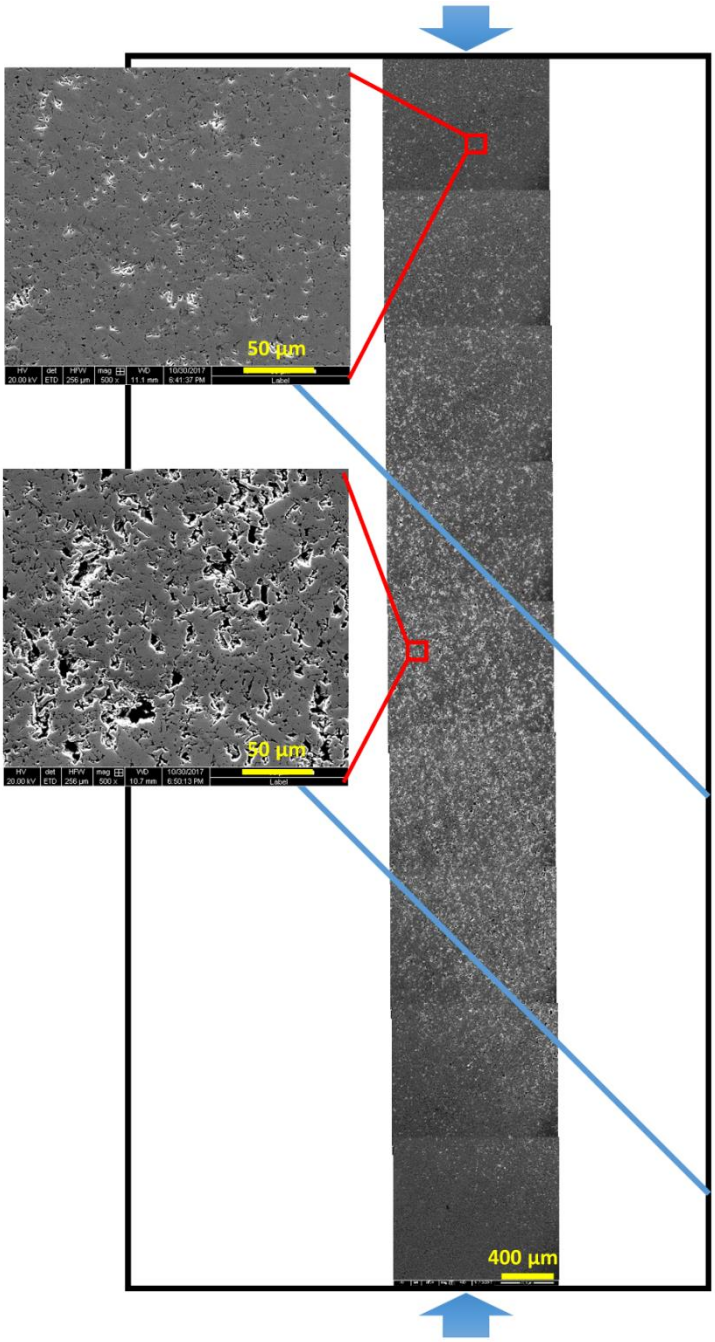

Figure 5.7 SEM images taken along the longitudinal axis of the sample's cross-section after quasi-static compression to a strain of 9% at 1100 °C. The black frame outlines the entire sample, while the blue dashed lines highlight a shear band. Arrows denote loading direction.

5.4 Discussion

The results presented in **Figure 5.2** to **Figure 5.4** clearly show that below 800 °C, MoAlB responds to compressive stresses in a linear elastic manner. This is evidenced by the fact that slopes of the stress-strain curves are in excellent agreement with those measured using RUS shown by dashed red lines in **Figure 5.4**). The failure is brittle, with UCS in the order of 2 to 2.5 GPa. These values are noteworthy given the grain size (≈ 5-30 μm, **Figure 5.6**) of the samples tested, compared to typical MAX phases [71, 79, 127, 150]. This linear elastic response in MoAlB is different than that of most MAX phases, wherein under compression the response at room temperature is hysteretic [4, 7, 74, 76, 78, 146, 147, 153-156]. It is worth noting, however, that Ti_2SC as a MAX phase wherein the Ti-S bonds are relatively strong and that is harder than most of the other MAX phases, also responds in a linear elastic fashion when loaded in compression at RT [157].

Above the BPT temperature, however, both the MAX phases and MoAlB deform plastically with extensive strains to failure – at the higher temperature ends – in compression (note 9 % strain in **Figure 5.3** is not the failure strain, but rather the strain at which the test was interrupted). Another similarity is the significant drop in UCS with increasing temperature. Above the BPT temperature, especially at 1100 °C, the stress-displacement curve in MoAlB exhibits a linear elastic region, followed by a region of apparent "hardening" and then gradual softening. In other words, MoAlB starts to creep due to microcracking. The reason for the second apparent hardening at strains exceeding

7% (**Figure 5.3**) is unclear at this time, but could possibly be related to the significant increase in the cross-sectional area (~48 %) due to "barreling" of the sample.

Observed differences in macroscopic stress-strain behavior below and above BPT temperature can be also traced back to microstructural changes. Although no significant microstructural changes can be observed in samples loaded below the BPT temperature (compare **Figure 5.6**a and b), the microstructures of the samples loaded above the BPT temperature (**Figure 5.6**c-f) show the presence of bent and kinked individual grains, extensive transgranular delamination along basal planes, microcracking and microcrack coalescence. It is reasonable to assume at this juncture that the microcracks, delaminations, etc., are associated to the hysteretic behavior.

Considerable bending and kinking of individual grains has been widely observed in different MAX phases (e.g. Ti_3SiC_2, Ti_2AlC, Ti_3AlC_2, Cr_2AlC, etc. [69-73, 149]). When the strain is recoverable, those deformation processes are responsible for the energy dissipation during cyclic loading observed both below and above their BPT temperatures. However, compared to MAX phases, the occurrence of grain bending and kinking is relatively rare in MoAlB even above the BPT temperature, which renders this mechanism unlikely to be the major cause of the observed energy dissipation and irrecoverable strains observed (**Figure 5.5**) at and above 800 °C. Even after quasi-static compression, cracks are more commonly observed than grain bending in MoAlB loaded above BPT temperatures as illustrated in **Figure 5.6**. Therefore, other microstructural changes, especially transgranular delamination and microcracking, may play important roles in the observed hysteretic behavior.

The kinking model is not the only one used to explain the hysteretic behavior in MAX phases. Instead, Poon *et al.* [77] used an alternate model, which explained the nonlinear hysteretic behavior of MAX phases by formation of microcracks and energy dissipation due to friction between crack surfaces during cyclic loading. Although, that model was not successful in completely capturing the macroscopic hysteretic behavior of the MAX phases, in which extensive bending and kinking of individual grains occurs during loading, it might better explain the observed macroscopic stress-strain behavior of MoAlB. In other words, extensive microcracking and delamination above the BPT temperature result in irrecoverable strains and the observed hysteretic behavior in compression, rather than bending and kinking of individual grains that is apparently more difficult in MoAlB.

This difference could be traced to differences in crystal structures and bonding strengths. Although MAX phases and MoAlB share a similar structure in which Al layer(s) interleave a ceramic sublattice, the crystal structure of MAX phases is hexagonal while that of MoAlB is orthorhombic with strong covalent zig-zag B-B single chains – that are along <001> – within the Mo-B sublattice [28]. The latter results in greater stiffness within the Mo-B blocks when compared to the M-X blocks in the MAX phases. Also, while the C-Al distance in the MAX phases is of the order of 3.8 Å, the Al-B distance at 2.3 Å, is significantly shorter, signifying a much stronger bond in MoAlB. Moreover, the Al-B bonds are even shorter than the B-Mo bonds, within the BM_6 trigonal prisms of the MB blocks, which also supports the notion that the bonding between the Mo-B and Al layers is quite strong. At 151 GPa, the shear modulus of

MoAlB is significantly higher than the typical shear modulus of all 211 Al-containing MAX phases with which they can be compared [1, 4]. The shear modulus of MoAlB is closer to that of 312 and 413 Al-containing MAX phases. The fact that the MoAlB structure contains two Al layers, instead of one in the MAX phases, renders it elastic properties even more exceptional and must explain, at least in part its resistance to deformation. Thus, MoAlB is less prone to kinking and grain bending than MAX phases which explains the lack of hysteresis at room temperature, and even relatively small amount of bending and kinking observed above BPT temperature. Above the BPT temperature, although some MoAlB grains are bent, delaminations and microcracking is more dominant, especially within the shear band. The latter can be considered responsible for observed open hysteresis loops in compression. Recently it was postulated that ripplocations and not dislocations are responsible for the energy dissipation in layered solid in general and the MAX phases in particular [78]. For ripplocations to nucleate and propagate, sliding and bending of layers is required. However, strengths of the bonds alluded to above, together with the high elastic properties may be what is preventing the nucleation of ripplocations. Nevertheless, more work is needed to understand completely the origin of the hysteretic stress-stain behavior of MoAlB above its BPT temperature.

Lastly, the fact that UCSs > 2 GPa were measured herein, at temperatures up to 800 °C, is noteworthy. These values are even more impressive when the grain size is considered. Typically, at RT, the strengths of ceramics, decrease with increasing grain sizes. A very fruitful avenue of research would be to fabricate MoAlB samples with sub-

micron grains and measure their UCSs as it is not unreasonable to expect higher UCS. Exceptionally high UCS numbers reported here are indirect evidence that not only are the grain resistant to deformation, but more importantly, so are the grain boundaries. The fact that MoAlB is readily EDM machinable, forms an alumina layer at higher temperatures when heated in air, and lower density, (6.45 g/cm^3), together with the fact that above 900 °C they can deform significantly and can sustain a large amount of damage before final failure, bodes well for its potential use as a high temperature structural material. Before this can be assessed, it is important to measure its creep properties.

5.5 Summary

The results of uniaxial quasi-static and cyclic compression of MoAlB at temperatures up to 1100 °C show that open stress-strain hysteresis appear above a BPT temperature of 800 °C for this refractory ternary boride. Below the BPT temperature, MoAlB exhibits linear elastic behavior and fails in brittle manner at stresses exceeding 2 GPa, because the stress is insufficient to cause massive bending, kinking or any other deformation of individual grains. Therefore, this study shows that the mechanical response of MoAlB is quite different than those of the MAX phases wherein fully and spontaneously reversible stress-strain hysteresis loops are observed even below the BPT temperatures.

Above the BPT temperature extensive microcracking has been observed in MoAlB that appears to be predominantly localized in a shear band. Bending and kinking of individual grains, typically observed in MAX phases, was quite rare. Once the

microcracks form, not surprisingly, the process is irreversible, resulting in small irrecoverable strain in the first loading-unloading cycle. Starting from the second cycle, friction between the microcracked faces and delaminations are proposed to cause the dissipation of energy during each cycle, resulting in smaller stress-strain hysteresis loops with increasing number of loading cycles.

6. CONCLUSIONS AND FUTURE WORK

In this study, the oxidation behavior of two Al_2O_3-forming MAX phases namely Ti_2AlC and Cr_2AlC in 1000 to 1300 °C temperature range was investigated as well as mechanical properties of another promising alumina former, namely MoAlB. The major results and findings can be summarized as followings:

Results of this study reviled existence of five different phase regions during oxidation through a simple test on the wedge-shaped Ti_2AlC samples oxidized in 1000-1300 °C temperature range for different times, ranging from 5 min to 10h. In regions *I* and *II* at the thickest end of the wedge-shaped sample, a thin and protective, predominantly Al_2O_3 scale forms on the surface without any visible decomposition of Al deficient Ti_2AlC substrate. Moving toward the tip of the sample, the *Region III* can be observed with the ticker Al_2O_3 and TiO_y mixed oxide scale on the surface of the wedge-shaped sample, and decomposed Al depleted Ti_2AlC substrate to Ti_3AlC_2 and TiC phases. Breakaway oxidation was found to occur between Regions II and III when Al deficiency in Ti_2AlC reaches approximately 5%. Close to the tip of the wedge-shape samples (Regions IV and V), no Ti_2AlC or any other carbide phase can be detected anymore, as sample completely oxide forming ticker Al_2O_3 and TiO_y mixed oxide scale on the surface and TiO_2 in the middle of the sample (*Region IV)*, or only Al_2O_3 and TiO_y mixed oxide throughout the thickness at the very tip of the wedge-shaped sample (*Region V*).

Ti6242 and Ti_2AlC were successfully diffusion bonded by PECS at 800°C and 1000 using PECS under the processing condition of 800 °C, 5 MPa, C for 15 min.

However, since diffusion bonding at 1000 °C results in transformation of β phase into the α phase in Ti6242 substrate, only Ti6242-Ti_2AlC couples diffusion bonded at 800 °C where further selected to study the oxidation resistance and phase evolution in the Ti_2AlC-Ti6242 interface after extended exposure to temperatures up to 800 °C in ambient air.

Results of this study clearly show that after extended exposure of Ti_2AlC-Ti6242 to the ambient air, Al diffuses from Ti_2AlC into both Ti6242 substrate and oxide layer that forms on Ti_2AlC. Diffusion of the Al from Ti_2AlC into Ti6242 results in formation of two reaction sublayers at Ti_2AlC into Ti_2AlC-Ti6242 interface, the first one adjacent to Ti_2AlC costing mostly of $TiAl_2$ while the second one closer to Ti6242 consisting mostly of TiAl. In addition, further diffusion of Al from Ti_2AlC to Ti6242 substrate results in the formation of transformation zone, in which β phase Ti6242 completely transforms into the α phase. Thicknesses of both $TiAl_2$ and TiAl reaction sublayers and β→α transformation zone in Ti6242 increase with increasing exposure time to high temperatures, but they thicknesses do not exceeded ~5 μm, ~3 μm and ~12 μm, respectively, after exposure of Ti_2AlC-Ti6242 couple to 800 °C for 100 h.

In addition, fast diffusion of Al from Ti_2AlC layer in Ti_2AlC-Ti6242, and its preferential oxidation, results in the formation of the protective Al_2O_3 oxide scale if thickness of Ti_2AlC is above some critical value. Oxidation studies using Ti6242 samples diffusion boded to tapered Ti_2AlC clearly show that as Al diffuses form Ti_2AlC into both Ti6242 and oxide scale, Al depleted Ti_2AlC layer with thickens below the critical value does not oxidize any more to form protective Al_2O_3 scale, but rather a non-

protective oxide scale costing of TiO_2+Al_2O_2 mixture. This critical thickens of the Ti_2AlC layer at which oxidation breakaway occurs was found to be a strong function of oxidation temperature. More importantly, no oxygen was detected in Ti642 substrate after long term exposure of Ti_2AlC-Ti6242 couples to elevated temperatures and ambient air. The latter is particularly important, since oxygen diffusion into Ti6242 beyond TiO_2 that forms on its surface during oxidation, results in it significant embrittlement.

Results obtained in this study clearly suggest that Ti_2AlC can be used successfully as an environmental barrier coating on Ti6242 to protect it if from the rapid oxidation and oxygen embrittlement at elevated temperatures, thus extending its potential application up to ~800 °C. However, the thickness of the protective Ti_2AlC has to be carefully designed for different temperatures and exposure times to avoid significant Al depletion in Ti_2AlC, and consequently its breakaway oxidation, due to continuous diffusion of Al from Ti_2AlC into both protective Al_2O_3 scale and Ti6242 substrate.

Results of this study shows that pure Cr_2AlC can forms a pure and dense Al_2O_3 layer, like other alumina forming MAX phases during oxidation at high temperatures, only when access Al is present in grain boundaries, most likely in the form of aluminum rich Cr-Al solid solutions or intermetallic. With the presence of Cr_7C_3 secondary phase, the Cr_2AlC is deficient of excess Al and it form Cr_7C_3 sublayer in Al deficient Cr_2AlC beneath the Al_2O_3 layer.

It has been also shown that the he morphology and spallation resistance of the Al_2O_3 layer is significantly influenced by impurities such as Fe and S, and most likely luck of excess Al. Oxide layers on the samples with different amount of impurities results in the formation of planar, convoluted or wrinkled oxide scale. The morphology of the oxide scale is determined by the rate of the lateral growth of the oxide scale that can be fostered by presence of impurities such as Fe, and adhesion of the oxide scale to the substrate. The latter in turn depends on the tendency for segregation of impurities (such as S) in the interface between oxide scale and substrate, and presence or lack off Cr_7C_3 subscale that forms in Al-depilated zone beneath the oxide scale. Results in this study show that the addition of excess Al and use of starting powders with no impurities such as Fe and S, can foster formation of protective and more spallation resistant Al_2O_3 oxide scale during oxidation of Cr_2AlC. However, both factors contribute to formation of convoluted and wrinkled oxide scale, rather than planar one.

The results of uniaxial quasi-static and cyclic compression of MoAlB at temperatures up to 1100 °C show that open stress-strain hysteresis appear above a BPT temperature of 800 °C for this refractory ternary boride. Below the BPT temperature, MoAlB exhibits linear elastic behavior and fails in brittle manner at stresses exceeding 2 GPa, because the stress is insufficient to cause massive bending, kinking or any other deformation of individual grains. Therefore, this study shows that the mechanical response of MoAlB is quite different than those of the MAX phases wherein fully and spontaneously reversible stress-strain hysteresis loops are observed even below the BPT temperatures.

Above the BPT temperature extensive microcracking has been observed in MoAlB that appears to be predominantly localized in a shear band. Bending and kinking of individual grains, typically observed in MAX phases, was quite rare. Once the microcracks form, not surprisingly, the process is irreversible, resulting in small irrecoverable strain in the first loading-unloading cycle. Starting from the second cycle, friction between the microcracked faces and delaminations are proposed to cause the dissipation of energy during each cycle, resulting in smaller stress-strain hysteresis loops with increasing number of loading cycles.

The results presented in this thesis answer several key questions that are currently needed to better understand oxidation and mechanical properties of alumina forming MAX and MAB phases that would foster their design for application as structural materials and protective coatings for extreme environments. However, it also opens new questions that should be explored in the near future, such as:

1. *Can testing of wedge-shaped samples can be useful to screen fast out other Al_2O_3 forming MAX phases, such as Ti_3AlC_2 and Cr_2AlC for the breakaway oxidation conditions?* This work suggests that oxidation testing of wage-shaped samples offers considerable potential to find out the critical breakaway oxidation conditions for Ti_2AlC where a decomposition occurs from Ti_2AlC to Ti_3AlC_2 and TiC. It would be efficiently useful to apply the same approach to other Al_2O_3 forming MAX phases such as Ti_3AlC_2 and Cr_2AlC.

2. *Will microstructure such as grain orientation and grain size affect the Al_2O_3 forming process?* Our results suggest for the first time that Al diffuses along Cr_2AlC

grain boundaries faster than in grains, and that excess Al in grain boundaries contributes to the formation of pure alumina oxide scale, which is highly desired for oxidation resistant alumina forming materials. Since the Al_2O_3 forming process is controlled by O diffusion along Al_2O_3 grain boundaries with sufficient Al from the base material, the increase in grain size will cause decrease in the number of Al-rich grain boundaries impurities and further reduce Al diffusion from the base material.

3. *What are conditions for breakaway oxidation in Al_2O_3-forming MAB phases?* MoAlB has also been demonstrated to have good oxidation resistance because of its Al_2O_3 forming process and high mechanical strength at elevated temperatures in this work, which makes it potentially good candidate material for high-temperature structural applications in oxidizing envelopments. In the MAB phase system, there are other Al-containing MAB phases such as Cr_2AlB_2, Fe_2AlB_2, Mn_2AlB_2, etc. that still needs to be evaluated for high temperature applications, and compared to other alumina forming materials.

REFERENCES

1. Barsoum, M.W., *MAX phases: properties of machinable ternary carbides and nitrides*. 2013: John Wiley & Sons.
2. Barsoum, M.W., *The MN+1AXN phases: A new class of solids: Thermodynamically stable nanolaminates.* Progress in Solid State Chemistry, 2000. **28**(1): p. 201-281.
3. Sokol, M., et al., *On the Chemical Diversity of the MAX Phases.* Trends in Chemistry, 2019. **1**(2): p. 210-223.
4. Barsoum, M.W. and M. Radovic, *Elastic and Mechanical Properties of the MAX Phases*, in *Annual Review of Materials Research, Vol 41*, D.R. Clarke and P. Fratzl, Editors. 2011. p. 195-227.
5. Barsoum, M.W. and T. El-Raghy, *Synthesis and Characterization of a Remarkable Ceramic: Ti3SiC2.* Journal of the American Ceramic Society, 1996. **79**(7): p. 1953-1956.
6. Radovic, M. and M.W. Barsoum, *MAX phases: Bridging the gap between metals and ceramics.* American Ceramic Society Bulletin, 2013. **92**(3): p. 20-27.
7. Radovic, M., et al., *On the elastic properties and mechanical damping of Ti3SiC2, Ti3GeC2, Ti3Si0.5Al0.5C2 and Ti2AlC in the 300–1573K temperature range.* Acta Materialia, 2006. **54**(10): p. 2757-2767.
8. Martini, C., et al., *Sliding and abrasive wear behaviour of boride coatings.* Wear, 2004. **256**(6): p. 608-613.
9. Shappirio, J., et al., *TiB2 and ZrB2 diffusion barriers in GaAs Ohmic contact technology.* Journal of Vacuum Science & Technology A: Vacuum, Surfaces, and Films, 1985. **3**(6): p. 2255-2258.
10. Aylett, B.J., *Borides and Silicides - New Chemistry and Applications.* British Polymer Journal, 1986. **18**(6): p. 359-363.
11. Sani, E., et al., *Optical properties of dense zirconium and tantalum diborides for solar thermal absorbers.* Renewable Energy, 2016. **91**: p. 340-346.
12. Schlatter, J.C., et al., *Catalytic behavior of selected transition metal carbides, nitrides, and borides in the hydrodenitrogenation of quinoline.* Industrial & engineering chemistry research, 1988. **27**(9): p. 1648-1653.
13. Vrubel, H. and X. Hu, *Molybdenum Boride and Carbide Catalyze Hydrogen Evolution in both Acidic and Basic Solutions.* Angewandte Chemie, 2012. **124**(51): p. 12875-12878.
14. Fahrenholtz, W.G., et al., *Refractory Diborides of Zirconium and Hafnium.* Journal of the American Ceramic Society, 2007. **90**(5): p. 1347-1364.
15. Okada, S., et al., *Single-crystal growth and properties of CrB, Cr3B4, Cr2B3 and CrB2 from high-temperature aluminum solutions.* Journal of Crystal Growth, 1996. **166**(1): p. 429-435.
16. Steinitz, R., I. Binder, and D. Moskowitz, *System Molybdenum-Boron and Some Properties of The Molybdenum-Borides.* JOM, 1952. **4**(9): p. 983-987.
17. Ptačinová, J., et al., *Oxidation stability of boride coatings.* Kovove Mater, 2015. **53**: p. 1-12.

18. Voitovich, R. and É. Pugach, *Oxidation of refractory compounds. III- Borides of group-VI metals.* Poroshkovaia Metallurgiia, 1974: p. 86-92.
19. Kota, S., M. Sokol, and M.W. Barsoum, *A progress report on the MAB phases: atomically laminated, ternary transition metal borides.* International Materials Reviews, 2019: p. 1-30.
20. Halla, F. and W. Thury, *Über Boride von Molybdän und Wolfram.* Zeitschrift für anorganische und allgemeine Chemie, 1942. **249**(3): p. 229-237.
21. Jeitschko, W., *Die Kristallstruktur von MoAlB.* Monatshefte für Chemie und verwandte Teile anderer Wissenschaften, 1966. **97**(5): p. 1472-1476.
22. Zhang, Y., et al., *Synthesis of a New Compound WAlB by the Use of Aluminium Flux.* Journal of the Ceramic Association, Japan, 1987. **95**(1100): p. 374-380.
23. Yu, Y. and T. Lundström, *Crystal growth and structural investigation of the new quaternary compound Mo1−xCrxAlB with x = 0.39.* Journal of Alloys and Compounds, 1995. **226**(1): p. 5-9.
24. Okada, S., et al., *Single Crystal Growth of (MoXCr1−X)AlB and (MoXW1−X)AlB by Metal Al Solutions and Properties of the Crystals.* Journal of Solid State Chemistry, 1997. **133**(1): p. 36-43.
25. Becher, H.J., K. Krogmann, and E. Peisker, *Über das ternäre Borid Mn2AlB2.* Zeitschrift für anorganische und allgemeine Chemie, 1966. **344**(3‐4): p. 140-147.
26. STADELMAIER, H., R. BURGESS, and H. DAVIS, *THE FE-AL-B TERNARY SYSTEM.* METALL, 1966. **20**(3): p. 225-226.
27. Chaban, N.F. and Y.B. Kuz'ma, *Cr-Al-B and Mn-Al-B ternary systems.* Izvestiya Akademii Nauk SSSR, Neorganicheskie Materialy, 1973. **9**(11): p. 1908-1911.
28. Ade, M. and H. Hillebrecht, *Ternary Borides Cr2AlB2, Cr3AlB4, and Cr4AlB6: The First Members of the Series (CrB2)nCrAl with n = 1, 2, 3 and a Unifying Concept for Ternary Borides as MAB-Phases.* Inorganic Chemistry, 2015. **54**(13): p. 6122-6135.
29. Zhang, H., et al., *Crystal structure of Cr4AlB4: A new MAB phase compound discovered in Cr-Al-B system.* Journal of Materials Science & Technology, 2019. **35**(4): p. 530-534.
30. Barsoum, M.W., T. El‐Raghy, and L.U.J.T. Ogbuji, *Oxidation Of Ti3SiC2 in Air.* Journal of The Electrochemical Society, 1997. **144**(7): p. 2508-2516.
31. Tallman, D.J., B. Anasori, and M.W. Barsoum, *A Critical Review of the Oxidation of Ti2AlC, Ti3AlC2 and Cr2AlC in Air.* Materials Research Letters, 2013. **1**(3): p. 115-125.
32. Gupta, S., E.N. Hoffman, and M.W. Barsoum, *Synthesis and oxidation of Ti2InC, Zr2InC, (Ti0.5,Zr0.5)2InC and (Ti0.5,Hf0.5)2InC in air.* Journal of Alloys and Compounds, 2006. **426**(1): p. 168-175.
33. Zhou, Y.C., H.Y. Dong, and X.H. Wang, *High-Temperature Oxidation Behavior of a Polycrystalline Ti2SnC Ceramic.* Oxidation of Metals, 2004. **61**(5): p. 365-377.

34. Quadakkers, W.J. and M.J. Bennett, *Oxidation induced lifetime limits of thin walled, iron based, alumina forming, oxide dispersion strengthened alloy components.* Materials Science and Technology, 1994. **10**(2): p. 126-131.
35. Quadakkers, W.J. and K. Bongartz, *The prediction of breakaway oxidation for alumina forming ODS alloys using oxidation diagrams.* Materials and Corrosion, 1994. **45**(4): p. 232-241.
36. Pint, B.A., L.R. Walker, and I.G. Wright, *Characterization of the breakaway al content in alumina-forming alloys.* Materials at High Temperatures, 2004. **21**(3): p. 175-185.
37. Stott, F.H. *The oxidation of alumina-forming alloys*. in *Materials science forum*. 1997. Trans Tech Publ.
38. Prescott, R. and M.J. Graham, *The formation of aluminum oxide scales on high-temperature alloys.* Oxidation of Metals, 1992. **38**(3): p. 233-254.
39. Wang, X.H. and Y.C. Zhou, *High-Temperature Oxidation Behavior of Ti2AlC in Air.* Oxidation of Metals, 2003. **59**(3-4): p. 303-320.
40. Byeon, J.W., et al., *Microstructure and Residual Stress of Alumina Scale Formed on Ti2AlC at High Temperature in Air.* Oxidation of Metals, 2007. **68**(1): p. 97-111.
41. Li, S., et al., *Multiple crack healing of a Ti2AlC ceramic.* Journal of the European Ceramic Society, 2012. **32**(8): p. 1813-1820.
42. Sloof, W.G., et al., *Repeated crack healing in MAX-phase ceramics revealed by 4D in situ synchrotron X-ray tomographic microscopy.* Scientific Reports, 2016. **6**: p. 23040.
43. Yang, H.J., et al., *High temperature healing of Ti2AlC: On the origin of inhomogeneous oxide scale.* Scripta Materialia, 2011. **65**(2): p. 135-138.
44. Sundberg, M., et al., *Alumina forming high temperature silicides and carbides.* Ceramics International, 2004. **30**(7): p. 1899-1904.
45. Wang, X.H. and Y.C. Zhou, *Layered Machinable and Electrically Conductive Ti2AlC and Ti3AlC2 Ceramics: a Review.* Journal of Materials Science & Technology, 2010. **26**(5): p. 385-416.
46. Cui, B., D.D. Jayaseelan, and W.E. Lee, *Microstructural evolution during high-temperature oxidation of Ti2AlC ceramics.* Acta Materialia, 2011. **59**(10): p. 4116-4125.
47. Yang, H., et al., *Self-healing performance of Ti 2 AlC ceramic.* Journal of Materials Chemistry, 2012. **22**(17): p. 8304-8313.
48. S. Basu, N.O., A. Gowdy, I. Karaman and M. Radovic, *Long-Term Oxidation of Ti2AlC in Air and Water Vapor at 1000–1300°C Temperature Range.* J. Electrochem. Soc, 2012. **159**(2).
49. Liu, Z., W. Gao, and Y. He, *Modeling of Oxidation Kinetics of Y-Doped Fe–Cr–Al Alloys.* Oxidation of Metals, 2000. **53**(3): p. 341-350.
50. Kingery, W.D., *Introduction to ceramics.* 1976.
51. Smialek, J.L., et al., *Oxygen permeability and grain-boundary diffusion applied to alumina scales.* 2013.

52. Wada, M., T. Matsudaira, and S. Kitaoka, *Mutual grain-boundary transport of aluminum and oxygen in polycrystalline Al₂O₃ under oxygen potential gradients at high temperatures.* Journal of the Ceramic Society of Japan, 2011. **119**(1395): p. 832-839.
53. Smialek, J.L., *Oxygen diffusivity in alumina scales grown on Al-MAX phases.* Corrosion Science, 2015. **91**: p. 281-286.
54. Li, X., et al., *Breakaway oxidation of Ti3AlC2 during long-term exposure in air at 1100°C.* Corrosion Science, 2016. **104**: p. 112-122.
55. Maréchal, L., et al., *Oxidation Behavior of ODS Fe–Cr–Al Alloys: Aluminum Depletion and Lifetime.* Oxidation of Metals, 2003. **60**(1): p. 1-28.
56. Lin, Z.J., et al., *High-temperature oxidation and hot corrosion of Cr2AlC.* Acta Materialia, 2007. **55**(18): p. 6182-6191.
57. Al-Badairy, H., G.J. Tatlock, and M.J. Bennett, *A comparison of breakaway oxidation in wedge-shaped and parallel sided coupons of FeCrAl alloys.* Materials at High Temperatures, 2000. **17**(1): p. 101-107.
58. Kota, S., et al., *Synthesis and Characterization of an Alumina Forming Nanolaminated Boride: MoAlB.* Scientific Reports, 2016. **6**: p. 26475.
59. Kota, S., et al., *Elastic properties, thermal stability, and thermodynamic parameters of MoAlB.* Physical Review B, 2017. **95**(14): p. 144108.
60. Kota, S., et al., *Synthesis and characterization of the atomic laminate Mn2AlB2.* Journal of the European Ceramic Society, 2018. **38**(16): p. 5333-5340.
61. Xu, L., et al., *Synthesis, microstructure and properties of MoAlB ceramics.* Ceramics International, 2018. **44**(11): p. 13396-13401.
62. Shi, O., et al., *Synthesis and oxidation resistance of MoAlB single crystals.* Ceramics International, 2019. **45**(2, Part A): p. 2446-2450.
63. Morgiel, J., J. Lis, and R. Pampuch, *Microstructure of Ti3SiC2-based ceramics.* Materials Letters, 1996. **27**(3): p. 85-89.
64. Farber, L., *transmission electron microscopy study of a low-angle boundary in plastically deformed Ti3SiC2.* Philosophical Magazine Letters, 1999. **79**(4): p. 163-170.
65. Barsoum, M.W., L. Farber, and T. El-Raghy, *Dislocations, kink bands, and room-temperature plasticity of Ti3SiC2.* Metallurgical and Materials Transactions A, 1999. **30**(7): p. 1727-1738.
66. Hess, J. and C. Barrett, *Structure and nature of kink bands in zinc.* JOM, 1949. **1**(9): p. 599-606.
67. Frank, F.C. and A.N. Stroh, *On the Theory of Kinking.* Proceedings of the Physical Society. Section B, 1952. **65**(10): p. 811-821.
68. Barsoum, M.W. and T. El-Raghy, *Room-temperature ductile carbides.* Metallurgical and Materials Transactions A, 1999. **30**(2): p. 363-369.
69. Barsoum, M.W., D. Brodkin, and T. El-Raghy, *Layered machinable ceramics for high temperature applications.* Scripta Materialia, 1997. **36**(5): p. 535-541.
70. Sun, Z.M., et al., *Microstructure and mechanical properties of porous Ti3SiC2.* Acta Materialia, 2005. **53**(16): p. 4359-4366.

71. Tian, W., et al., *Compressive deformation behavior of ternary compound Cr2AlC.* Journal of Materials Science, 2009. **44**(1): p. 102-107.
72. Bei, G.P., et al., *Compressive Behavior of Ti3AlC2 and Ti3Al0.8Sn0.2C2MAX Phases at Room Temperature.* Journal of the American Ceramic Society, 2013. **96**(2): p. 567-576.
73. Benitez, R., et al., *Effects of microstructure on the mechanical properties of Ti2AlC in compression.* Acta Materialia, 2018. **143**: p. 130-140.
74. Barsoum, M.W., et al., *Fully reversible, dislocation-based compressive deformation of Ti3SiC2 to 1 GPa.* Nat Mater, 2003. **2**(2): p. 107-111.
75. Radovic, M., et al., *Effect of temperature, strain rate and grain size on the mechanical response of Ti3SiC2 in tension.* Acta Materialia, 2002. **50**(6): p. 1297-1306.
76. Benitez, R., et al., *Room temperature stress-strain hysteresis in Ti2AlC revisited.* Acta Materialia, 2016. **105**: p. 294-305.
77. Poon, B., et al., *Damage accumulation and hysteretic behavior of MAX phase materials.* Journal of the Mechanics and Physics of Solids, 2011. **59**(10): p. 2238-2257.
78. Gruber, J., et al., *Evidence for Bulk Ripplocations in Layered Solids.* Scientific Reports, 2016. **6**: p. 33451.
79. Tzenov, N.V. and M.W. Barsoum, *Synthesis and Characterization of Ti3AlC2.* Journal of the American Ceramic Society, 2000. **83**(4): p. 825-832.
80. Barsoum, M.W., et al., *Ti3SiC2 and ice.* Applied Physics Letters, 2001. **79**(4): p. 479-481.
81. Zhen, T., M.W. Barsoum, and S.R. Kalidindi, *Effects of temperature, strain rate and grain size on the compressive properties of Ti3SiC2.* Acta Materialia, 2005. **53**(15): p. 4163-4171.
82. Levin, E.M., et al., *Effects of Al content and annealing on the phases formation, lattice parameters, and magnetization of $\mathrm{A}{\mathrm{l}}_{x}\mathrm{F}{\mathrm{e}}_{2}{\mathrm{B}}_{2}\phantom{\rule{4pt}{0ex}}(x=1.0,1.1,1.2)$ alloys.* Physical Review Materials, 2018. **2**(3): p. 034403.
83. Zhou, Y., et al., *Electrical conductive and damage-tolerant nanolaminated MAB phases Cr2AlB2, Cr3AlB4 and Cr4AlB6.* Materials Research Letters, 2017. **5**(6): p. 440-448.
84. Bai, Y., et al., *High-temperature mechanical properties and thermal shock behavior of ternary-layered MAB phases Fe2AlB2.* International Journal of Refractory Metals and Hard Materials, 2019. **80**: p. 151-160.
85. Kádas, K., et al., *AlM2B2(M = Cr, Mn, Fe, Co, Ni): a group of nanolaminated materials.* Journal of Physics: Condensed Matter, 2017. **29**(15): p. 155402.
86. Li, X., M. Chagas da Silva, and D.R. Salahub, *First-principles calculations of the structural, mechanical, electronic and bonding properties of (CrB2)n CrAl with n = 1, 2, 3.* Journal of Alloys and Compounds, 2017. **698**: p. 291-303.
87. Lejeune, B.T., et al., *Anisotropic thermal conductivity of magnetocaloric AlFe2B2.* Materialia, 2018. **1**: p. 150-154.

88. Verger, L., et al., *Anisotropic thermal expansions of select layered ternary transition metal borides: MoAlB, Cr2AlB2, Mn2AlB2, and Fe2AlB2.* Journal of Applied Physics, 2018. **124**(20): p. 205108.
89. Dai, F.-Z., Z. Feng, and Y. Zhou, *First-principles investigation on the chemical bonding, elastic properties and ideal strengths of MoAlB and WAlB nanolaminated MAB phases.* Computational Materials Science, 2018. **147**: p. 331-337.
90. Smialek, J.L., *Kinetic Aspects of Ti2AlC MAX Phase Oxidation.* Oxidation of Metals, 2015. **83**(3): p. 351-366.
91. Park, M.S. and R. Arróyave, *Concurrent nucleation, formation and growth of two intermetallic compounds (Cu6Sn5 and Cu3Sn) during the early stages of lead-free soldering.* Acta Materialia, 2012. **60**(3): p. 923-934.
92. Yang, H.J., et al., *Self-healing performance of Ti2AlC ceramic.* Journal of Materials Chemistry, 2012. **22**(17): p. 8304-8313.
93. Lin, Z., et al., *Microstructures and Adhesion of the Oxide Scale Formed on Titanium Aluminum Carbide Substrates.* Journal of the American Ceramic Society, 2006. **89**(9): p. 2964-2966.
94. Boyer, R.R., *An overview on the use of titanium in the aerospace industry.* Materials Science and Engineering: A, 1996. **213**(1–2): p. 103-114.
95. Deka, D., et al., *Crystal plasticity modeling of deformation and creep in polycrystalline Ti-6242.* Metallurgical and Materials Transactions A, 2006. **37**(5): p. 1371-1388.
96. Odegard, B.C. and A.W. Thompson, *Low temperature creep of Ti-6 Al-4 V.* Metallurgical Transactions, 1974. **5**(5): p. 1207-1213.
97. Sai Srinadh, K.V. and V. Singh, *Oxidation behaviour of the near α-titanium alloy IMI 834.* Bulletin of Materials Science, 2004. **27**(4): p. 347-354.
98. Leyens, C., M. Peters, and W.A. Kaysser. *Oxidation and protection of near-alpha titanium alloys*. in *Materials science forum*. 1997. Trans Tech Publ.
99. Leyens, C., M. Peters, and W.A. Kaysser, *Influence of microstructure on oxidation behaviour of near-α titanium alloys.* Materials Science and Technology, 1996. **12**(3): p. 213-218.
100. Gurrappa, I., et al., *Influence of nitrogen implantation on the high temperature oxidation of titanium-base alloys.* Surface and Coatings Technology, 2006. **201**(6): p. 3536-3546.
101. Gaddam, R., et al., *Oxidation and alpha-case formation in Ti–6Al–2Sn–4Zr–2Mo alloy.* Materials Characterization, 2015. **99**: p. 166-174.
102. Gurrappa, I., *Platinum aluminide coatings for oxidation resistance of titanium alloys.* Platinum Metals Review, 2001. **45**(3): p. 124-129.
103. McKee, D.W. and K.L. Luthra, *Plasma-sprayed coatings for titanium alloy oxidation protection.* Surface and Coatings Technology, 1993. **56**(2): p. 109-117.
104. Radovic, M. and M.W. Barsoum, *MAX phases: bridging the gap between metals and ceramics.* American Ceramics Society Bulletin, 2013. **92**(3): p. 20-27.
105. Chen, Y., et al., *Breakaway oxidation of Ti2AlC MAX phase.* Material Research Letters, 2019. **under review**.

106. Wang, Q.M., et al., *Fabrication and oxidation behavior of Cr2AlC coating on Ti6242 alloy.* Surface and Coatings Technology, 2010. **204**(15): p. 2343-2352.
107. Benitez, R., et al., *Effects of microstructure on the mechanical properties of Ti2AlC in compression.* Acta Materialia, 2017.
108. Semiatin, S.L., et al., *Alpha/Beta Heat Treatment of a Titanium Alloy with a Nonuniform Microstructure.* Metallurgical and Materials Transactions A, 2007. **38**(4): p. 910-921.
109. Jiangwei, R., L. Yajiang, and F. Tao, *Microstructure characteristics in the interface zone of Ti/Al diffusion bonding.* Materials Letters, 2002. **56**(5): p. 647-652.
110. Zhou, Y. and Z. Sun, *Electronic structure and bonding properties in layered ternary carbide Ti3SiC2.* Journal of Physics: Condensed Matter, 2000. **12**(28): p. L457.
111. Hu, L., et al., *Fabrication and characterization of NiTi/Ti3SiC2 and NiTi/Ti2AlC composites.* Journal of Alloys and Compounds, 2014. **610**(0): p. 635-644.
112. Kothalkar, A., et al., *Interfacial study of NiTi–Ti3SiC2 solid state diffusion bonded joints.* Materials Science and Engineering: A, 2015. **622**(0): p. 168-177.
113. Smialek, J.L. and A. Garg, *Interfacial reactions of a MAX phase/superalloy hybrid.* Surface and Interface Analysis, 2015. **47**(8): p. 844-853.
114. Smialek, J.L., and Anita Garg, *Microstructure and Oxidation of a MAX Phase/Superalloy Hybrid Interface.* NASA/TM, 2014. **2014-216679**.
115. Tian, W., et al., *Oxidation behavior of Cr2AlC ceramics at 1,100 and 1,250 °C.* Journal of Materials Science, 2008. **43**(8): p. 2785-2791.
116. Hajas, D.E., et al., *Oxidation of Cr2AlC coatings in the temperature range of 1230 to 1410°C.* Surface and Coatings Technology, 2011. **206**(4): p. 591-598.
117. Li, S., et al., *Influence of grain size on high temperature oxidation behavior of Cr2AlC ceramics.* Ceramics International, 2013. **39**(3): p. 2715-2721.
118. Lee, D.B. and T.D. Nguyen, *Cyclic oxidation of Cr2AlC between 1000 and 1300°C in air.* Journal of Alloys and Compounds, 2008. **464**(1): p. 434-439.
119. Smialek, J.L., *Unusual Oxidative Limitations for Al-MAX Phases.* 2017.
120. Champagne, A., et al., *Phonon dispersion curves in Cr2AlC single-crystals.* Materials Research Letters, 2018. **6**(7): p. 378-383.
121. Gonzalez‐Julian, J., et al., *Environmental resistance of Cr2AlC MAX phase under thermal gradient loading using a burner rig.* Journal of the American Ceramic Society, 2018. **101**(5): p. 1841-1846.
122. Lee, D.B., et al., *Oxidation of Cr2AlC at 1300°C in air.* Corrosion Science, 2007. **49**(10): p. 3926-3934.
123. Haftani, M., et al., *Studying the oxidation of Ti2AlC MAX phase in atmosphere: A review.* International Journal of Refractory Metals and Hard Materials, 2016. **61**: p. 51-60.
124. Yang, Z.G. and P.Y. Hou, *Wrinkling behavior of alumina scales formed during isothermal oxidation of Fe–Al binary alloys.* Materials Science and Engineering: A, 2005. **391**(1): p. 1-9.

125. Tolpygo, V.K. and D.R. Clarke, *Wrinkling of α-alumina films grown by oxidation—II. Oxide separation and failure.* Acta Materialia, 1998. **46**(14): p. 5167-5174.
126. Scabarozi, T.H., et al., *Thermal expansion of select Mn+1AXn (M=earlytransitionmetal, A=Agroupelement, X=C or N) phases measured by high temperature x-ray diffraction and dilatometry.* Journal of Applied Physics, 2009. **105**(1): p. 013543.
127. MUNRO, M., *Evaluated Material Properties for a Sintered alpha-Alumina.* Journal of the American Ceramic Society, 1997. **80**(8): p. 1919-1928.
128. Stasik, M.C., et al., *Effects of reactive element additions and sulfur removal on the oxidation behavior of fecral alloys.* Scripta Metallurgica et Materialia, 1994. **31**(12): p. 1645-1650.
129. Li, D., Y. Xu, and D. Lin, *Oxidation behavior of FeAl alloys with and without titanium.* Journal of Materials Science, 2001. **36**(4): p. 979-983.
130. Tolpygo, V.K. and D.R. Clarke, *Wrinkling of α-alumina films grown by thermal oxidation—I. Quantitative studies on single crystals of Fe–Cr–Al alloy.* Acta Materialia, 1998. **46**(14): p. 5153-5166.
131. Golightly, F.A., G.C. Wood, and F.H. Stott, *The early stages of development of α-Al2O3 scales on Fe-Cr-Al and Fe-Cr-Al-Y Alloys at high temperature.* Oxidation of Metals, 1980. **14**(3): p. 217-234.
132. Golightly, F.A., F.H. Stott, and G.C. Wood, *The Relationship Between Oxide Grain Morphology and Growth Mechanisms for Fe‐Cr‐Al and Fe‐Cr‐Al‐Y Alloys.* Journal of The Electrochemical Society, 1979. **126**(6): p. 1035-1042.
133. Huntz, A.M., *Influence of active elements on the oxidation mechanism of M · Cr · Al alloys.* Materials Science and Engineering, 1987. **87**: p. 251-260.
134. Messaoudi, K., A.M. Huntz, and B. Lesage, *Diffusion and growth mechanism of Al2O3 scales on ferritic Fe-Cr-Al alloys.* Materials Science and Engineering: A, 1998. **247**(1): p. 248-262.
135. HOLLENBERG, G.W. and R.S. GORDON†, *Effect of Oxygen Partial Pressure on the Creep of Polycrystalline Al2O3 Doped with Cr, Fe, or Ti.* Journal of the American Ceramic Society, 1973. **56**(3): p. 140-147.
136. GORDON, R.S., *Mass Transport in the Diffusional Creep of Ionic Solids.* Journal of the American Ceramic Society, 1973. **56**(3): p. 147-152.
137. Lessing, P.A. and R.S. Gordon, *Creep of polycrystalline alumina, pure and doped with transition metal impurities.* Journal of Materials Science, 1977. **12**(11): p. 2291-2302.
138. Hou, P.Y., X.F. Zhang, and R.M. Cannon, *Impurity distribution in Al2O3 formed on an FeCrAl alloy.* Scripta Materialia, 2004. **50**(1): p. 45-49.
139. Haynes, J.A., et al., *Influence of Sulfur, Platinum, and Hafnium on the Oxidation Behavior of CVD NiAl Bond Coatings.* Oxidation of Metals, 2002. **58**(5): p. 513-544.
140. Rivoaland, L., et al., *The Effect of Sulfur Segregation on the Adherence of the Thermally-Grown Oxide on NiAl—II: The Oxidation Behavior at 900°C of*

Standard, Desulfurized or Sulfur-Doped NiAl(001) Single-Crystals. Oxidation of Metals, 2003. **60**(1): p. 159-178.
141. Cannon, R. and P. Hou, *Diffusion induced stress generation during oxidation.* High Temperature Corrosion and Materials Chemistry, 1998: p. 594-607.
142. Clarke, D.R., *The lateral growth strain accompanying the formation of a thermally grown oxide.* Acta Materialia, 2003. **51**(5): p. 1393-1407.
143. Kota, S., et al., *Isothermal and Cyclic Oxidation of MoAlB in Air from 1100°C to 1400°C.* Journal of The Electrochemical Society, 2017. **164**(13): p. C930-C938.
144. Li, X., H. Cui, and R. Zhang, *First-principles study of the electronic and optical properties of a new metallic MoAlB.* Scientific Reports, 2016. **6**: p. 39790.
145. Akopov, G., M.T. Yeung, and R.B. Kaner, *Rediscovering the Crystal Chemistry of Borides.* Advanced Materials, 2017. **29**(21): p. 1604506.
146. Griggs, J., et al., *Spherical nanoindentation, modeling and transmission electron microscopy evidence for ripplocations in Ti3SiC2.* Acta Materialia, 2017. **131**: p. 141-155.
147. Zhou, A.G. and M.W. Barsoum, *Kinking nonlinear elastic deformation of Ti3AlC2, Ti2AlC, Ti3Al(C0.5,N0.5)2 and Ti2Al(C0.5,N0.5).* Journal of Alloys and Compounds, 2010. **498**(1): p. 62-70.
148. Gudlur, P., A. Muliana, and M. Radovic, *Effective thermo-mechanical properties of aluminum–alumina composites using numerical approach.* Composites Part B: Engineering, 2014. **58**: p. 534-543.
149. Hu, L., et al., *Processing and characterization of porous Ti2AlC with controlled porosity and pore size.* Acta Materialia, 2012. **60**(18): p. 6266-6277.
150. El-Raghy, T., et al., *Processing and Mechanical Properties of Ti3SiC2: II, Effect of Grain Size and Deformation Temperature.* Journal of the American Ceramic Society, 1999. **82**(10): p. 2855-2860.
151. Radovic, M., et al., *Tensile properties of Ti3SiC2 in the 25–1300°C temperature range.* Acta Materialia, 2000. **48**(2): p. 453-459.
152. Zhen, T., et al., *Compressive creep of fine and coarse-grained T3SiC2 in air in the 1100–1300 °C temperature range.* Acta Materialia, 2005. **53**(19): p. 4963-4973.
153. Barsoum, M.W., et al., *Dynamic Elastic Hysteretic Solids and Dislocations.* Physical Review Letters, 2005. **94**(8): p. 085501.
154. Zhou, A.G. and M.W. Barsoum, *Nonlinear Elastic Deformation of MAX Phases.* Key Engineering Materials, 2010. **434-435**: p. 149-153.
155. Murugaiah, A., et al., *Spherical Nanoindentations and Kink Bands in Ti3SiC2.* Journal of Materials Research, 2011. **19**(4): p. 1139-1148.
156. Anasori, B. and M.W. Barsoum, *Reversible dislocation motion and microcracking in plastically anisotropic solids under cyclic spherical nanoindentation.* MRS Communications, 2013. **3**(4): p. 245-248.
157. Shamma, M., et al., *On the response of titanium sulfocarbide to stress studied by in situ neutron diffraction and the elastoplastic self-consistent approach.* Scripta Materialia, 2011. **65**(7): p. 573-576.